学位論文

On the X-ray spectral variability in the Fe-K band of active galactic nuclei

(活動銀河核の鉄Kバンドにおける X 線スペクトルの変動性について)

平成29年12月博士（理学）申請

東京大学大学院理学系研究科
天文学専攻

水本　岬希

On the X-ray spectral variability in the Fe-K band of active galactic nuclei

Misaki Mizumoto

Department of Astronomy, Graduate School of Science, The University of Tokyo

February 13, 2018

Abstract

Active Galactic Nuclei (AGNs) are very compact central regions of galaxies, which have similar or even larger luminosities than those of their host galaxies. They have supermassive black holes (BHs) whose masses are 10^{6-9} times the solar mass. Gas accretion onto the BH is considered to produce such large luminosities. AGNs are composed of X-ray emission regions producing the power-law spectra, accretion discs emitting the photons from ultraviolet to soft X-ray, and various types of clouds making absorption and emission features in their energy spectra.

X-ray photons scattered by the surrounding materials of the central BH produce fluorescent Fe-K emission lines at 6.4 keV. Although the line is sharp for the cold and static scattering materials, the observed lines in many AGNs are broadened in $\sim 4-7$ keV (see Miller 2007 for a review). Origin of this broadening is still under discussion. Today, two main scenarios are considered; the scattering material is located in the vicinity of the BH ($\sim R_g$, where R_g is the gravitational radius) or far from the BH ($\sim 100\,R_g$). The former may be called the "disc-reflection scenario", and the latter, the "cloud-reflection scenario".

Time-variability in the Fe-K band has been studied to disentangle the two scenarios. So far, two major observational clues of time variability are reported; root-mean-square (rms) spectra and time lags. First, the rms spectra (energy dependence of the fractional variation) often have a deep and broad dip at $\sim 4-7$ keV (e.g., Matsumoto et al. 2003; Iso et al. 2016). Namely, the Fe-K band has smaller variability compared to the continuum flux. Depth of the dip is as much as $\sim 50\%$ relative to the reference energy band of ~ 2 keV. Second, photons in the Fe-K band are delayed after those in the adjacent energy bands (e.g., Kara et al. 2016). This is interpreted as reverberation lags, where the scattered photons travel through longer distances than the direct ones. Fourier frequencies of the lags are $\sim c/100\,R_g$ Hz, where c is the light velocity, and the delay time (=lag amplitude) is about several R_g/c. The time lags are seen in the broad 4–7 keV band. These features are considered to reflect geometry and structure of materials in the vicinity of the BH, and have an important clue to reveal origin of the broad Fe-K line features.

The disc-reflection scenario expects that scattering occurs in the vicinity of the BH. In this scenario, a tiny X-ray emission region (lamp post) illuminates the innermost area of the accretion disc around the Kerr BH with nearly maximum spin, and the fluorescent Fe-K line is skewed and broadened by the strong gravitational redshift (e.g., Fabian et al. 2002a). The rms dip is explained by variations of the height of the lamp post from the disc (e.g., Miniutti & Fabian 2004), and the light-travel time from the lamp post to the disc is several R_g/c,

which corresponds to the delay time (e.g., Kara et al. 2013c). This scenario may explain each time-variable feature individually and semi-quantitatively. However, there is no study that explains both features simultaneously and quantitatively with the same calculation code. Therefore, we first investigate whether the observed rms dips and reverberation lags can be simultaneously explained in the disc-reflection scenario. We adopt a ray-tracing technique to calculate photon paths including the effect of general relativity, and compare the results with the observations of IRAS 13224–3809, which has both the deep rms dip and the significant iron lags. As a result, we found that the iron abundance ($A_{\rm Fe}$) is required to be extremely high ($\gtrsim 10$ times solar) to explain the observed deep rms dip. On the contrary, the observed reverberation lag is explained with $A_{\rm Fe} = 1$ solar; no reasonable fitting was obtained when $A_{\rm Fe} = 10$ solar. In addition, flux dependence of the lags observed in this object, that the lags disappear in the high-flux periods, cannot be explained in this model. In this manner, we conclude that it is difficult to simultaneously explain the two time-variable features in the Fe-K band of AGNs with the disc-reflection scenario.

Next, we try to explain the observations with the cloud-reflection scenario, which requires absorption/scattering clouds at $\sim 100\,R_g$. In this scenario, the absorption structure produced by the clouds mimics the seemingly broad emission line (e.g., Tanaka et al. 2004; Mizumoto et al. 2014). When the clouds partially cover the X-ray source and the partial covering fraction varies, the deep rms dips are known to be reproduced (Miyakawa et al. 2012; Iso et al. 2016). Here, we try to explain the reverberation lags with the cloud reflection scenario. First, we assume a partial-shell-like cloud at $100\,R_g$ with an outflowing velocity and calculate time-delay of each photon via Monte-Carlo simulation. As a result, we successfully reproduced all the lag features in this geometry. This result is interpreted as follows: First, the reverberation lags are observed at the Fourier frequency of $< c/R$ Hz, where R is a location of the scattering material, so that the clouds at $R \lesssim 100\,R_g$ can explain the observed lag frequencies of $\sim c/100\,R_g$ Hz. Second, the primary component, which has no time delay, is much stronger than the time-delayed scattered component in the Fe-K band, and thus the time delay is diluted by two orders of magnitude. Therefore, even when the light-travel distance of the scattering cloud is $100\,R_g$, the observed lag amplitude gets as short as several R_g/c. Third, when the scattering cloud has an outflowing velocity, photons scattered on the near side are blueshifted, whereas those on the far side are redshifted, which makes the broad lag-energy feature.

The most plausible material outflowing at $\lesssim 100\,R_g$ is a disc wind, which is launched at several tens of R_g due to radiation pressure (e.g., Proga et al. 2000). Therefore, as a next step, we assumed a more realistic disc-wind geometry including radial dependence of the density, ionisation state and velocity, and calculated time lags. As a result, we successfully reproduced the observed lag profiles of three targets: Ark 564, 1H 0707–495, and IRAS 13224–3809, which have characteristic Fe-K lags in common. Moreover, cold clumpy absorbers, which explain the spectral profile and the rms dips, can be generated due to density fluctuation of the wind (Takeuchi et al. 2013). Therefore, we conclude that the cloud-reflection scenario is plausible (table 1).

The physical picture of AGNs we propose is as follows: An X-ray emission region and an

accretion disc exist around the central BH. The hot and continuous disc wind at ∼several tens of R_g produces the reverberation lags, as well as blueshifted absorption lines in the energy spectra. At $\gtrsim 500\,R_g$, cold clumpy absorbers are generated due to density fluctuation of the wind. They partially cover the X-ray emission region and produce the Fe-K edge in the energy spectra, which mimics the broad emission line. Variability of the partial covering fraction produces the deep rms dips in the Fe-K band In these manners, we are successful to draw a self-consistent physical picture to simultaneously explain all the X-ray spectral variability in the Fe-K band of AGNs.

Table 1: Previous status (before our work) and results of this thesis about the two scenarios

Previous status

	Line profile	rms dip	time lag
Disc-reflection	◯	△	△
Cloud-reflection	◯	◯	?

⇓

Results of this thesis

		Line profile	rms dip	time lag
Disc-reflection	($A_{\rm Fe} = 1$ solar)	×	×	◯
	($A_{\rm Fe} = 10$ solar)	◯	◯	×
Cloud-reflection	($A_{\rm Fe} = 1$ solar)	◯	◯	◯

Contents

List of Figures

Chapter 1

Introduction

Active galactic nuclei (AGNs) emit strong radiation in all the wavelength ranges, and their spectra have a lot of features. They host supermassive black holes (BHs) at their centre, and mass accretion to the central BH fuels the high luminosity of AGNs. Among the whole wavelength range, X-ray is emitted from the hottest region in AGNs, i.e., in the vicinity of the central BH. One of the most feature-rich energy bands in X-ray is the Fe-K band (around 5–8 keV). This band has an iron absorption edge and many emission/absorption lines. When the primary emission from the central region of AGN interacts the material around the BH, the absorption and/or emission features are produced in this energy band, which tells us structure and geometry around the central BH. Therefore, the Fe-K spectral features can be a powerful diagnostic tool to investigate AGN physics.

A seemingly broad iron emission line has been reported in X-ray energy spectra of many AGNs, which is resolved by CCD detectors ($\Delta E/E \sim 10-30$). When photons are scattered on neutral and static materials, a sharp Fe-K fluorescent line would be produced at 6.4 keV. However, the observed iron lines in many AGNs seem to be broadened, with low-energy tails down to $\sim$ 4 keV. It was clearly recognised in MCG–6-30-15 with the Solid-State Imaging Spectrometer (SIS) on *ASCA* satellite (Tanaka et al. 1995), and in many other AGNs with the European Photon Imaging Camera (EPIC) on *XMM-Newton*, the X-ray Imaging Spectrometer (XIS) on *Suzaku*, and so on (Miller 2007 for a review). It has been known that about a half of AGNs have such broad line features (Nandra et al. 2007). If this line feature is really an emission line, it must be strongly broadened and skewed by some physical mechanisms. For instance, it was explained by relativistically-blurred reflection, in which the line shape is distorted by effects of the strong gravitational redshift (e.g. Fabian et al. 2002a). In this interpretation, the iron line has to originate from the innermost area of the accretion disc around the nearly maximum-spinning Kerr-BH. On the other hand, this spectral feature can be due to an absorption edge (e.g., Tanaka et al. 2004; Mizumoto et al. 2014) or a broad absorption line (Hagino et al. 2016). Also, Noda et al. (2011a) argued that the continuum has at least two primary components and that, in this case, the strong broadening of the iron line is not necessary. All of these models can explain the time-averaged spectral feature equally well, so origin of the broad Fe-K line has still been under discussion.

Time-variability in the Fe-K band should bring us key information to disentangle the

degenerate theoretical models. Today, two major observational clues of time variability are reported; root-mean-square (rms) spectra and time-lags. First, the rms spectra (energy dependence of the fractional variation) of AGNs are known to have a deep and broad dip at $\sim 5-7$ keV (e.g., Matsumoto et al. 2003; Terashima et al. 2009; Iso et al. 2016). Namely, the Fe-K band has smaller variability compared to the continuum flux. Depth of the dip is as large as $\sim 50\%$ relative to the reference energy band of ~ 2 keV. Second, photons in the Fe-K energy band are found to be delayed after those in the adjacent energy bands. Kara et al. (2013b) found that the photons in 5–7 keV lag behind those in the adjacent energy bands in 1H 0707–495. The lag amplitude is about 50 s ($= 5\,R_g/c$ when $M_{\rm BH} = 2\times10^6\,M_\odot$, where $R_g = GM_{\rm BH}/c^2$ is the gravitational radius and $M_{\rm BH}$ is the BH mass). The broad feature is also seen in the lag-energy spectrum. Kara et al. (2016) systematically investigated time lags of Seyfert galaxies in the *XMM-Newton* archive data, and found that $\sim 50\%$ of sources have the Fe-K reverberation lags. The time delay (=lag amplitudes) are commonly $1-9\,R_g/c$, and the characteristic Fourier frequency is $\sim c/100\,R_g$ Hz. These two observational facts about time variability must be related to the broad Fe-K line feature because they have similar energy-dependence.

In this thesis, we try to construct such a physical picture of AGNs that can explain the X-ray spectral variability in the Fe-K energy band comprehensively and self-consistently. We focus on the 2–10 keV band with the variation timescale of $\lesssim 1$ day. The plan of this thesis is as follows: We review AGNs, their X-ray spectral features and variability, and their current understanding toward the Fe-K band in Chapter 2. The purpose of this thesis is shown in Chapter 3. In Chapter 4, we examine the disc-reflection scenario to explain Fe-K band of AGNs and examine its validity. Next, we carefully study the cloud-reflection scenario in Chapter 5. Based on these results, we present a picture of AGN to explain the X-ray spectral variability in Chapter 6. Main results of this thesis are summarised in Chapter 7.

Chapter 2

Review

Contents

2.1 Active Galactic Nuclei (AGNs)

2.1.1 Theory of black holes

Theories of black holes (BHs) began with the theory of general relativity (GR) proposed by Einstein in 1915. Under the Newtonian mechanics, an escape velocity $v_{\rm esc}$ from the surface of an object with a mass of M and a radius of r is

$$\frac{1}{2}v_{\rm esc}^2 = G\frac{M}{r}, \tag{2.1}$$

where G is the gravitational constant. When the escape velocity is equal to the light speed c, the radius R_s is

$$R_s = \frac{2GM}{c^2} \approx 3 \times 10^5 \left(\frac{M}{M_\odot}\right) \ \ [\rm cm], \tag{2.2}$$

where $M_\odot$ is the solar mass. Therefore, if the radius of the object is less than R_s, even the light cannot escape from its surface under Newtonian mechanics. GR theory writes down such an extreme condition precisely. Einstein equation, which is a basic equation of GR theory, is as follows:

$$R_{\mu\nu} - \frac{1}{2}g_{\mu\nu}R = \frac{8\pi G}{c^4}T_{\mu\nu}, \tag{2.3}$$

where $R_{\mu\nu}$ is a Ricci tensor, $g_{\mu\nu}$ is a metric tensor, R is a scalar curvature, $T_{\mu\nu}$ is a stress-momentum tensor. Schwarzschild solved equation (2.3) under the condition that mass exists only at the centre of the isotropic spacetime. Schwarzschild's metric is

$$ds^2 = -\left(1 - \frac{R_s}{r}\right)dt^2 + \left(1 - \frac{R_s}{r}\right)^{-1}dr^2 + r^2 d\theta^2 + r^2 \sin^2\theta d\phi^2, \tag{2.4}$$

and the proper time is

$$d\tau = \left(1 - \frac{R_s}{r}\right)^{1/2} dt, \tag{2.5}$$

which shows that a clock time becomes slower near the vicinity of $r = R_s$ and that the inner region ($r < R_s$) cannot be observed from the outer region. R_s is called as the Schwarzschild radius. If material collapses within $r < R_s$, information of the inner region cannot reach the outer world; this is the concept of BH.

2.1.2 Discovery of AGNs

Active Galactic Nucleus (AGN) is such a very compact central region of an active galaxy that has a comparable or even larger luminosity than its host galaxy itself. The total luminosity of AGN reaches up to $\sim 10^{43-47}$ erg s^{-1}.

Fath (1909) discovered strong emission lines in an optical spectrum of NGC 1068, which was the first observation of AGNs. Seyfert (1943) performed optical spectroscopy of galaxies with high surface luminosities in their central regions, and found that they have especially bright nuclei with many broad and highly-ionised emission lines. Today they are called as "Seyfert galaxies", which are typical AGNs.

From the late of 1950s, many radio sources have been identified. A large radio survey observation program (the 3C catalogue) listed about 500 objects, many of whose optical spectra were found to be similar to those of Seyfert galaxies. On the other hand, Matthews & Sandage (1963) found several unique quasi-stellar objects (e.g., 3C 273) with unidentified broad emission lines. They were named quasars. Schmidt (1963) identified the emission lines in 3C 273 as those with a large redshift ($z = 0.158$). This indicates that the source is located at a cosmological distance and that its luminosity is brighter than normal galaxies by two or three orders of magnitude; indeed quasars are particularly bright AGNs.

It is now believed that AGN hosts a supermassive black hole (SMBH), and that mass accretion to the central BH fuels the high luminosity of AGNs. Mass accretion is the most efficient way in the Universe to release a large amount of energy. Let us assume an object whose radiation is isotropic and spherically symmetric, with the mass M and the luminosity L. When the object consists of hydrogen atoms, the gravitation at a distance r is

$$F_{\rm grav} = \frac{GMm_p}{r^2}, \tag{2.6}$$

where m_p is the proton mass. When an electron and a proton are Coulomb coupled, the radiation force from the BH is expressed as

$$F_{\rm rad} = \frac{\sigma_{\rm T}}{c}\frac{L}{4\pi r^2}, \tag{2.7}$$

where $\sigma_{\rm T}$ is the Thomson cross section. Therefore, the maximum stable luminosity is expressed as the equation of $F_{\rm grav} = F_{\rm rad}$, and

$$L = \frac{4\pi cGMm_p}{\sigma_{\rm T}} \approx 1.25 \times 10^{38} \left(\frac{M}{M_\odot}\right) \ [{\rm erg\,s^{-1}}]. \tag{2.8}$$

This luminosity is called as Eddington luminosity ($L_{\rm Edd}$). Substituting AGN luminosities $\sim 10^{43-47}$ erg s^{-1} to equation (2.8), we can estimate masses of the central object of AGNs as $10^{5-9}\,M_\odot$. Recently, some of the masses can be directly constrained by observing dynamics of molecular gas. For example, Onishi et al. (2015) measured the mass in the central region of NGC 1097 as $1.40^{+0.27}_{-0.32} \times 10^8\,M_\odot$ with ALMA observations. The size of the central object may be constrained by time variability. In particular, X-rays from AGNs are known to show rapid variability (e.g., Mushotzky et al. 1993). The variability timescales are roughly 10^{3-4} s, which corresponds to the Schwarzschild radius, $R_s/c = 10^3\,(M_{\rm BH}/10^8 M_\odot)$ s. A direct radio imaging of the Schwarzschild-radius-scale structure is now attempted with the Event Horizon Telescope (e.g., Akiyama et al. 2017).

2.2 X-ray energy spectra of AGNs

AGNs emit electromagnetic waves with a wide wavelength range, from radio to γ-ray. X-ray has the high photon energy, radiated from the central hot region in AGNs. Also, heaviest atomic transitions take place in the X-ray energy band. Therefore X-ray tells us physics of the dynamic region around the central SMBHs with strong gravitational fields. AGNs have complex geometries and structure, and their X-ray energy spectra are also complex. Below, we review each of the components constituting the AGNs.

2.2.1 Accretion disc component

An accretion disc around the SMBH emits thermal radiation corresponding to its temperature. In a normal AGN where its disc is optically-thick and geometrically-thin (the "standard" disc; formulated by Shakura & Sunyaev 1973), its spectral energy distribution (SED) has a big hump in the ultraviolet (UV) to soft X-ray bands (Koratkar & Blaes 1999). When the disc is optically thick, it emits a blackbody radiation and its luminosity is estimated as

$$L(r)dr = \frac{GM_{\rm BH}\dot{M}}{2r}dr = 2\pi r^2 \sigma T(r)^4 dr \tag{2.9}$$

where σ is the Stefan-Boltzmann constant, $T(r)$ is temperature of the disc, and $\dot{M}$ is the mass accretion rate. Thus the temperature is

$$T(r) = \left(\frac{GM_{\rm BH}\dot{M}}{4\pi\sigma r^3}\right)^{1/4} \tag{2.10}$$

When the viscous torque is taken into account, equation (2.10) is written as

$$T(r) = \left[\frac{3GM_{\rm BH}\dot{M}}{8\pi\sigma r^3}\left\{1 - \left(\frac{R_{\rm in}}{r}\right)^{1/2}\right\}\right]^{1/4}, \tag{2.11}$$

where $R_{\rm in}$ is the inner radius of the disc. At $r \gg R_{in}$,

$$T(r) = \left(\frac{3GM_{\rm BH}\dot{M}}{8\pi\sigma R_{\rm in}^3}\right)^{1/4}\left(\frac{r}{R_{\rm in}}\right)^{-3/4}. \tag{2.12}$$

In this way, the radiation from the disc is expressed as summation of the black body radiation with different temperatures (multi-color disc model; Mitsuda et al. 1984).

In the Newtonian mechanics, $R_{\rm in}$ can be as small as possible, but in GR, $R_{\rm in}$ has the lower limit to keep a stable orbit, which is called as the innermost stable circular orbit (ISCO). The radius of ISCO around the Schwarzschild BH is $3\,R_s = 6\,R_g$, where R_g is the gravitational radius ($= R_s/2$). The ISCO around a Kerr BH (=rotational BH) monotonically decreases as the BH spins faster, where the spin is parameterised by a spin parameter $a = J/M_{\rm BH}^2$ where J is the angular momentum of the BH. When the spin parameter is maximum ($a = 0.998$), ISCO gets minimum at $1.24\,R_g$. Below, we assume $R_{\rm in} = R_s$ for simplicity. Equation (2.12) is calculated as

$$T(r) = \left(\frac{3c^6}{64\pi\sigma G^2}\right)^{1/4}\dot{M}^{1/4}M_{\rm BH}^{-1/2}\left(\frac{r}{R_s}\right)^{-3/4} \tag{2.13}$$

$$= 6.3\times10^5\left(\frac{\dot{M}}{\dot{M}_{\rm Edd}}\right)^{1/4}\left(\frac{M_{\rm BH}}{10^8\,M_\odot}\right)^{-1/4}\left(\frac{r}{R_s}\right)^{-3/4}\ [\rm K], \tag{2.14}$$

where $\dot{M}_{\rm Edd} = 1.4\times10^{18}(M_{\rm BH}/M_\odot)$ g s^{-1} is Eddington mass accretion rate. Using Wien's displacement law, the peak energy of inner disc emission is calculated as

$$h\nu_{\rm max} = 2.8kT(r_{\rm in}) \sim 0.1\ \rm keV. \tag{2.15}$$

This indicates that the standard disc emits optical/UV to soft X-ray photons.

When $\dot{M}$ increases, the disc gets hotter and geometrically-thicker, and becomes a "slim" disc (Abramowicz et al. 1988). This disc emits harder photons, and its peak of SED reaches the X-ray energy band. This is one of the plausible mechanisms to explain a "soft excess", which is an excess component seen in the $\lesssim 1$ keV energy band of many narrow-line Seyfert 1 galaxies (Mineshige et al. 2000). However, origin of the soft excess is still under debate and many models have been considered. For example, Sobolewska & Done (2007) proposed that the soft excess component is reproduced by complex emission and absorption lines produced in the relativistic outflow winds.

2.2.2 Power-law component

X-ray energy spectra of AGNs in the 1–50 keV band are dominated by a power-law component, which is expressed as $E^{-\Gamma}\exp(-E/E_c)$, where Γ is a photon index and E_c is a cut-off energy ($\sim$a few hundreds keV). When UV seed photons from the disc enter a hot corona above the disc, they gain energies by inverse Compton scattering, which can produce a power-law spectrum (Thorne & Price 1975; Sunyaev & Truemper 1979). The cut-off energy is produced because photons cannot receive much higher energies than the coronal temperature. Let us assume that a seed photon with energy of $E_{\rm initial}(\ll kT_e)$, where k is Boltzmann constant, is scattered on the non-relativistic thermal plasma whose electron temperature is T_e. With a single inverse Compton scattering, the photon's energy increases by $\Delta E = (4kT_e/m_ec^2)E_{\rm initial}$, where m_e is the electron mass. When the photon is scattered N times, The resultant photon energy is calculated as

$$E \simeq E_{\rm initial}\exp\left[N\left(\frac{4kT_e}{m_ec^2}\right)\right]. \tag{2.16}$$

N is expressed as $\max(\tau,\tau^2)$ where τ is an optical depth, and thus

$$E \simeq E_{\rm initial}e^y \tag{2.17}$$

$$y \equiv \max(\tau,\tau^2)\,\frac{4kT_e}{m_ec^2}, \tag{2.18}$$

where y is called as Compton y-parameter. The photon index Γ is written as

$$\Gamma = -\frac{3}{2} \pm \sqrt{\frac{9}{4}+\frac{4}{y}}. \tag{2.19}$$

Geometries of the X-ray emitting corona have not been elucidated yet. Figure 2.1 shows some suggested geometries (Reynolds & Nowak 2003). A slab geometry, where both disc and corona exist at the same radii, was once suggested (top panel), but such a corona is easily cooled that it is difficult to reach the high enough temperature to produce the observed hard spectrum (e.g., Stern et al. 1995). If the corona is located in the central region and the soft photons come from the outer cool disc, the corona is not strongly Compton cooled and can remain hot enough to produce observed hard spectra (middle two panels; see Dove et al. 1997). Instead, if the corona is patchy, such that small corona regions sit atop the disk (bottom panel), a relatively small fraction of the reprocessed disc flux is intercepted by the corona, and the corona can also be hot enough (Stern et al. 1995).

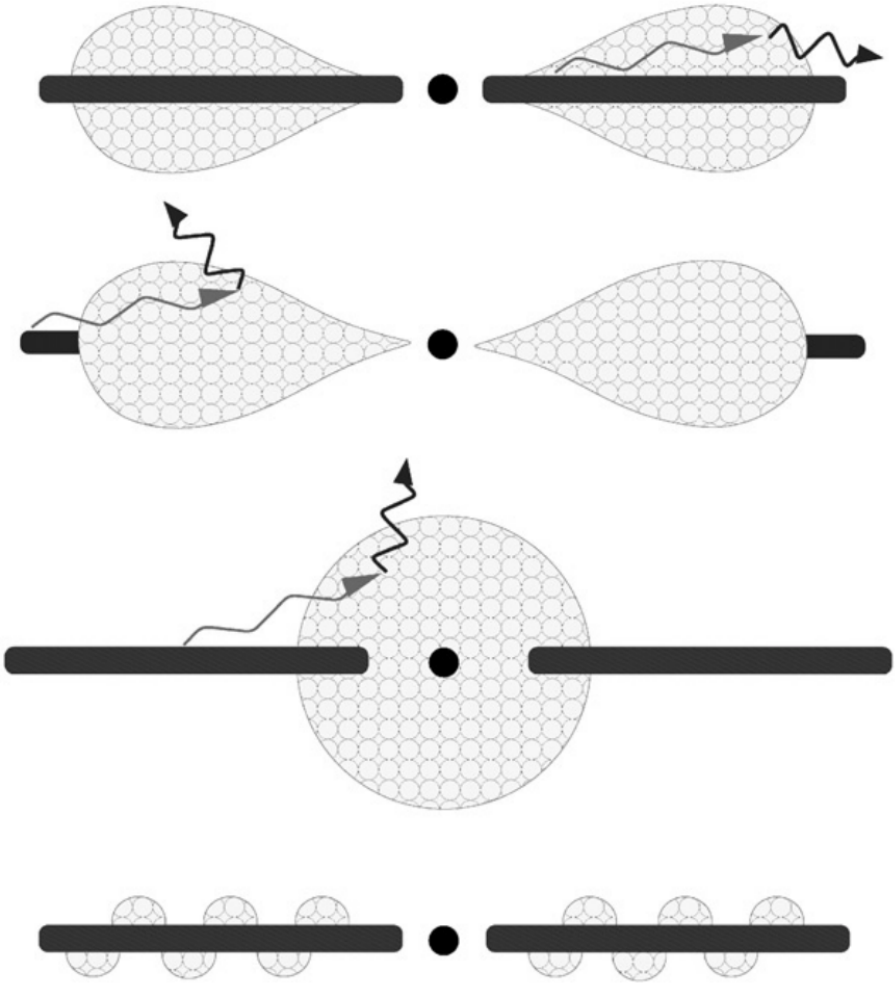

Figure 2.1: Suggested geometries for an accretion disc and X-ray emitting corona (Reynolds & Nowak 2003). The wave arrows show the seed photons. The top panel is like a "slab", but this geometry cannot explain hardness of the X-ray energy spectra (e.g., Stern et al. 1995). The other three show "photon starved" geometries; the middle two geometries are often referred to as "sphere+disc" geometries, whereas the bottom geometry is often referred to as a "patchy corona".

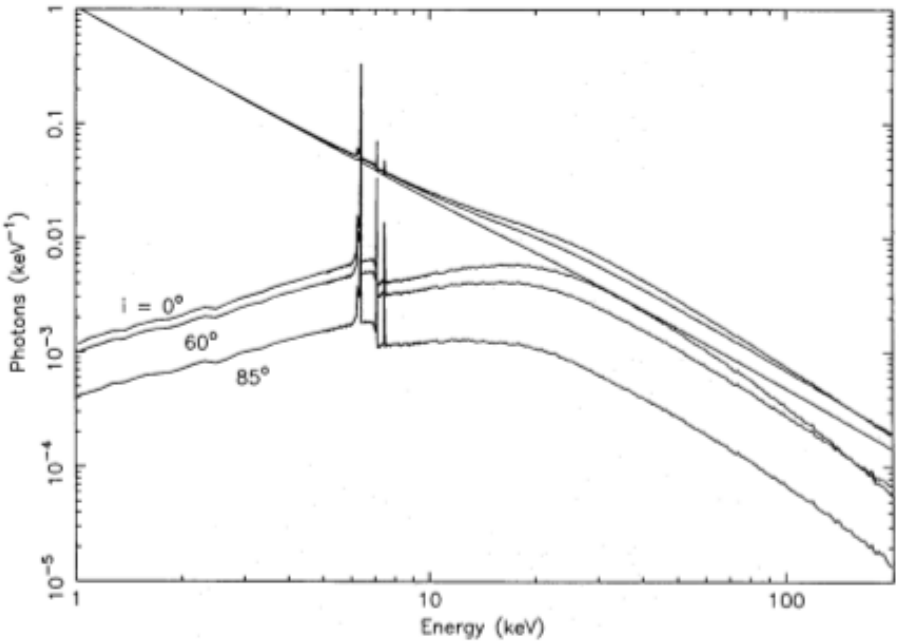

Figure 2.2: Reflected spectra as well as the composite (reflected+primary) spectra for a flat, optically-thick, non-rotating circular slab illuminated by an isotropic source with different inclination angles (George & Fabian 1991).

2.2.3 Reprocessed component

X-ray irradiation of the high-density materials gives rise to a characteristic reflection spectrum, which is the result of photoelectric absorption and Compton scattering (figure 2.2). The photoelectronic cross-section (σ_a) of K-shells of atoms with the atomic number Z is $\sigma \propto Z^5 \nu^{-7/2}$, and thus the absorption probability is higher in the lower energy band (Morrison & McCammon 1983). The cross-section of Compton scattering (σ_s) is formulated by Klein-Nishina, which is almost constant in the energy band of figure 2.2. The reflection probability is calculated from the two cross-sections above, e.g., $\sim \sigma_s/(\sigma_a + \sigma_s)$ in the optically-thick material, which results in the energy dependence of the reflection spectrum. In the higher energy band than several tens of keV, energy shift due to Compton recoil gets significant and produces a broad structure around 20–30 keV, which is called as a "Compton hump".

Fluorescent lines, as well as scattering continuum, are observed in the neutral material. The Fe-Kα fluorescent line at 6.4 keV is strongest and thus most investigated. The fluorescent lines are produced when one of the two K-shell electrons of atoms is ejected due to photoelectric absorption of photons with ≥ 7.1 keV. Following the bound-free transition, an L-shell electron drops into the K-shell, and the transition energy is released from the atom in either of the following ways; released as a photon of 6.4 keV and produces an Fe-Kα emission line, or internally absorbed by another electron that is escaped as an Auger electron. Fluorescent yield is the probability of the former case, which is about 0.35 for neutral iron (Pious et al. 1992). There are many candidates of the Fe-Kα emitter: an accretion disc, a

broad-line region, a dusty torus, and so on. Observation of Perseus cluster by *Hitomi* satellite (Takahashi et al. 2016) was performed on 2016 Feb.–Mar. (Hitomi Collaboration 2016), and the Soft Xray Spectrometer (SXS; Kelley et al. 2016) directly measured the intrinsic width of the Fe-Kα line of NGC 1275 (within the view field of Perseus cluster) for the first time, as $\sim 500 - 1400$ km s^{-1} (FWHM). This narrow width implies that the Fe-Kα emitter is located at a few hundred parsec distance from the central BH, such as the dusty torus (Hitomi Collaboration 2017).

The fluorescent line is produced also in the ionised case, as far as photons exist in the L-shell (Ross & Fabian 1993). Energies of the photoelectric threshold and the Kα line increase with the ionisation degree, while the fluorescent yield is not so much changed up to Be-like ions (Fe XXIII). For Li-like irons (Fe XXIV), there are no electrons in the L-shell except for the one dropping to the K-shell, and the Auger effect cannot take place. In He- and H-like ions, the line is produced mainly by the capture of free electrons; when a photon with a certain energy (6.7 keV for He-like, and 7.0 keV for H-like) is absorbed, a K-shell electron is excited to the L-shell, and the excited-electron is soon de-excited, emitting an X-ray photon toward 4π (resonance scattering). Cross-section of the resonance scattering is much higher than that of Thomson scattering by several orders of magnitude, so the former is strongly seen in the cases of highly-ionised ions.

Ionisation state of the photoionised plasma is characterised by the ionisation degree, $\xi = L/(nr^2)$, where L is the ionising luminosity integrated between $1 - 1000$ Rydberg, n is the number density of the material, and r is the distance from the source to the material (figure 2.3). The iron line emission for various ξ was investigated by Matt et al. (1996, 1993), and its feature was found to be distinct with four regimes depending on ξ (figure 2.4; also see Fabian et al. 2000 for a review):

1. $\xi < 100$ (ergs cm s^{-1}) — The material is not ionised up to Fe XVIII, so the neutral iron line at 6.4 keV is seen.

2. $100 < \xi < 500$ — Most of the ions are in the forms of Fe XVII–Fe XXIII, where there is a vacancy in the L-shell. Therefore, these ions can resonantly absorb the corresponding Kα line photons. Successive fluorescent emission followed by resonant absorption effectively traps the photon in the surface layers of the material until it is terminated by the Auger effect. Only a few photons can escape the material, leading to a very weak iron line.

3. $500 < \xi < 5000$ — The ions are highly ionised (more than Li-like), and thus the Auger effect is no longer permitted. Whereas the line photons are still subject to resonant scattering, the lack of a destruction mechanism allows the photons to escape the material.

4. $5000 < \xi$ — The material is mostly fully ionised so the line flux is very weak. Especially when $\log \xi$ exceeds 5, population of the H-like ions becomes less than 50% and the iron lines almost disappear.

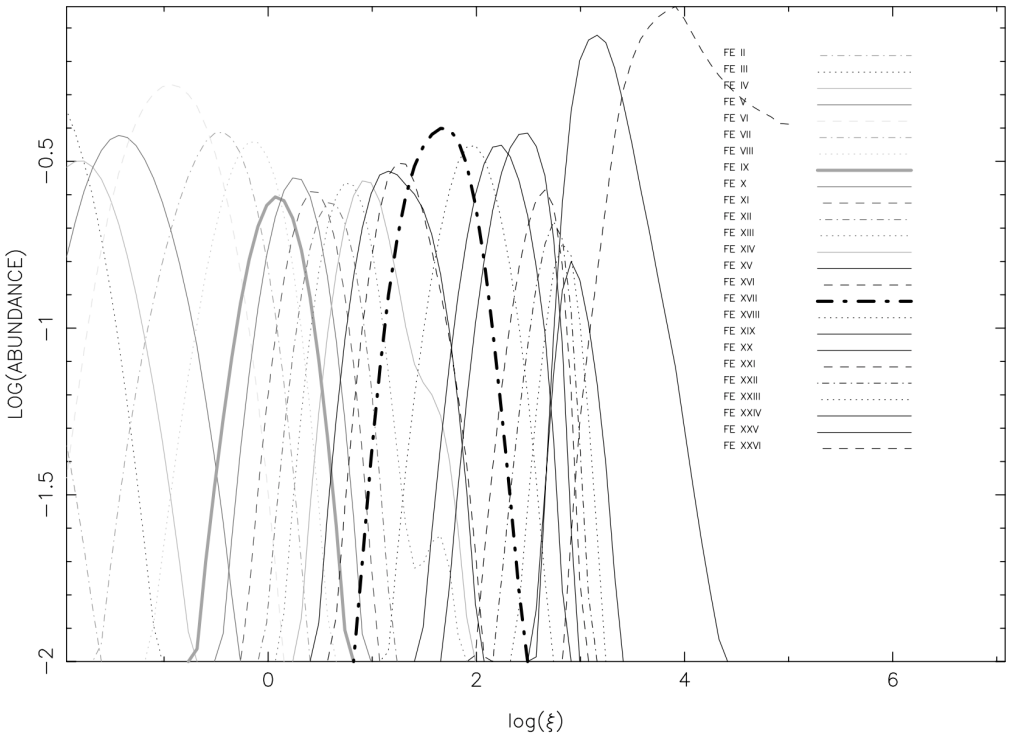

Figure 2.3: Ion population of iron as a function of ξ (Kallman et al. 2004). The higher-ionised ions are likely to exist for the higher ξ value.

2.2.4 Cold and warm absorbers

Ambient matters in AGNs can absorb X-ray photons emitted from the X-ray corona and make complex features in the X-ray energy spectra. These absorptions are roughly divided into two categories: neutral absorption and ionised absorption. These absorptions make observed X-ray spectral features and variability in AGN especially at lower energies (Turner & Miller 2009 for a review).

Neutral absorption occurs in a low-temperature and low-ionised absorber, such as a dusty torus and interstellar medium in the host galaxy and/or in our Galaxy. The absorption effect is written as $\exp[-N_{\rm H}\sigma(E)]$, where $N_{\rm H}$ is the column density and $\sigma(E)$ is a photoionisation cross section. Although amount of the absorption gas is usually expressed as the column density of the hydrogen atoms, the actual X-ray photons are absorbed by heavy elements like carbon, oxygen, neon, silicon, and so on. When the neutral absorption takes place, soft X-ray photons below 1 keV are heavily absorbed, and a deep Fe-K edge is produced at 7.1 keV.

Ionised absorption occurs in an ionised clouds around the central BH, such as warm absorbers and outflowing clouds. Bound-bound transitions in H- and He-like ions of heavy elements in these clouds make absorption lines especially in the 1–2 keV and $\gtrsim 7$ keV band. Some AGNs are known to have blueshifted absorption lines of H- and/or He-like iron ions with especially high outflow velocities, as high as several tens percent of the light velocity. These high-velocity outflows are called as UltraFast Outflows (UFOs; figure 2.5, also see

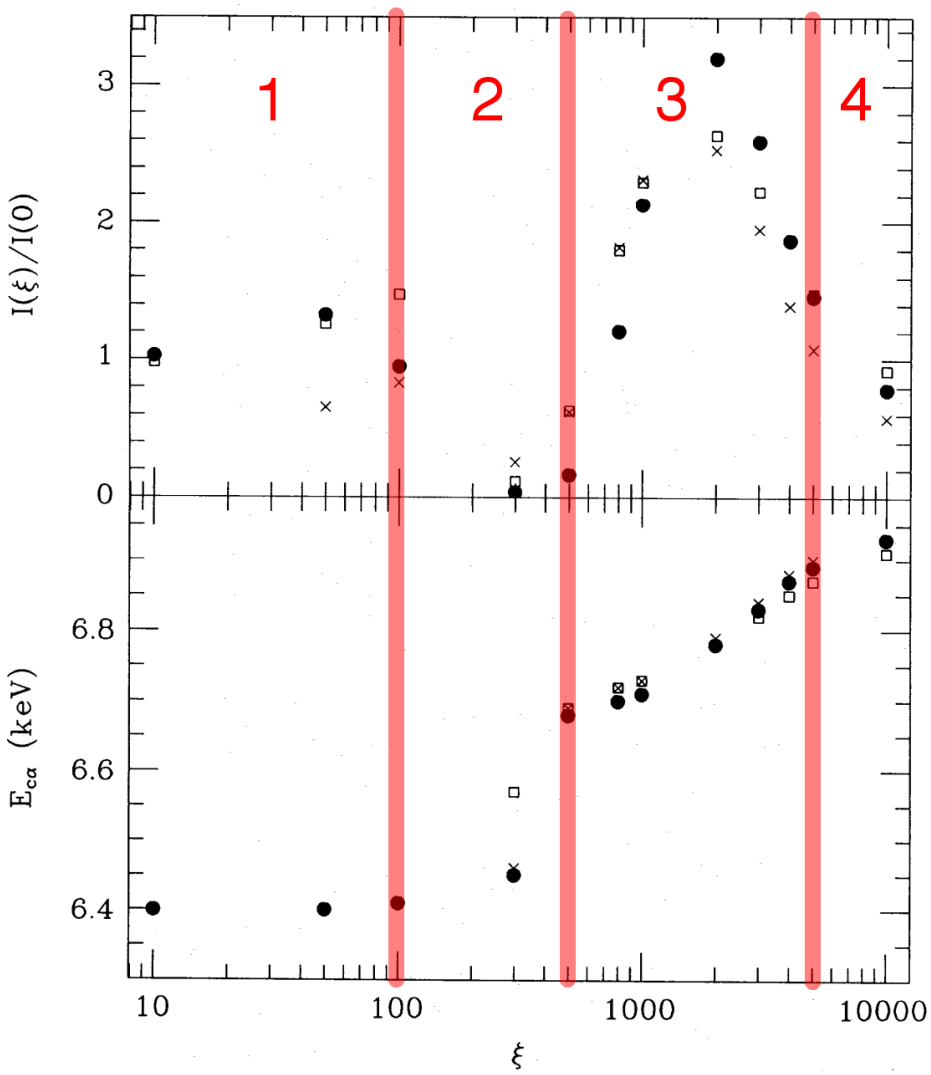

Figure 2.4: Intensity (normalised at $\xi = 0$) and centroid energy of the iron line emitted by a plane-parallel slab as a function of ξ in the face-on case (Matt et al. 1993; editted). The crosses and circles show $\mu_0 = 1/\sqrt{3}$ and 1, respectively, where μ_0 is cosine of the incident angle. The squares assume that the soft flux is proportional to the hard flux, whereas it is constant in the other symbols. The red numbers (1, 2, 3, 4) indicate the separated regimes explained in the main text.

Tombesi et al. 2010). Though number of the samples is still limited, UFOs are detected in about a half of Seyfert galaxies (e.g., Gofford et al. 2015). Their velocities, ionisation degree, and column densities are roughly $v \sim 0.03c - 0.3c$, $\log \xi \sim 3 - 6$, and $N_{\rm H} \sim 10^{22} - 10^{24}$ cm^{-2} (Tombesi et al. 2011). One of the most plausible origins of the UFO is the "line-driven disc wind", where radiation force due to the spectral line absorbing UV radiation through the bound-bound transition of metals accelerates gases and launches outflows from the disc surface (figure 2.6; see e.g., Stevens & Kallman 1990; Proga et al. 2000; Proga & Kallman 2004).

2.3 Broad Fe-K spectral features

2.3.1 Line profiles

When photons are scattered on neutral materials, such as an outer part of an accretion disc or a dusty torus, the sharp Fe-K fluorescent line is produced at 6.4 keV. However, the observed Fe-K lines in AGNs are commonly more broadened, with significant low-energy tails down to $\sim$ 4 keV. If this feature is a real emission line, it must be skewed by some physical mechanisms. *ASCA* satellite clearly showed the broad Fe-K line in MCG–6-30-15 (figure 2.7; see Tanaka et al. 1995). Nandra et al. (2007) comprehensively analysed Seyfert 1 galaxies observed by *XMM-Newton*, and found that $\sim$ 45% of them have such broad Fe-K line features. However, the line profile highly depends on how to estimate the continuum level, and there are complicated spectral features other than the fluorescent line in the Fe-K band, such as ionised absorption lines, absorption edge, and Compton shoulder. Indeed, there are several alternative models to explain the observed broad Fe-K line profiles (see §2.4).

2.3.2 Spectral variability

Time-variability in the Fe-K band has been actively investigated as it should bring us a key information to reveal the line production mechanism. Today, two major observational clues of time variability are reported: root-mean-square (rms) spectra and time-lags. First, the rms spectra (energy dependence of the fractional variation) of AGNs are known to have a deep and broad dip at $\sim 4-7$ keV, which has been reported from MCG–6-30-15 (Fabian et al. 2002b; Matsumoto et al. 2003) and other AGNs (e.g., Iso et al. 2016). That is, the iron lines in Seyfert galaxies have low variability compared to the continuum flux. Depth of the dip is as much as $\sim$ 50% relative to the reference energy band of $\sim$ 2 keV (figures 2.8, 2.9). Second, when the intrinsic hard X-ray illuminates the surrounding materials and the fluorescent Fe-K emission line and continuum reflection are produced, the reprocessed emission should be lagged and smeared by the light travel time from the source. In other words, we expect to observe reverberation lags. In fact, the Fe-K reverberation lags in AGNs were significantly detected in *XMM-Newton* observations of 1H 0707–495 (Kara et al. 2013b); photons in the Fe-K energy band lag behind those in the adjacent energy bands by $\simeq$ 50 s, corresponding to

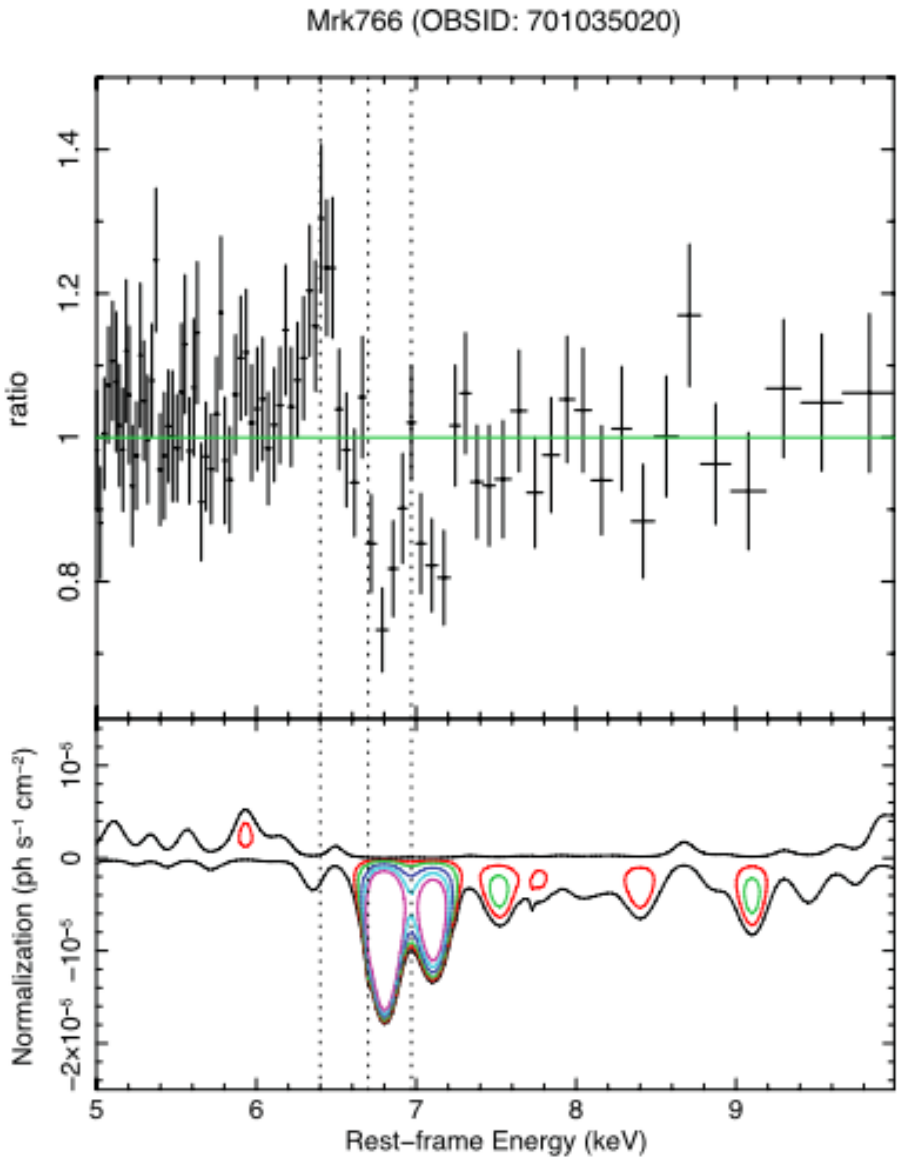

Figure 2.5: UFO lines in Mrk 766 (Gofford et al. 2013). Top panel: ratio of the energy spectrum to the continuum including reflection continuum. Bottom panel: confidence contours showing deviations from the best-fitting model. Two highly significant (> 99.99 %) absorption profiles are clearly detected. They are He- and H-like iron ions with the outflowing velocity of $\sim 0.05c$.

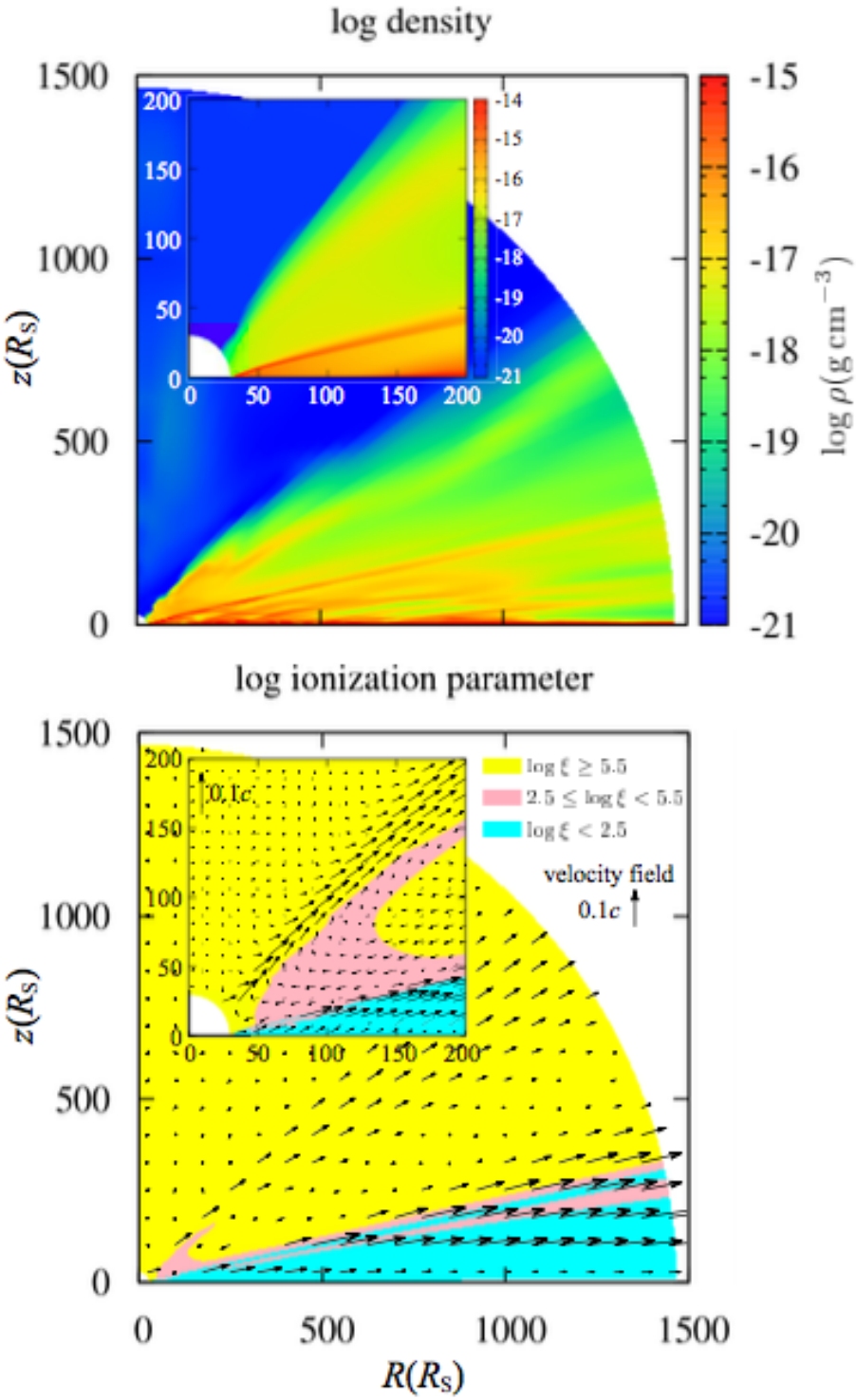

Figure 2.6: Numerical simulation of a line-driven disc wind for the Eddington ratio of 0.5 and the BH mass of $10^8\,M_\odot$ (Nomura et al. 2016). The $z = 0$ plain corresponds to the disc surface and the z-axis is equal to the rotational axis. Top panel: the time-averaged density map. Bottom panel: the ionisation parameter map with the velocity field (shown by vectors). The pink region with $2.5 \leq \log \xi < 5.5$ shows the area where the UFO line is likely to be produced, whose solid angle is $\Omega/4\pi \sim 0.2$.

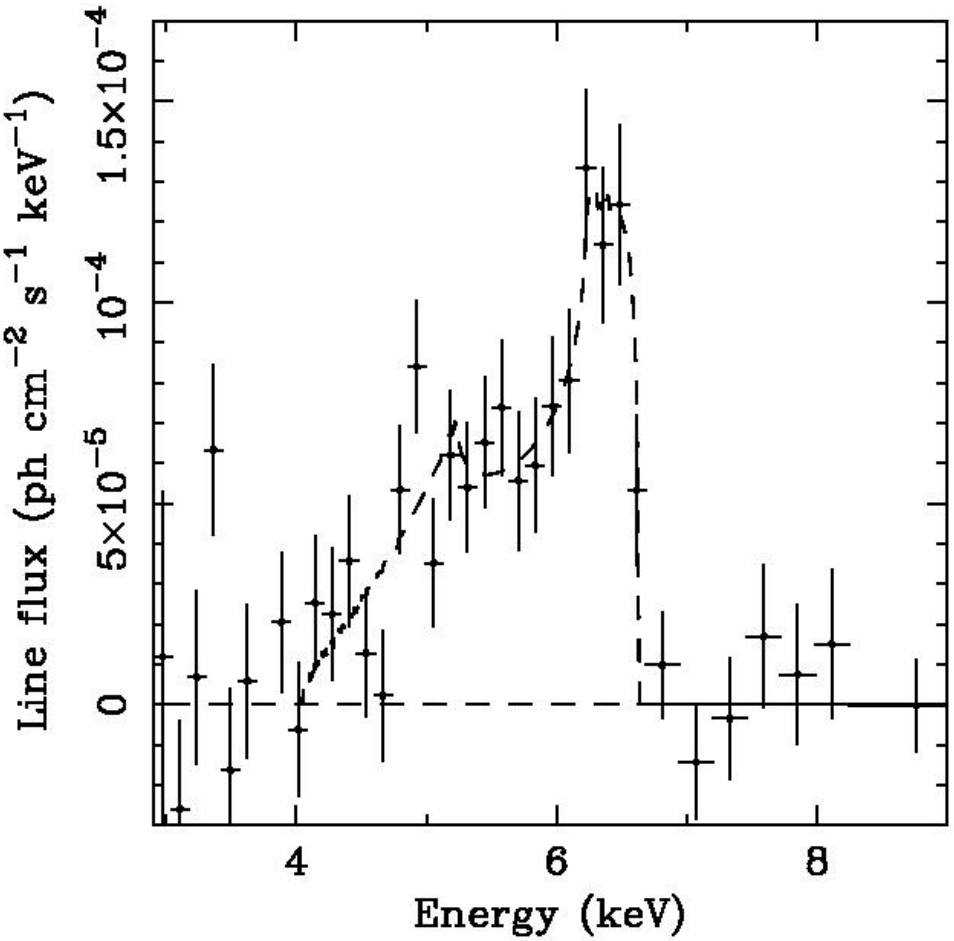

Figure 2.7: Broad Fe-K line profile in MCG–6-30-15 obtained by *ASCA* (Tanaka et al. 1995). The continuum level is fitted by power-law in the adjacent energy band of the line profile.

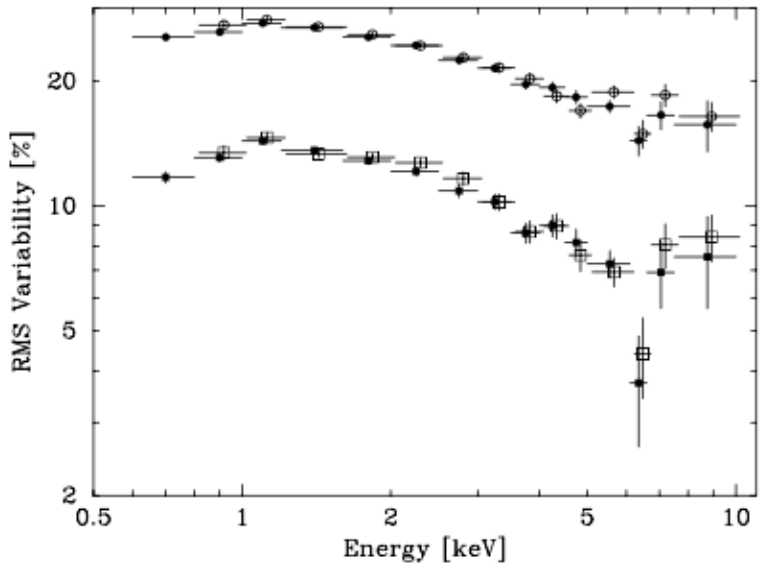

Figure 2.8: Spectral variability of MCG–6-30-15 observed by *ASCA* in the time-bin-widths of 2.3×10^4 s (circles) and 1.8×10^5 s (squares), shown in Matsumoto et al. (2003). The filled/open marks correspond to the two different types of the detectors.

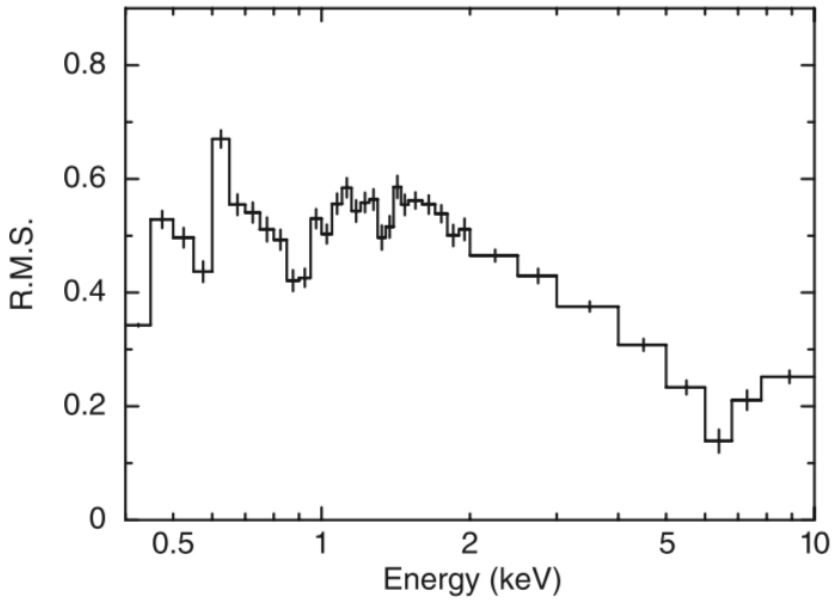

Figure 2.9: Spectral variability of NGC 4051 observed by *Suzaku* in the time-bin-widths of 1024 s (Terashima et al. 2009).

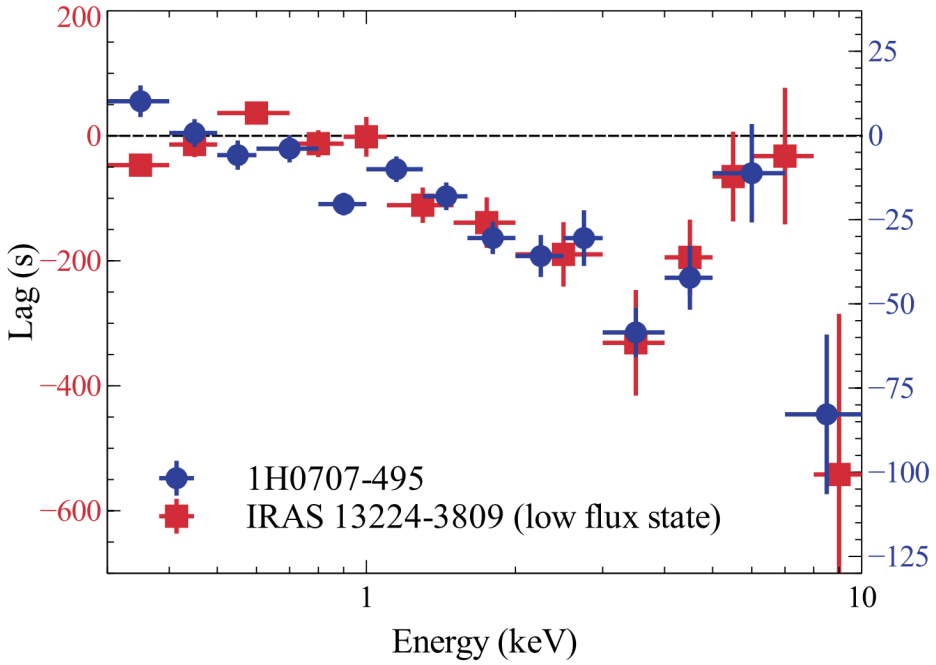

Figure 2.10: Lag-energy spectra for 1H 0707–495 (blue) and IRAS 13224–3809 in the low-flux periods (red), shown in Kara et al. (2013a). Fourier frequency ranges are $[0.98-2.98]\times10^{-3}$ Hz and $[5.8-10.5]\times10^{-4}$ Hz, respectively. The time lag of a light curve in each narrow energy bin is calculated with respect to the light curve of a reference band from $0.3-0.8$ keV.

$\sim 5\,R_g/c$ (for $M_{\rm BH}=2\times10^6 M_\odot$; Zhou & Wang 2005). The full lag-energy plot for the fast variability shows that the lags associated with the Fe-K line emission feature are significant across the broad 4–7 keV band (figure 2.10). To date, there are ~ 20 AGNs where such Fe-K reverberation lags have been measured, with delay time (=lag amplitudes) of $1-9\,R_g/c$ at frequencies of $\sim c/100\,R_g$ Hz (figure 2.11; Kara et al. 2016). These three observational facts, broad line profiles, rms dips, and reverberation lags, are essential to understanding Fe-K line production mechanism, and thereby to reveal structure and geometry around SMBH.

2.4 Models to explain Fe-K features

Several models have been proposed to explain the broad Fe-K spectral features and their variability. Below, representative models are explained.

2.4.1 Relativistic light-bending model

The Fe-K features may be explained by extreme relativistic disc-reflection around a high spin BH (e.g., Fabian et al. 1989). When a primary photon from the X-ray corona is reflected at the inner region of the disc, strong gravitational redshift affects the reprocessed spectrum, and the Fe-K fluorescent line is skewed. Figure 2.12 illustrates how the Fe-K line is skewed. First, under Newtonian mechanics, the line is split into two due to Kepler motion of the

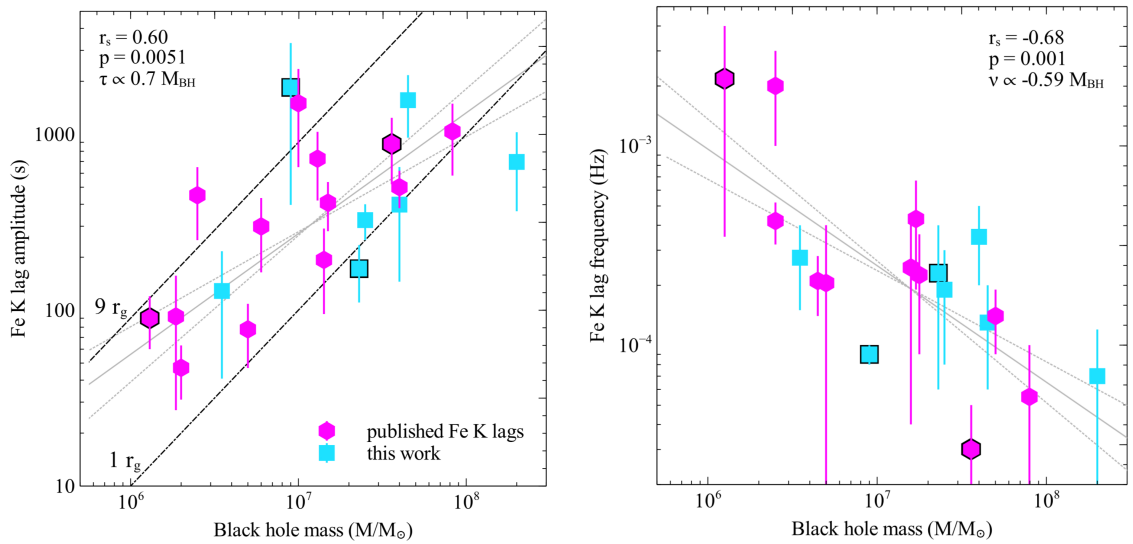

Figure 2.11: Lag parameters for different AGNs (Kara et al. 2016). (left) Fe-K lag amplitude versus BH masses with previously detected ones (magenta) and ones newly detected in Kara et al. (2016). The black diagonal dot-dashed and dashed lines show the time delay of 1 and 9 R_g. Sources with optical reverberation mass estimates are highlighted with black outlines. The grey line shows the best-fitting linear model and 1σ errors. (right) The frequencies where the Fe-K lag are seen versus BH masses.

disc. Second, the blue side of the line is enhanced due to beaming effect in special relativity. Third, the whole energy of the line moves redshifted due to the strong gravitational field. As a result, summation of the reflected line at every radius produce a skewed and broadened line.

The strongest relativistic reflection is required to explain the observation. The radius of ISCO becomes smaller as the spin is faster. When the spin parameter is theoretically maximum (i.e., $a = 0.998$), the ISCO radius becomes $1.24\,R_g$, and strong gravitational redshift is produced. In order to illuminate the inner edge, this model requires a compact corona ($\lesssim 1\,R_g$) just above the central BH ($\lesssim 10\,R_g$), which is often called as a "lamp post".

In order to explain the spectral variability in this framework, the "relativistic light bending model" has been considered (e.g., Miniutti et al. 2003; Miniutti & Fabian 2004). In this model, the lamp post moves along the rotation axis without changing the intrinsic luminosity. When the source height is smaller, primary photons with a power-law spectrum are less likely to escape from the strong gravitational field in the vicinity of the BH and rather likely to be trapped, so the Power-Law Component (PLC) becomes fainter. On the other hand, the Reflection-Dominated Component (RDC) hardly varies with a smaller height, because larger parts of the photons fall into the BH itself. In this manner, variations of PLC and RDC are totally different, and the variability amplitudes are expected to be reduced in the Fe-K band where RDC is dominant. In addition, a light-travel distance from the lamp to the accretion disc is about several R_g (e.g., Kara et al. 2013b; Cackett et al. 2014). Therefore, the observed reverberation lags with short amplitudes ($\lesssim 10\,R_g/c$) may be expected.

Here, we point out potential problems in the relativistic light bending model. First, the rms dips and Fe-K lags require opposite patterns of the RDC variability. The RDC

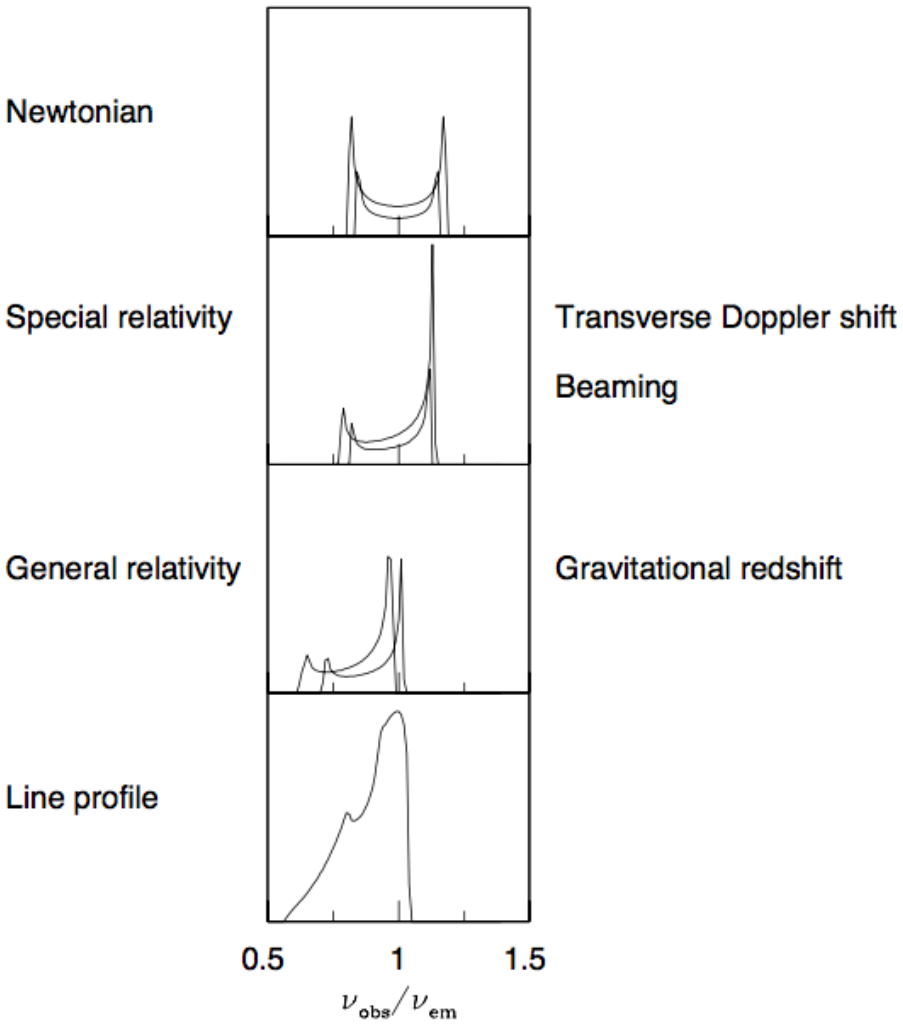

Figure 2.12: The broad iron line profile caused by Doppler shifts, relativistic beaming, and gravitational redshift (Fabian et al. 2000). The upper panel shows a symmetric double-peaked profile from a Kepler disc. The second panel shows effects of transverse Doppler shift and relativistic beaming, and in the third panel gravitational redshift is included. These produce a skewed and broadened line profile shown in the bottom panel.

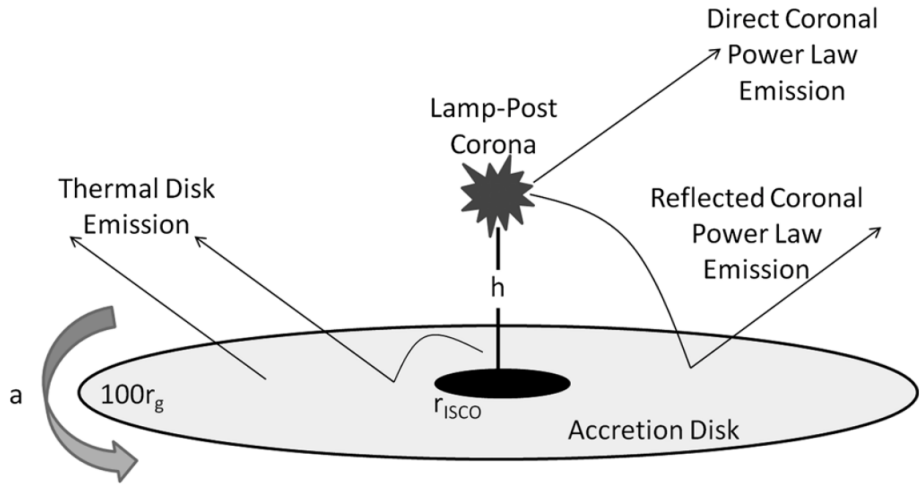

Figure 2.13: Sketch of the lamp post model (Hoormann et al. 2016). Some X-ray photons emitted from the lamp post corona directly reach the observer, some illuminate the accretion disc around the Kerr BH, and the rests fall into the BH.

flux and spectral shape have to be rather constant to explain the rms dips. For example, the rms dip of MCG–6-30-15 requires a variable PLC and the "perfectly-constant" RDC (Miniutti et al. 2007). However, if RDC were perfectly constant, the reverberation lags would not emerge. Thus, the RDC variability has to be well-balanced to make the rms dips and the reverberation lags simultaneously. Second, the Fe-K line profiles and lags require different iron abundances. The iron overabundance ($3 - 20$ solar) is commonly required to explain the observed strong Fe-K line in the relativistic light bending model (e.g., Fabian et al. 2002a; Chiang et al. 2015). On the other hand, numerical simulations show that the solar iron abundance is sufficient to explain the reverberation lags (Cackett et al. 2014; Emmanoulopoulos et al. 2014). Moreover, some argued that the observed deep rms dips cannot be fully explained only by the relativistic light bending model (Inoue & Matsumoto 2003; Życki et al. 2010). Therefore, we have to carefully examine whether this model can quantitatively and consistently explain the observations.

2.4.2 Partial covering model

Tanaka et al. (2004) studied an energy spectrum of 1H 0707–495 obtained with *XMM-Newton* based on the partial covering concept, and found that the energy spectrum and its variations can be explained as due to changes in the partial covering fraction (figures 2.14). In this model, the cold absorbers partially cover the extended emission region and produce Fe-K absorption edge at ~ 7.1 keV. If the full covering occurs, the soft energy band would be totally absorbed, so the cold clouds have to only partially cover the source. The absorption edge mimics the seemingly broad emission line. The partial covering model has been successfully applied to various AGNs with the broad Fe-K emission features (e.g., Miyakawa et al. 2012; Mizumoto et al. 2014; Iso et al. 2016; Mizumoto & Ebisawa 2017; also see figure 2.15).

Inoue & Matsumoto (2003) proposed that the observed deep rms dips can be realised

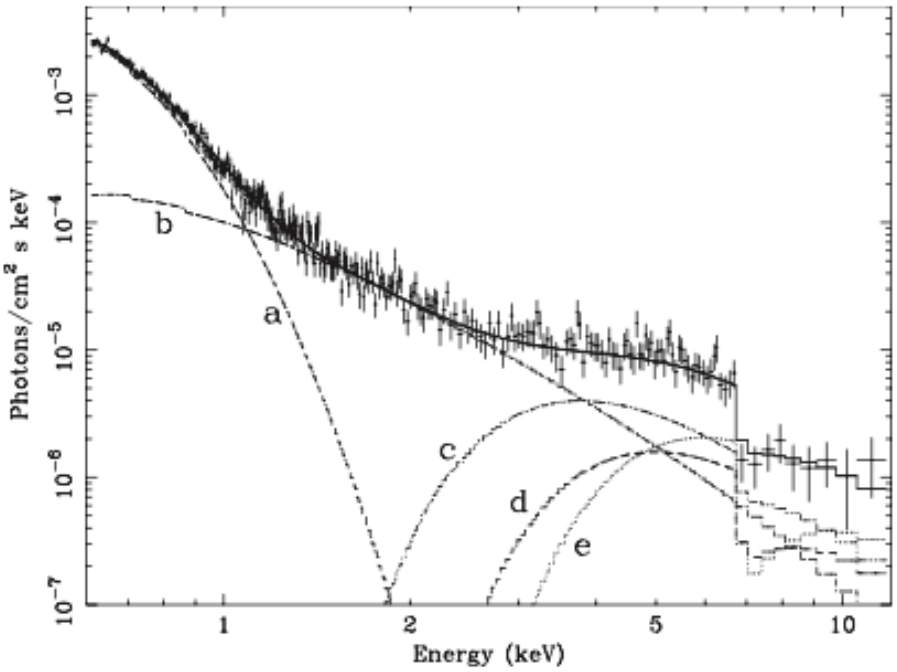

Figure 2.14: Model fitting of the partial covering model to 1H 0707–495 (Tanaka et al. 2004). The unfolded spectrum is shown with the model components: (a) the multi-colour disc, (b) the cut-off power-law, and (c), (d), and (e) are the components absorbed by the first absorber, the second absorber, and both the two absorbers, respectively. The absorption edge mimics the broad emission line.

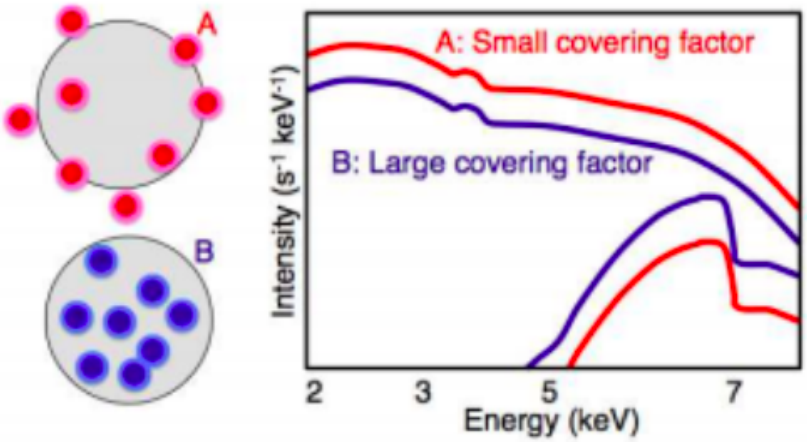

Figure 2.15: Schematic picture of spectral variations in the partial covering model (Mizumoto et al. 2016). When the covering fraction is small (A), the direct component is bright and the absorbed component is faint, and when the covering fraction is large (B), vise versa. Fluxes of the direct component and the absorbed component anti-correlate, and these variations cancel each other at around the Fe-K edge, which may produce the deep rms dip.

by absorption components with the variation timescale longer than that of the continuum. Mizumoto & Ebisawa (2017) analytically calculated the rms amplitudes expected from the partial covering model. This is formulated as

$$F(E,t) = \left(1 - \alpha(t) + \alpha(t) e^{-\sigma(E) N_{\rm H}}\right) P(E), \tag{2.20}$$

where $F(E,t)$ is the observed flux with energy E and time t, $\alpha(t)$ is the partial covering fraction, $\sigma(E)$ is the photoionisation cross-section, $N_{\rm H}$ is the column density, and $P(E)$ is the primary component. In this case, energy dependence of the rms amplitude due to change of the partial covering fraction is expressed as

$$\text{rms amplitude} \propto \frac{(1 - e^{-\sigma(E) N_{\rm H}})\alpha}{1 - (1 - e^{-\sigma(E) N_{\rm H}})\alpha}, \tag{2.21}$$

which monotonically increases with $\sigma(E)$. From lower energies toward the iron K-edge energy, $\sigma(E)$ continuously decreases, and at the iron K-edge, it suddenly increases. Consequently, the rms amplitude reaches its local minimum just before the iron K-edge with locally-minimal $\sigma(E)$, and the deep rms dips are reproduced. Figure 2.16 illustrates how the spectrum varies with different α (Yamasaki et al. 2016). The deep rms dip in 4–7 keV is explained by change of the partial covering fraction.

Miller et al. (2010b) pointed out that the observed small lag amplitude underestimates the light-travel distance due to the "dilution effect", such that the iron line band contains the continuum photons with no lags, as well as the lagged line emission. The observed lag is then given by the intrinsic lag multiplied by the fraction of the photons lagged by this light-travel time. Therefore, the short lag amplitudes do not necessarily indicate that the reprocessing matter is close to the light source. Indeed, the short lag amplitudes of 1H 0707–495 and other AGNs can be explained by distant clouds at $\gtrsim$ 1000 light-seconds, corresponding to $\gtrsim 100 - 600\, R_g/c$ (Miller et al. 2010a,b). Turner et al. (2017) also proposed that distant materials at $\sim 100\, R_g$ explain the lag-frequency plot of NGC 4051. However, in Miller et al. (2010a,b) and Turner et al. (2017), only the lag-frequency plots were shown and the observed Fe-K broad features in the lag-energy plots (like figure 2.10) have not been explained. Thus, the energy dependence of the lag amplitudes has yet to be studied.

2.4.3 Outflow model

Hagino et al. (2015) constructed a spectral model to reproduce the blueshifted absorption lines created by UFO using a Monte-Carlo tool named "MONACO" (see §5.1.1 for the explanation of this tool). They adopted a biconical configuration (Sim et al. 2010) and the velocity dispersion of β-law, where the wind is accelerated to the terminal velocity. The ionisation structure and 3-dimensional radiative transfer are comprehensively solved. As a result, they reproduced the energy spectra of PDS 456, which has an extremely strong outflowing wind. Hagino et al. (2016) pointed out that the energy spectra of PDS 456 and 1H 0707–495 (which has a typical broad Fe-K feature) are similar, especially in the Fe-K band. They also successfully applied basically the same outflow model to the energy spectra

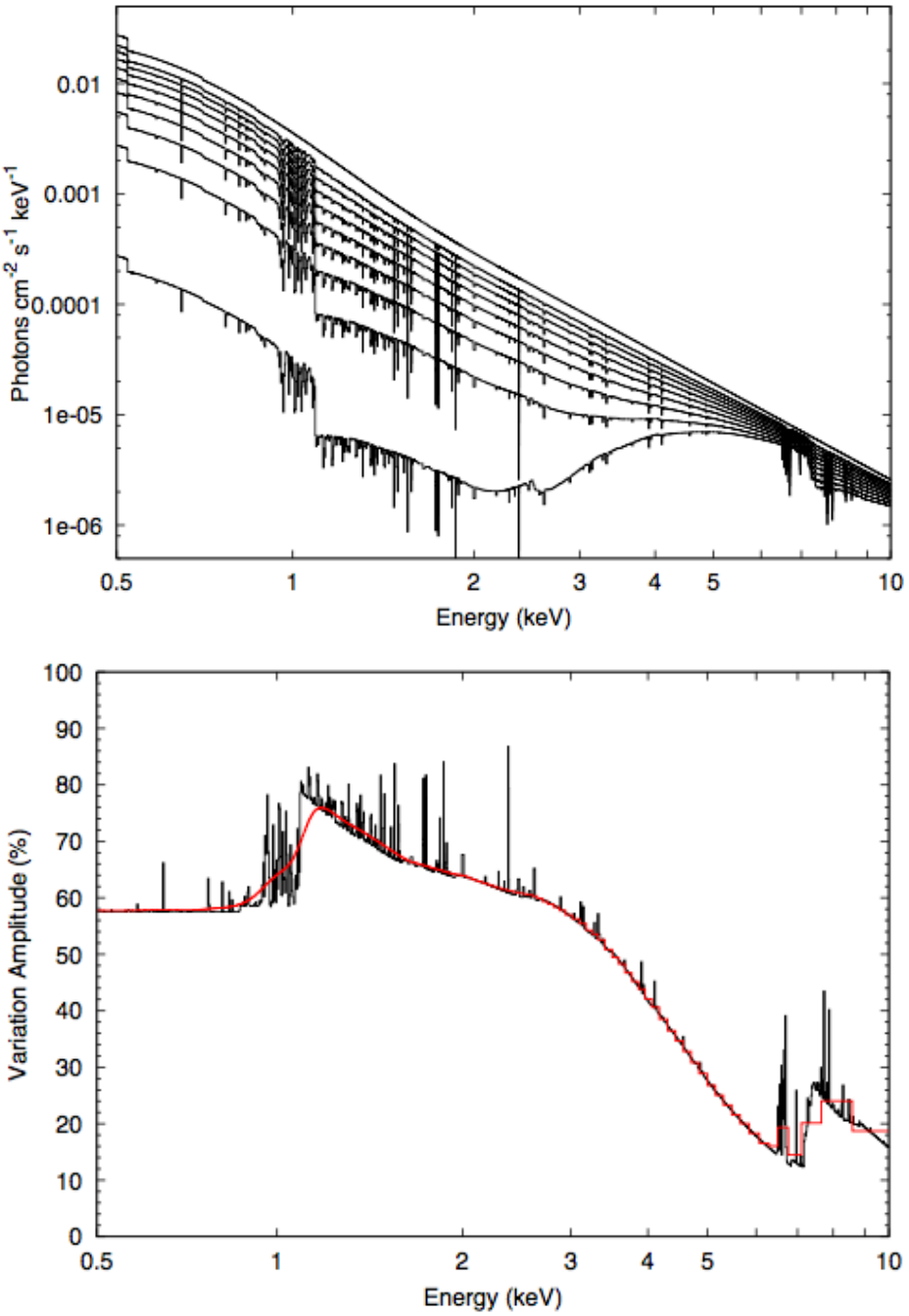

Figure 2.16: Model spectral variability of IRAS 13224–3809 due to change of the partial covering fraction (Yamasaki et al. 2016). (Upper) model spectra where α is 0.01, 0.1, 0.2, ..., 0.9, and 0.99 from top to bottom. Fe-K edge is seen at the $\sim$ 7.1 keV, which become deeper as the covering fraction increases. (Lower) Simulated rms spectra when α uniformly varies within 0.01–0.99. The black line is the one with an energy resolution of 1 eV, whereas the red line assumes the *XMM*/EPIC-pn response. The rms dips at the Fe-K energy band are reproduced due to change of the partial covering fraction.

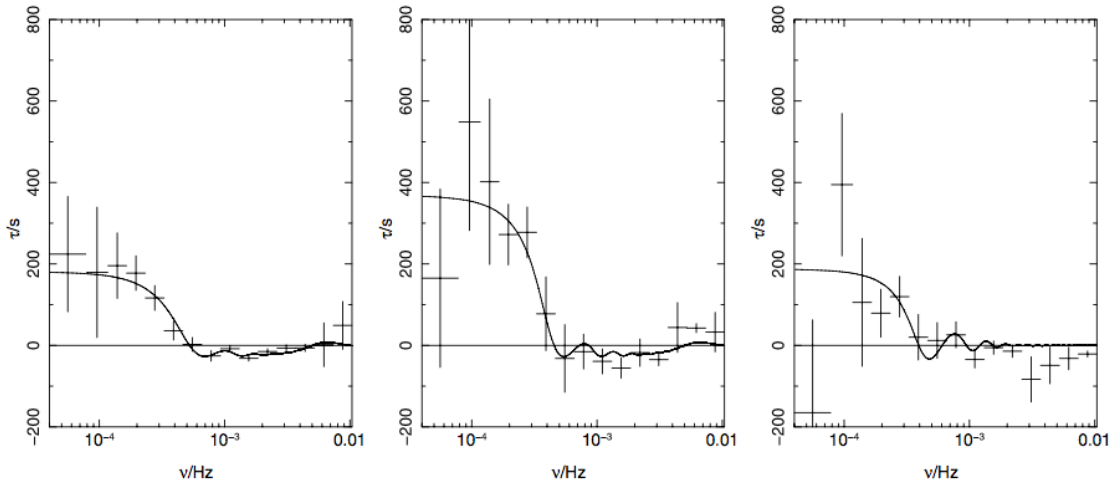

Figure 2.17: Lag-frequency plots of 1H 0707–495 with the medium (1–4 keV) versus soft (0.3–1 keV) bands (left-hand panel), hard (4–7.5 keV) versus soft bands (centre panel) and hard versus medium bands (right-hand panel). Solid curves show the ones expected from the distant clouds (Miller et al. 2010a).

of 1H 0707–495. In this model, especially deep and broad absorption lines explain the broad iron spectral feature. Variability of the absorption line is explained by the wind fluctuation, but the rms spectra have not been explained. Hagino et al. (2016) also introduced clumpy absorbers to explain variability in the soft energy band, and pointed out that the lag timescale can be explained by the clumps (Gardner & Done 2015), whereas the lag-energy spectra have remained to be studied.

2.4.4 Multi-powerlaw model

Noda et al. (2011a) calculated count-count plots of MCG–6-30-15, and reported a second spectral component which can be expressed as an absorbed and hard power-law varying independently of the first power-law emission. They also pointed out that the strong broadening of the iron line is not needed when the second power-law is taken into account. They invented a Count-Count Correlation with Positive offset (C3PO) method, and have reported presence of the similar second power-law components in many AGNs (figure 2.19; see Noda et al. 2011b; Noda et al. 2013a; Noda et al. 2014). This model refers to the central engine of AGNs, and details of the Fe-K variability are not explained. Although the (rather narrow) rms dip of NGC 3516 were explained with the distant reflection plus two primary components (Noda et al. 2013b), we speculate that the deep rms dip and the reverberation lags have to be explained by other mechanisms, such as absorbing/reflecting ambient clouds.

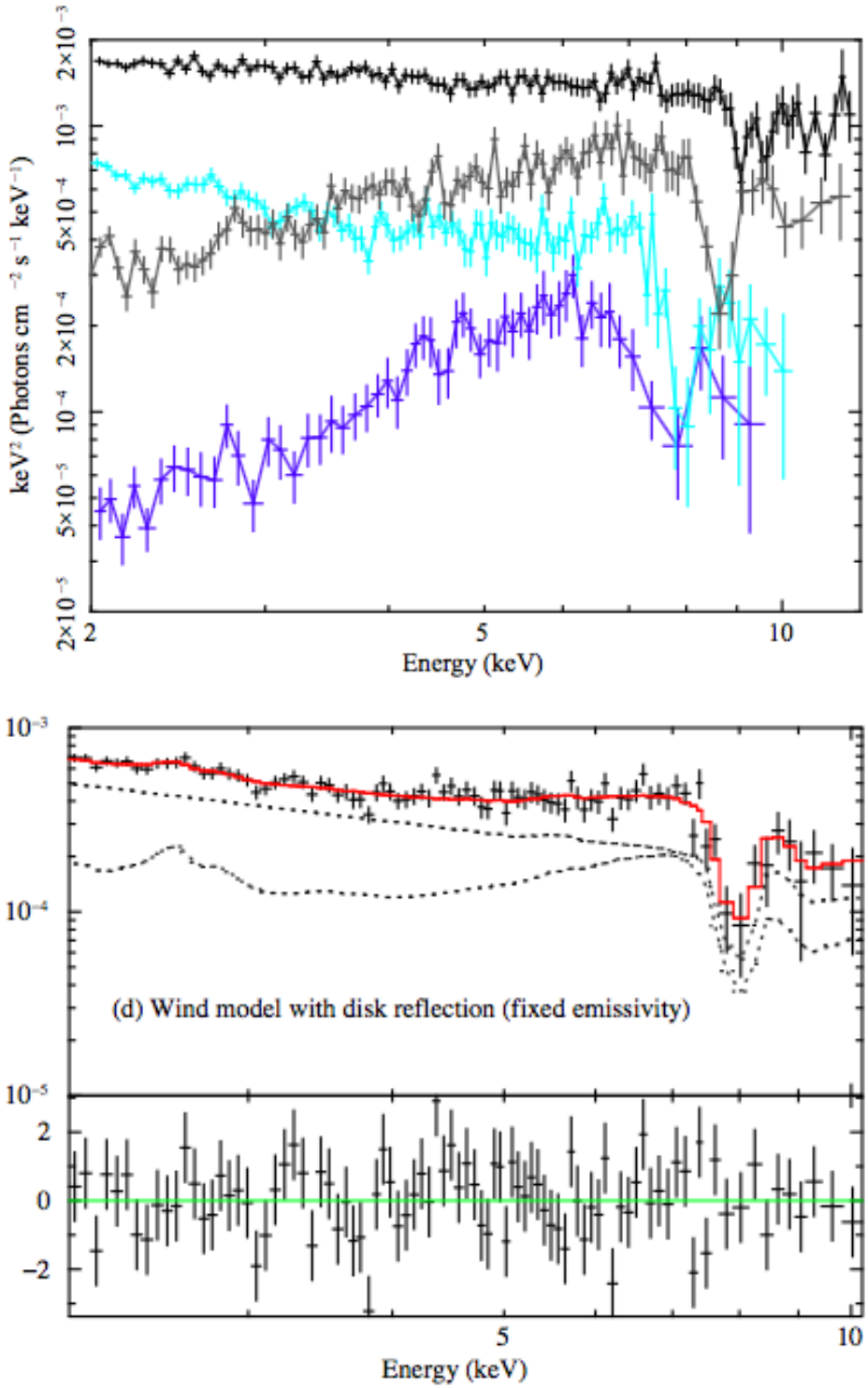

Figure 2.18: Energy spectra of 1H 0707–495 with the outflow model (Hagino et al. 2016). (Upper) Comparison between the spectra of PDS 456 (black and grey) and 1H0707 (cyan and blue). They have similarly deep features in the Fe-K band, though those in 1H0707 are broader and start at a lower energy than in PDS 456. (Lower) Energy spectrum of 1H0707 (black) fitted by wind model with blurred disc reflection (red). The lower panel shows the residuals.

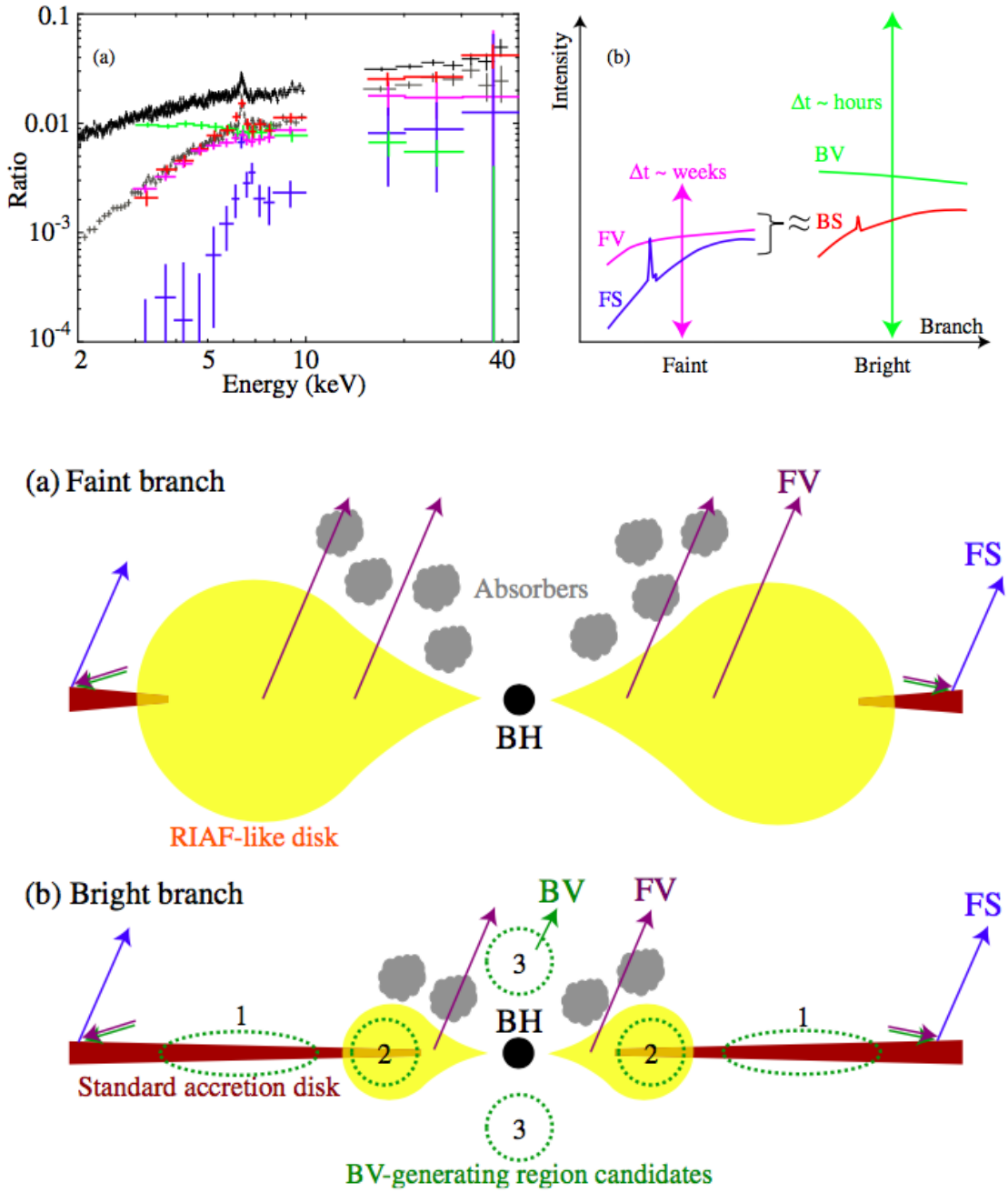

Figure 2.19: C3PO results and possible geometry (Noda et al. 2014). (Upper) Spectral components of NGC 3227. The faint-branch variable (FV; magenta) is very similar in spectral shape to the bright-branch stationary (BS; red), except the lack of the prominent Fe-K emission line. Instead, the iron line appears in the faint-branch stationary (FS; blue), whereas the bright-branch variable (BV; green) does not have. (Lower) Possible geometries of the central engine in NGC 3227, in the faint- and bright branches. In panel (b) there are three candidates of the BV emission regions; (1) small patch coronal regions located at the surface of the disc, (2) regions where the disc and the hot flow overlap, and (3) bipolar regions within 25 R_g from the central BH.

Chapter 3

Purpose of this thesis

As explained in the previous chapter, origin of the Fe-K features and time variability in AGNs are still under discussion. There are several models that explain each observational fact (line profiles, rms dips, and reverberation lags), but there are no studies to explain them simultaneously with the same physical condition. Therefore, we aim to construct a model to explain all the observational features self-consistently, envisioning to reveal AGN structure.

The proposed models may be categorised into two scenarios: the "disc-reflection scenario" and the "cloud-reflection scenario". The relativistic disc reflection model belongs to the disc-reflection scenario, which explains all of the Fe-K features with disc reflection around the Kerr BH. The X-ray emission region must be very compact, with a size of $\lesssim 1\,R_g$, to illuminate the innermost region of the disc. On the other hand, the partial covering model, the outflow model, and presumably the multi-powerlaw model propose that the Fe-K features are due to interaction with some kinds of clouds, which belong to the cloud-reflection scenario. The extended X-ray emission region is required especially in the partial covering model, because the clouds (with a size of $\sim 10\,R_g$) have to only partially cover the emission. The purpose of this thesis is to perform the numerical simulations of the two scenarios, compare the results with observations, and discuss which scenario is more plausible to explain the spectral variability in the Fe-K band of AGNs.

We use X-ray archival data of *XMM-Newton* (Jansen et al. 2001) to examine the models. The CCD detector on this satellite (*EPIC-pn*; Strüder et al. 2001) has a large effective area, which brings us good photon statistics. In addition, *XMM-Newton* has a higher orbit and thus longer orbital period (~ 48 hr) than other satellite such as *Suzaku* (~ 1.6 hr; Mitsuda et al. 2007), so that the long contiguous data can be obtained, which is essential to calculate time lags.

Chapter 4

Disc-reflection scenario

Contents

In this chapter, we compute the rms spectra and lag features simultaneously in the disc-reflection scenario (=the relativistic light bending model) using a ray-tracing technique. The goal is to investigate whether this scenario can quantitatively explain the observational Fe-K features simultaneously.

We select IRAS 13224–3809 as a typical object to investigate such Fe-K time features; it has the strong Fe-K spectral feature, the deep rms dip, and the significant reverberation lags. It has been observed with a very large program of *XMM-Newton*, and we can investigate details of the spectral variations. Its iron line is strongly skewed (e.g., Boller et al. 2003), the X-ray flux shows strong variability by more than one order of magnitude with a timescale of ~ 500 s (e.g., Dewangan et al. 2002), and the rms dip has an amplitude of $\sim 50\%$ (e.g., Yamasaki et al. 2016). Kara et al. (2013a) reported that Fe-K reverberation lags disappear at the high-flux periods, and proposed that this flux-dependence is explained by the large change of the source height; the Power-Law Component (PLC) becomes stronger with lower height, whereas the Reflection-Dominated Component (RDC) is hardly variable, so that lag features are more diluted by the contamination of the PLC. Each observational feature has been explained in the disc-reflection scenario, but there has been no attempt to explain them in the same calculation code.

4.1 Model and assumption

We briefly explain the model used in this chapter (see details in Appendix A). We show in figure 4.1 the schematic picture for the model. A distant observer observes the iron line reverberation due to a static X-ray emitter close to the prograde geometrically-thin accretion disc around a rotating BH. The lamp post is assumed to emit an instantaneous and isotropic X-ray pulse in its inertial frame. The gas element of the accretion disc is postulated to be in Keplerian motion, and the velocity components in the radial and polar directions are neglected. Radii of the inner and outer edges of the disc are fixed to be $r_{\rm ms}$ and $100\,R_g$, respectively, where $r_{\rm ms}$ is the radius of the marginally stable orbit. The $r_{\rm ms}$ value is calculated as

$$\begin{aligned} \frac{r_{\rm ms}}{R_g} &= 3 + Z_2 - \sqrt{(3-Z_1)(3+Z_1+2Z_2)} \\ Z_1 &= 1 + (1-a^2)^{1/3}\left\{(1+a)^{1/3} + (1-a)^{1/3}\right\} \\ Z_2 &= \sqrt{3a^2 + Z_1^2}, \end{aligned} \tag{4.1}$$

where $a = J/M_{\rm BH}^2$ is a spin parameter and J is the angular momentum of the BH. The light bending effects, Doppler effects, and gravitational redshift are taken into account. The total mass of the disc is assumed to be negligible compared to the BH mass.

We numerically calculate trajectories of the photons emitted from the static source with a point-like geometry. Some photons directly reach the observer along the path $\ell_{\rm p}$, which is regarded as the primary component. Other photons illuminate the accretion disc along the path $\ell_{\rm d}$ and causes the fluorescent iron line and the reflected continuum emission, which reach the observer along the path $\ell_{\rm r}$. We assume the lamp post located on the rotation

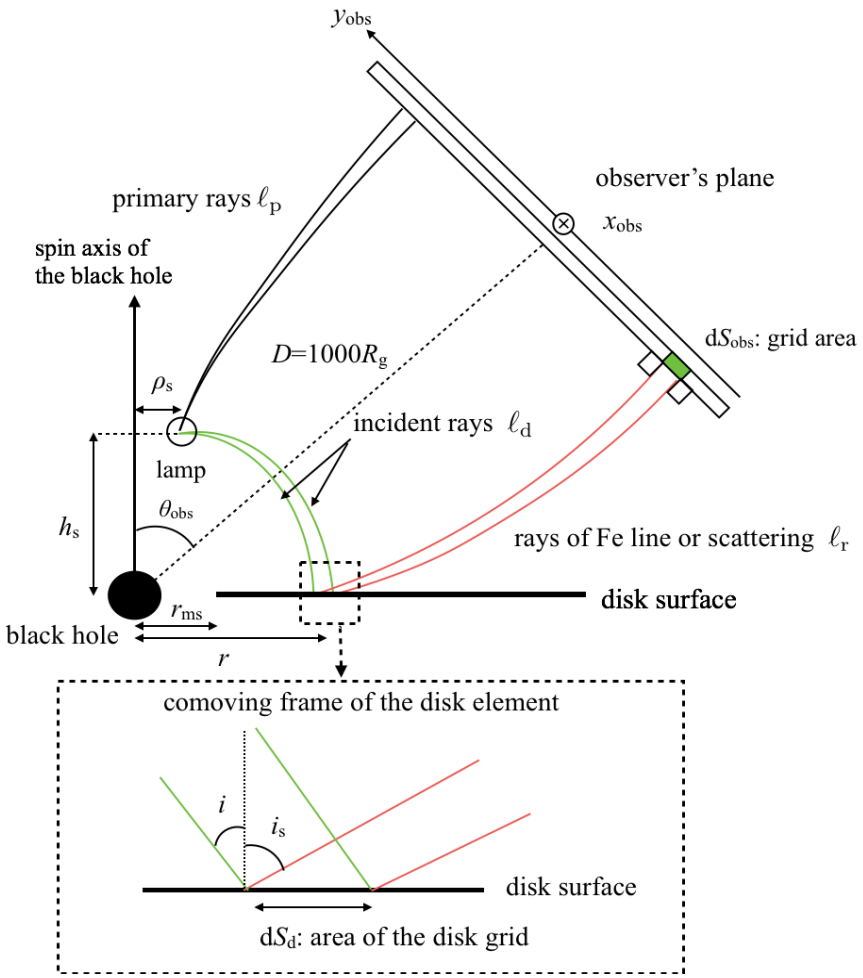

Figure 4.1: Schematic picture of the relativistic light bending model. The X-ray emitter has the point-like geometry and radiates an isotropic X-ray flare in its inertial frame. The accretion disc lies in the equatorial plane and is geometrically-thin and optically-thick. The radius of the inner edge of the disc is equal to that of the marginally stable orbit, $r_{\rm ms}$. Here, $h_{\rm s}$ and $\rho_{\rm s}$ are the height and the radial position of the source, $\theta_{\rm obs}$ is the viewing angle, D is the distance between the BH and the centre of the observer's plane. $\ell_{\rm p}, \ell_{\rm d}$, and $\ell_{\rm r}$ represent the photon path lengths of the primary, incident, and scattering orbits, respectively. Area elements of the observer's plane and the disc surface are denoted as $dS_{\rm obs}$ and $dS_{\rm d}$, respectively. In the comoving frame of the disc element, i and $i_{\rm s}$ are the incident and scattering angles, respectively. The $x_{\rm obs}$-axis is parallel to the equatorial plane of the BH ($\otimes$), and the $y_{\rm obs}$-axis is perpendicular to the $x_{\rm obs}$-axis.

axis (e.g., model A in Niedźwiecki & Miyakawa 2010). Intrinsic luminosity of the primary source is assumed to be invariable, and thus only the change of the heights h_s above the disc induces observed variability. The observed spectra were computed for different h_s. The heights were linearly spaced with $\Delta h = 1$ at $h \geq 3$ and $\Delta h = 0.2$ at $h < 3$ where $h = h_s/R_g$, following Niedźwiecki & Miyakawa (2010), which means that the h distribution is larger for $h < 3$. The h range was set to be $2.2 \leq h \leq 10$. Calculations are performed for four spin parameters ($a = 0$, 0.6, 0.9, 0.998). The photon index of the primary power-law spectrum is fixed at 2. We assume a high inclination angle ($i = 60$ deg), which is applicable for IRAS 13224–3809 (Boller et al. 1997; Parker et al. 2017). Calculations for the low-inclination case ($i = 30$ deg) are described in Appendix B.

4.2 Products

4.2.1 Energy spectra

Figure 4.2 shows h dependence of the primary and reflected spectra for different a. Find the red lines in the top left panel for explanation ($a = 0$ and $h = 9$ case): The horizontal line shows the primary spectrum, whereas the curved one shows the reflected spectrum. In the reflected spectrum, Fe-K lines, as well as the absorption edges, are skewed due to the gravitational redshift and the Doppler effect. As h decreases (see other colours in the same panel), the effect of the gravitational redshift becomes stronger, fewer photons escape from the gravitational field, and both the observed iron line fluxes and the primary component become smaller. On the other hand, Doppler effect of the disc has little dependence on h, such that the blue cut-off energies are unchanged. When a increases (see red lines in the other panels), the inner edge of the disc moves inward and the line is more strongly skewed by the gravitational redshift. Therefore, the low-energy tail reaches the softer band and the line becomes broader.

The right panel of figure 4.2 shows variations of the PLC flux, the RDC flux, and the equivalent widths (EW) of the iron line (=RDC flux/PLC flux), where the PLC flux shows the 6.4 keV flux and the RDC flux shows the integrated flux over the iron line (Miniutti & Fabian 2004). When $a \lesssim 0.6$, variations of the RDC and PLC fluxes are similar, so the EW is rather flat against significant change of h. In the larger spin cases ($a > 0.9$), the RDC flux is almost flat due to the light-bending effect in the h range of $\sim 5 - 10$ while the PLC flux is more significantly variable; this is considered to be the cause of the Fe-K dip in the rms spectrum.

4.2.2 Spectral variability

We compute 12 simulated spectra for different h ($= 2.2 - 10$) and calculated fractional variability amplitudes ($F_{\rm var}$; Edelson et al. 2002) using the following equation:

$$F_{\rm var}(E) = \frac{1}{\langle X \rangle} \sqrt{S^2 - \langle \sigma_{\rm err}^2 \rangle}, \tag{4.2}$$

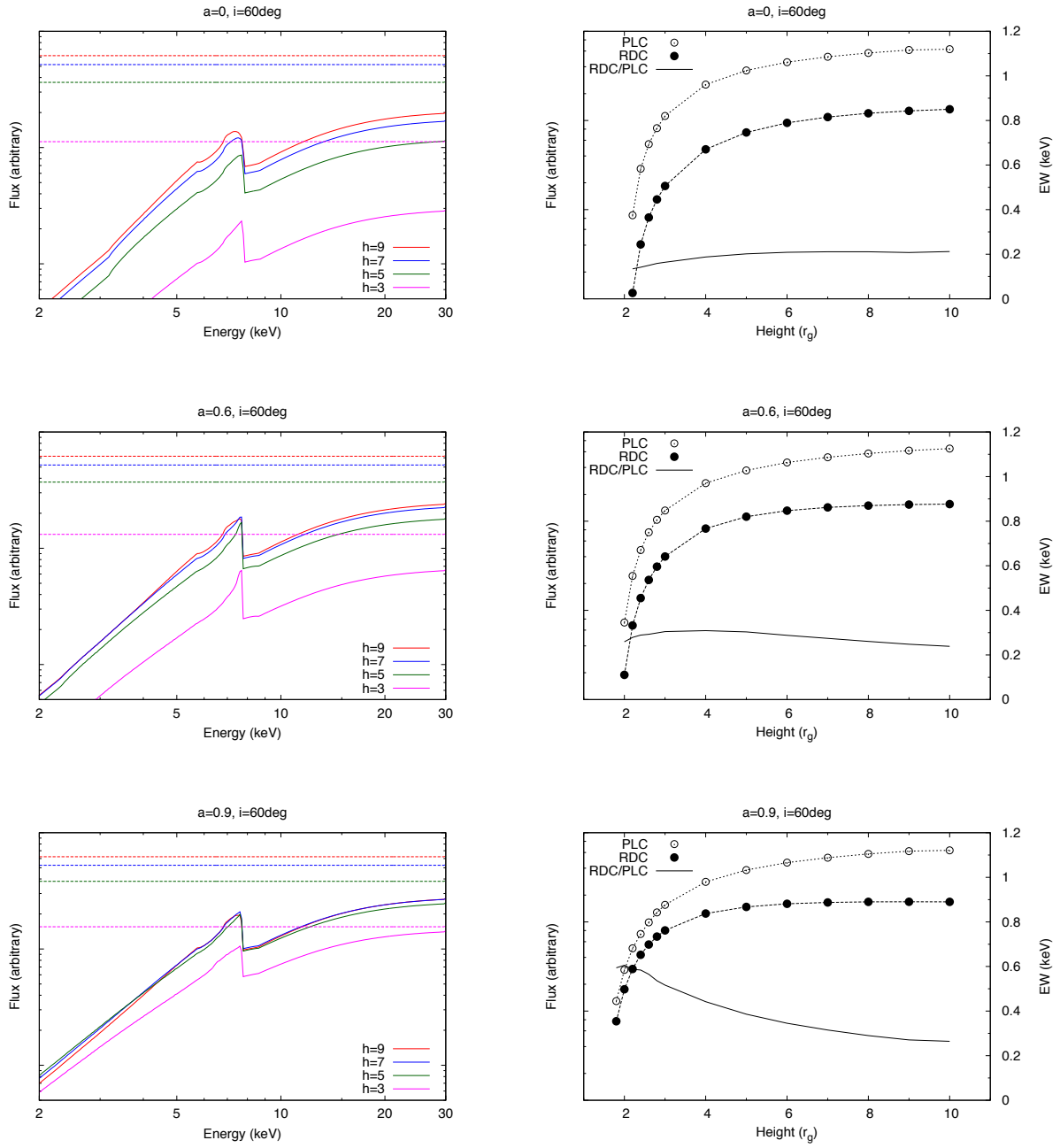

Figure 4.2: (Left) Primary and reflected (iron line + Compton reflection) spectra for different a and h, shown by dashed and solid lines, respectively. The vertical axis shows the energy flux (an arbitrary unit). (Right) The PLC (flux at 6.4 keV) and RDC (integrated over the iron line) fluxes as a function of h. The iron line EW $\equiv$ RDC/PLC is also shown in the solid line. Units of flux are arbitrary, whereas that of EW is given in keV.

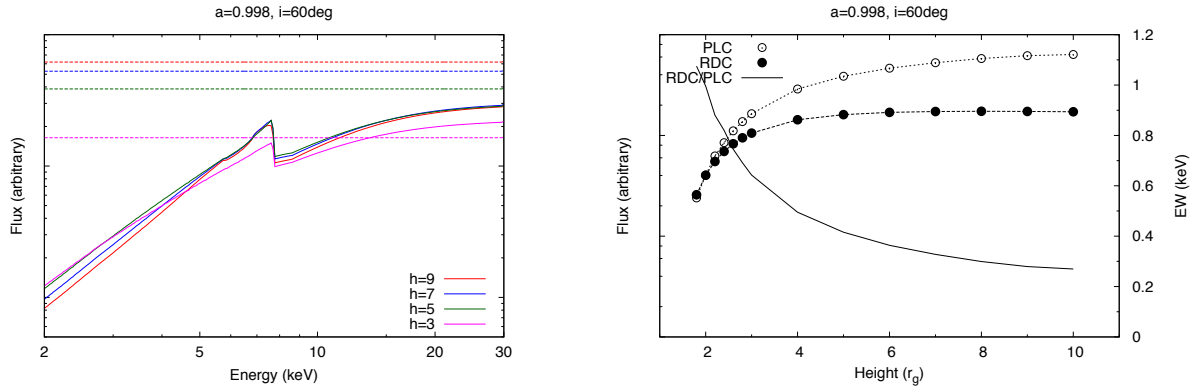

Figure 4.2: *Continued.*

where X_i is the photon count in the energy bin of interest for the i-th among the 12 simulated spectra, $\langle X \rangle$ is the mean counts, S^2 is the variance of $\{X_i\}$, and $\langle \sigma_{\rm err}^2 \rangle$ is the mean error squared of $\{X_i\}$, which is assumed to be null in our calculations. We assume that h varies continuously between 2.2 and 10. We also calculate the rms spectra assuming different variation pattern of h (such that h variation follows the sinusoidal function), only to find that the resultant rms features hardly change.

Figure 4.3 shows the resultant rms spectra. In the zero spin case, variations of the PLC and RDC fluxes are similar and EW of the iron line is constant against different h (figure 4.2), so the rms spectrum is rather featureless. In the spinning case, RDC varies less than PLC (figure 4.2), and both Compton reflection and iron line reduce variation amplitudes. In particular, the rms dip gets deeper and broader for the higher spin ($a \geq 0.9$). The relative dip depths at the 7–8 keV band are up to 20% in the maximum spin case.

4.2.3 Time lags

Next, we compute time lags. Figure 4.4 shows counts of the reflected photons in each time- and energy-bin when the X-ray source illuminates the disc with a delta function of time. This corresponds to the two-dimensional (2D) transfer function applied to the input photon spectrum. Interpretation of the 2D transfer functions are described in the preceding papers (e.g., Reynolds et al. 1999; Wilkins & Fabian 2013; Cackett et al. 2014). The delay time of a scattered photon is determined by the photon path difference from the primary photons, as well as Shapiro delays. The main difference among different a is that the energy-averaged responses in the high-spin cases have stronger peaks than in the low-spin cases. This is because the disc with high a has a larger surface area than that with low a and extends closer to the BH, whereas the response from the outer part of the disc is still the same (also see Cackett et al. 2014).

The frequency-dependent lag, $\tau(f)$, is defined as

$$\begin{aligned} \tau(f) &= \arg[C(f)]/(2\pi f) \\ C(f) &= \mathcal{S}(f)\mathcal{H}^*(f), \end{aligned} \tag{4.3}$$

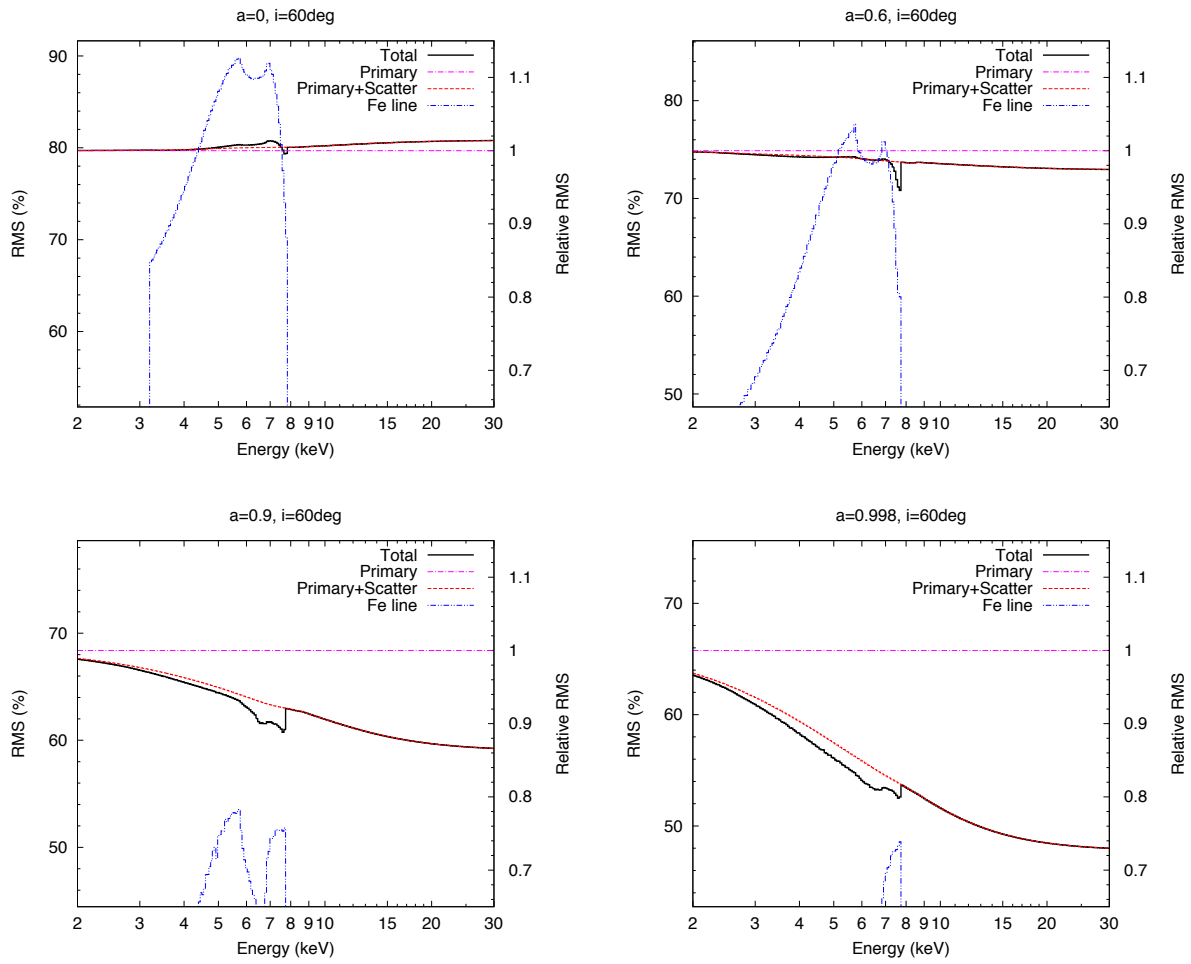

Figure 4.3: The rms spectra for different spectral components. The curves are for the primary component (magenta dot-dashed), the primary+Compton reflection (red dashed), and the iron line (blue dot-dot-dashed). The black solid curve indicates the total emission (primary+Compton reflection+iron line). The right axis show the relative amplitude where that of primary component is normalised as unity.

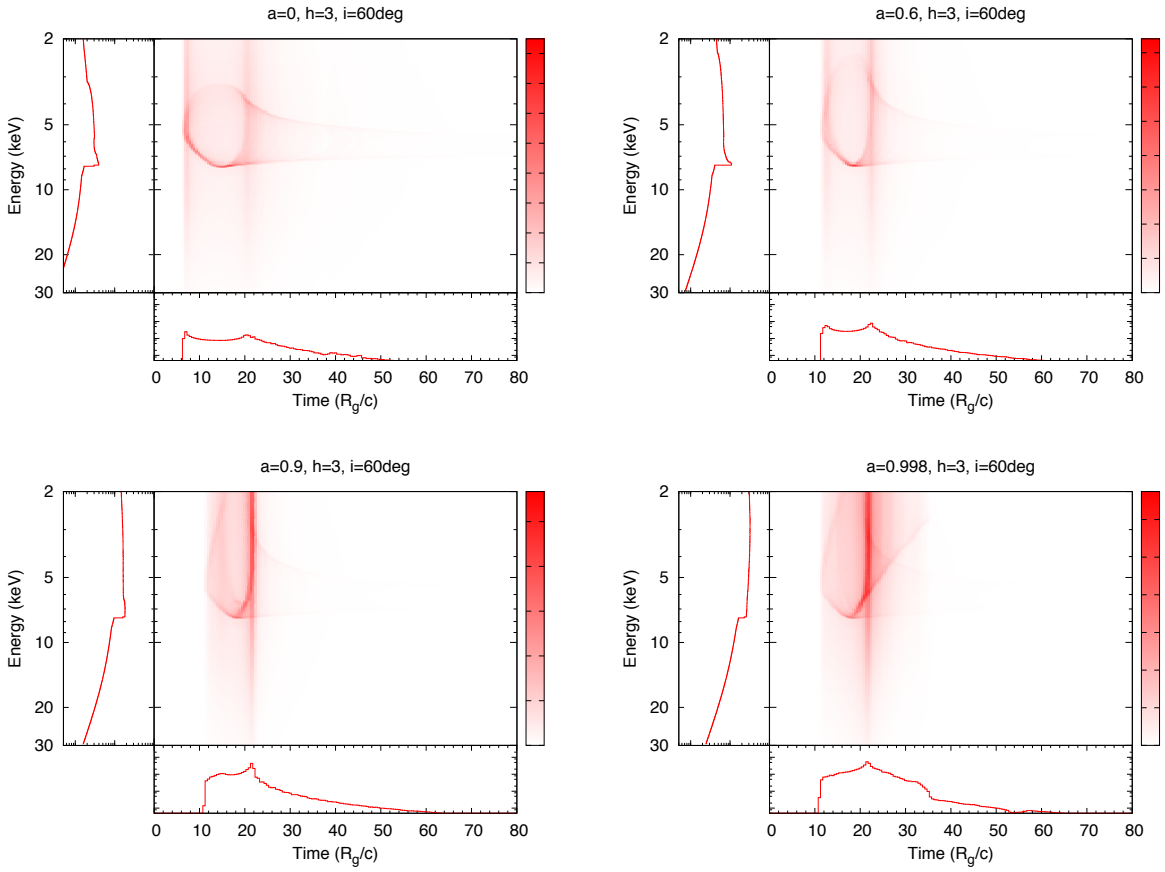

Figure 4.4: Main panels: Counts of the photons reflected on the disc for different i and a when $h = 3$. The X-ray source emits at once with a delta-function of time. The colour bar shows the photon counts in the arbitrary unit. Left-hand panels: Projection to the y-axis, which gives the total energy spectrum of all the reflected photons. Bottom panels: Projection to the x-axis, which gives the energy-averaged response

where * denotes complex conjugate and $\mathcal{S}(f)$ and $\mathcal{H}(f)$ are Fourier transforms of soft- and hard-band light curves, $s(t)$ and $h(t)$ (Vaughan & Nowak 1997; Nowak et al. 1999). We use the standard convention that a positive lag means that photons in the hard band lag behind those in the soft band (e.g., Kara et al. 2013b). In other words, $s(t)$ is a light curve in a reference band, and $h(t)$ is the one in an energy band of interest.

First, we calculate lags for each h value. An observed light curve at a given energy bin E is expressed as the sum of the primary emission and the reprocessed emission. The primary emission is expressed as $P(E)g(t)$, where $P(E)$ is the primary spectrum and $g(t)$ is the intrinsic flux variability, which is assumed to have no energy dependence, i.e., the continuum varies only in normalisation. We define $R(E,k)$ as photon counts of the reprocessed component in each energy-bin (E) and time-bin (k), which is shown in figure 4.4. The reprocessed emission is expressed as $\sum_{k=0}^{k_{\rm max}} R(E,k)g(t-kt_{\rm bin})$, where $t_{\rm bin}$ is a time bin-size of the light curve ($=0.5\,R_g/c$ in this section). We take $k_{\rm max}=400$, so we consider lags between 0–200 R_g/c. Here, the light curve at a given energy bin E is written as

$$l(E,t) = P(E)g(t) + \sum_{k=0}^{k_{\rm max}} R(E,k)g(t-kt_{\rm bin}), \tag{4.4}$$

and its Fourier transform is expressed as

$$\mathcal{L}(E,f) = P(E)\mathcal{G}(f) + \sum_{k=0}^{k_{\rm max}} R(E,k)\exp[-2\pi i(kt_{\rm bin})f]\mathcal{G}(f), \tag{4.5}$$

where $\mathcal{L}(E,f)$ and $\mathcal{G}(f)$ are Fourier transforms of $l(E,t)$ and $g(t)$. Thus the soft- and hard-band light curves and their Fourier transforms are expressed as

$$\begin{aligned} s(t) &= \sum_{E\in\,\text{soft band}} l(E,t) \\ h(t) &= \sum_{E\in\,\text{hard band}} l(E,t), \end{aligned} \tag{4.6}$$

and

$$\begin{aligned} \mathcal{S}(f) &= P_s\mathcal{G}(f) + \sum_k R_s(k)\exp[-2\pi i(kt_{\rm bin})f]\mathcal{G}(f) \\ \mathcal{H}(f) &= P_h\mathcal{G}(f) + \sum_k R_h(k)\exp[-2\pi i(kt_{\rm bin})f]\mathcal{G}(f), \end{aligned} \tag{4.7}$$

where $P_s = \sum_{E\in\,\text{soft band}} P(E)$, $R_s(k) = \sum_{E\in\,\text{soft band}} R(E,k)$, and P_h and $R_h(E)$ are those in the hard band. Therefore, equation (4.3) is calculated as

$$\begin{aligned} C(f) &= \mathcal{S}(f)\mathcal{H}^*(f) \\ &= \left(P_s + \sum_k R_s(k)\exp[-2\pi i(kt_{\rm bin})f]\right)\left(P_h + \sum_k R_h(k)\exp[2\pi i(kt_{\rm bin})f]\right)|\mathcal{G}(f)|^2 \end{aligned} \tag{4.8}$$

and

$$\tau(f) = \frac{1}{2\pi f} \arg \left[\left(P_s + \sum_k R_s(k) \exp[-2\pi i (k t_{\rm bin}) f] \right) \left(P_h + \sum_k R_h(k) \exp[2\pi i (k t_{\rm bin}) f] \right) \right]. \tag{4.9}$$

Note that the frequency-dependent lag amplitudes do not depend on the functional form of the intrinsic variation $g(t)$, as long as the lags are caused by the reverberation. Hereafter, we calculate lags based on equation (4.9).

Figure 4.5 shows the average lag-frequency plot with the probability distribution of h being flat within the variation range of $h = 2.2 - 10$. We use the 3–4 keV (least contribution from the reflected component) for the soft band, and 5–8 keV (where the Fe-K emission peaks) for the hard band. We assume the BH mass of $10^{6.8}\,M_\odot$(González-Martín & Vaughan 2012), i.e., $R_g/c = 30$ s. The results are normalised by the BH mass. The lag amplitude at the lowest frequency decreases with lower h corresponding to the light-travel time, but above the pivot point at $\sim [1-5] \times 10^{-4}$ Hz, the lag amplitude increases. The lag amplitude in the high-frequency range ($\gtrsim 5 \times 10^{-4}$ Hz) is larger for larger a because reflection in the innermost part of the disc is stronger. This effect is especially strong for small h (especially $h < 3$).

The same formalism is used to describe the lag-energy plots. We use each energy bin as a band of interest, $h(t)$, and the entire 2-30 keV (except for the energy bin of interest) as a reference band, $s(t)$, to get maximum statistics (e.g., Kara et al. 2016; Uttley et al. 2014). Figure 4.6 shows the lag-energy spectra for different a in the high frequency range (8×10^{-4} Hz). The reverberation Fe-K lags are seen in all the cases, but the broad features in the 4–7 keV band are only seen when $a > 0.9$. The lag amplitude is $\sim 1 - 2\,R_g/c$.

4.3 Comparison with IRAS 13224–3809

Our calculations show that the Fe-K rms dip ($\lesssim 20\%$) and the broad Fe-K lag with the amplitude of ~ 50 s are seen when $a > 0.9$. Here, we carefully investigate whether these results can quantitatively explain observations of IRAS 13224–3809.

4.3.1 Rms spectra

Figure 4.7 shows the observed rms spectrum of IRAS 13224–3809, in which results in the previous section are overplotted. We use all the archival data of this object with *XMM-Newton* between 2002 and 2016, whose total exposure time is 1.46 Ms. They were reduced with the Science Analysis System (SAS) v15.0.0, the latest calibration files, and the standard threads of SAS. We manually discarded high-background periods to get consecutive data as long as possible in each sequence. A time-bin width of the rms spectra is 1500 s, which corresponds to the frequency investigated in the lag features ($[5.8 - 10.5] \times 10^{-4}$ Hz). The variability amplitude at 7 keV is 55%, whereas that at 2 keV is 98%. In our calculations, when h varies within $2.2 - 10$ (red dashed in figure 4.7), the rms dip is produced but the

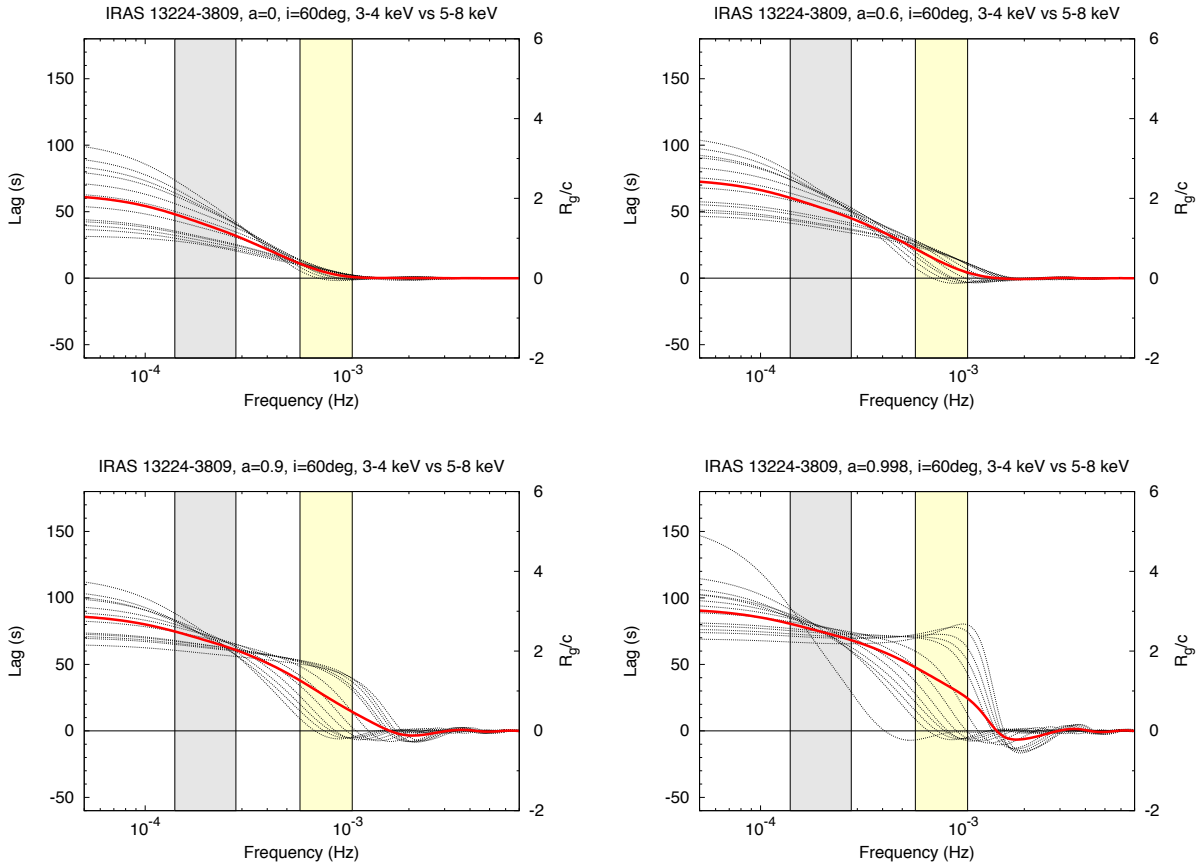

Figure 4.5: Lag-frequency plots, comparing 3–4 keV with 5–8 keV, with h values of 2.2, 2.4, 2.6, 2.8, 3.0, 4.0, 5.0, ..., 10.0 from bottom to top at the lowest frequency. A positive lag means that the hard band lags behind the soft. The BH mass is $10^{6.8}\,M_\odot$, i.e., $R_g/c = 30$ s, assuming IRAS 13224–3809. The yellow area shows $[5.8 - 10.5] \times 10^{-4}$ Hz where the Fe-K lag is seen in IRAS 13224–3809, and the grey shows $[1.4 - 2.8] \times 10^{-4}$ Hz where the lag disappear in the high-flux periods (see §4.3.2). The red solid line shows the average plot in $h = 2.2 - 10$. The plot of $h = 20$ is additionally shown only in the $a = 0.998$ case.

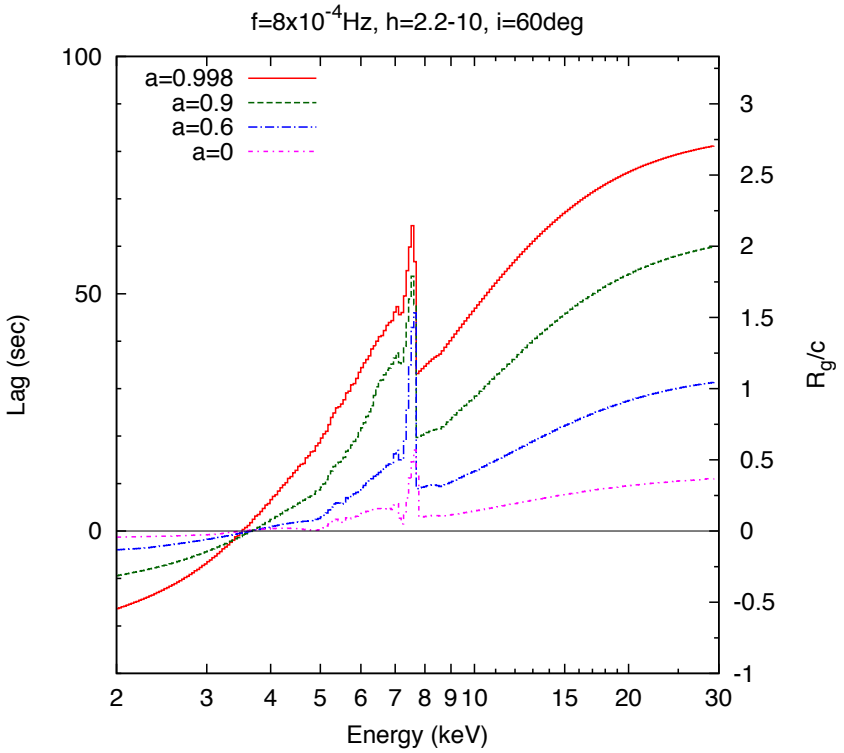

Figure 4.6: Lag-energy plots for different a at the frequency of 8×10^{-4} Hz.

depth is too shallow to explain the observation. We calculated the rms spectra with different h ranges (green dotted and magenta dot-dashed in figure 4.7), but none can explain the observed feature. Therefore we conclude that the observed rms dip cannot be explained by the relativistic disc reflection model when the iron abundance is solar.

Next, we intentionally change the iron line flux to explain the deep rms dip. We manually increase the iron flux by ten times, equivalently 10 solar overabundance of iron, and calculate rms spectra. As a result, the observed deep dip can be almost reproduced (blue solid). Therefore, we see that the extreme iron overabundance ($\gtrsim$ 10 solar) is required to explain the rms dip with the relativistic light bending model.

4.3.2 Lag features

We calculate the lag-energy spectrum of IRAS 13224–3809 in the frequency range of $[5.8 - 10.5] \times 10^{-4}$ Hz (figure 4.8), following Kara et al. (2013a). We use the same data in the rms spectrum. The Fe-K lag amplitude is about 80 s, which corresponds to $\sim 2 - 3\, R_g/c$. Indeed, the lag-energy plot obtained by our simulation is consistent with the observed one (red dashed, where reduced χ^2 is $6.30/9 = 0.70$). The lag amplitude becomes longer as the iron line flux (with time delay) is stronger. When the iron flux is ten times stronger (blue line), the lag amplitude gets more than 150 s and the reduced $\chi^2 = 31.73/9 = 3.53$, which is rejected with the 99.9% confidence. Thus, the iron abundance constrained by the lag feature ($\sim 1 - 2$ solar) contradicts the one derived from the rms dip ($\gtrsim$ 10 solar).

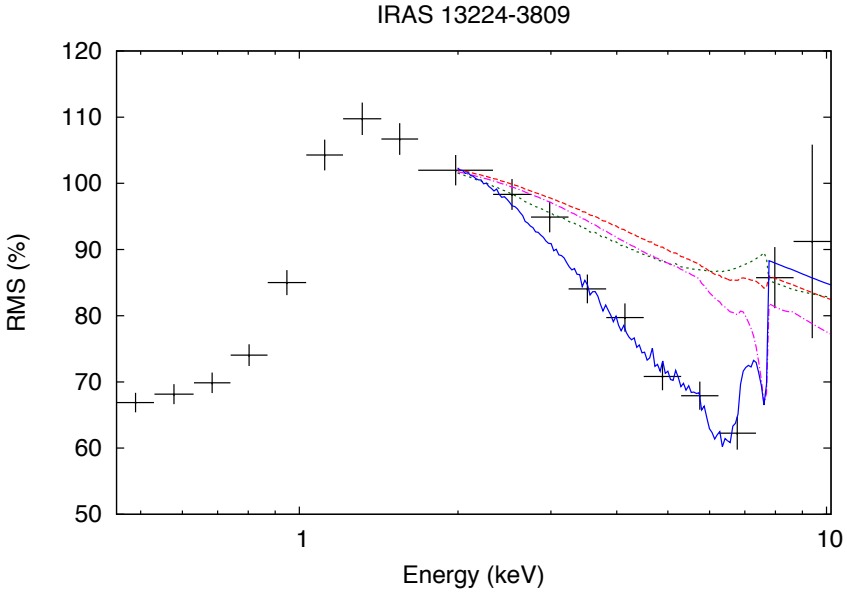

Figure 4.7: Observed rms spectra of IRAS 13224–3809 (black-solid bins) compared with the relativistic disc reflection model with $a = 0.998$, normalised at 2 keV. The red dashed, green dotted, and magenta dot-dashed lines are for the solar abundance with $2 \leq h \leq 10$, $2 \leq h \leq 3$, and $5 \leq h \leq 10$, respectively. The blue solid line is for 10 times overabundance of iron with $2 \leq h \leq 10$.

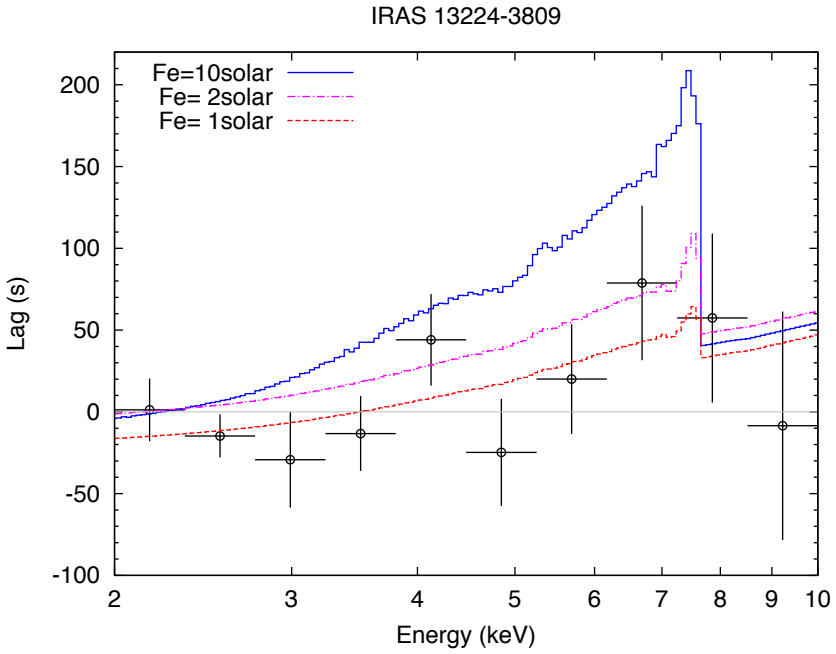

Figure 4.8: Observed lag-energy spectrum of IRAS 13224–3809 (black bins) in the frequency range of $[5.8 - 10.5] \times 10^{-4}$ Hz, compered with the relativistic disc reflection model with $a = 0.998$. The red dashed, magenta dot-dashed, and blue solid lines show when the iron abundance is equal to, twice, and 10 times of the solar abundance, respectively.

Kara et al. (2013a) reported flux-dependence of the Fe-K lags in this object. They examined lags from low- and high-flux intervals, where average count rates are different by one order of magnitudes. The Fe-K lags disappear in the high-flux period for $[1.4-2.8]\times10^{-4}$ Hz, whereas they are seen in the low-flux period for $[5.8-10.5]\times10^{-4}$ Hz. In the framework of the relativistic light bending model, this change may be explained by significant change of the lamp post height. As the lamp post height varies, the RDC flux is hardly variable and the PLC flux varies by an order of magnitudes, therefore the lag in the high-flux period is diluted by the strong PLC component. However, our calculation indicates that the lag is still clearly seen even when $h = 20$ (figure 4.5; $a = 0.998$ case). Assuming that the frequency where the lag amplitude gets to zero monotonically decreases with larger h, the height where the lag disappears should be $\sim 40\,R_g$. However, this clearly contradicts with the observed line profile; the line is hardly skewed and broadened with such a large source height (e.g., Fabian et al. 2002a).

4.3.3 Comments on the black-hole spin constraint

Some authors claimed that spin of IRAS 13224–3809 is tightly constrained to be almost maximum based on model fitting of the X-ray spectra, e.g., $0.990^{+0.001}_{-0.003}$ and 0.988 ± 0.001 (Fabian et al. 2013; Chiang et al. 2015). They proposed extremely-high emissivity indices $q\,(\gtrsim 9)$, where the disc emissivity per area at a radius r is proportional to r^{-q}. When the emissivity index is so high, the reflection component from the inner region of the disc is fully dominant, and thus the Fe-K line profiles are extremely sensitive to small change of a (i.e. change of $r_{\rm ms}$). We calculate the emissivity profiles and indices from our simulations (figure 4.9). In this figure, the emissivity index is up to ~ 6 at the innermost edge of the disc with the source height of $2\,R_g$ even in the maximum spin case, and such a high emissivity index of $q \gtrsim 9$ is possible only when the lamp locates within $2\,R_g$ from the central BH. Thus, the spin parameters cannot be constrained unless the source height is extremely small (see also Bonson & Gallo 2016). However, the relativistic light bending model requires height variations (typically $h = 2-10$), which makes contradiction. Also, we may tell whether $a < 0.9$ or $a > 0.9$ from the time variability (figures 4.3, 4.6), but it is very difficult to distinguish $a = 0.9$ from $a = 0.998$. Thus, we suggest that the BH spin values estimated from Fe-line spectral fitting or time variations are not trustworthy.

4.4 Summary of this chapter

In this section, we critically examined the disc-reflection scenario (=relativistic light bending model) by computing the energy spectra, rms spectra, and lag features, where a lamp post with the constant luminosity is moving vertically along the rotation axis. A ray-tracing technique is adopted including the full treatment of general relativity to calculate photon paths and delay times of the reflection. We try to explain Fe-K features of IRAS 13224–3809, which is a representative source to exhibit the characteristic Fe-K features. The observed rms dip may be reproduced when an extreme iron overabundance ($\gtrsim 10$ solar) is assumed. On

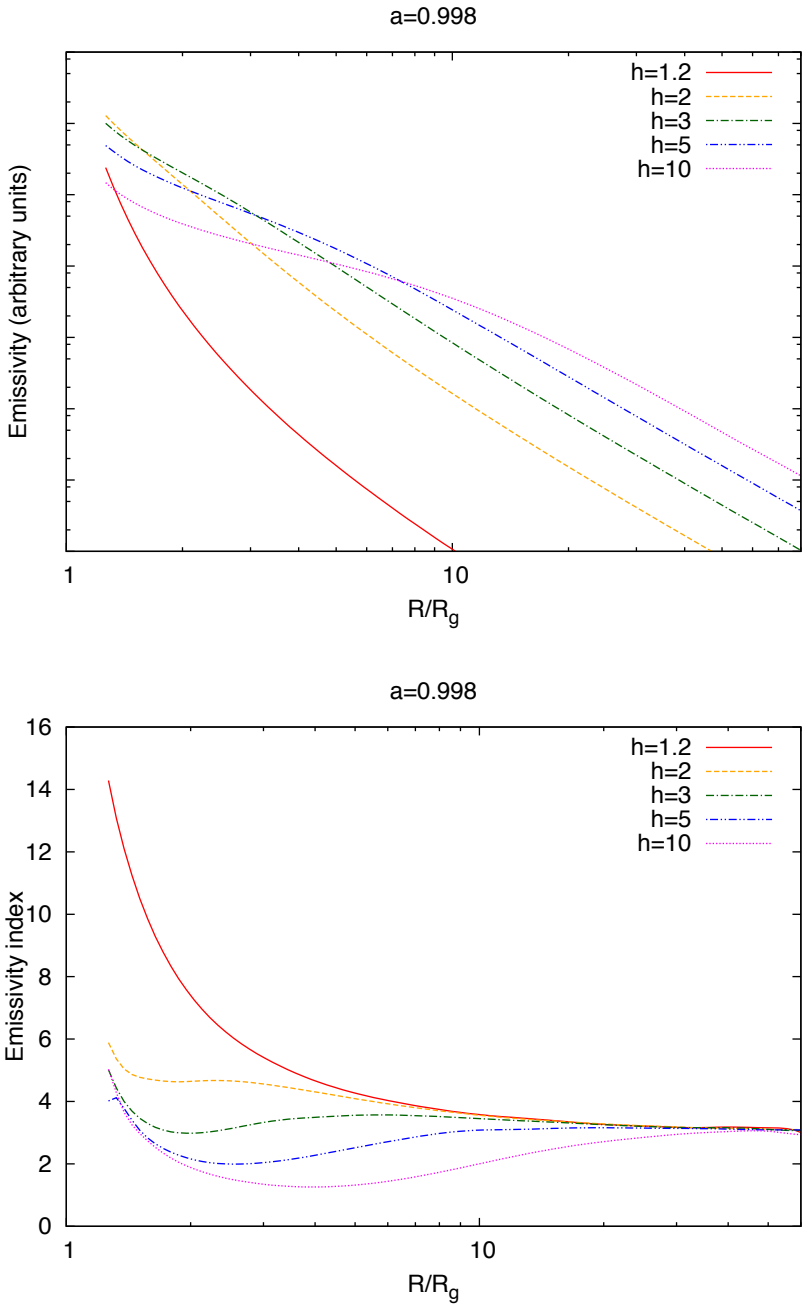

Figure 4.9: (Upper) Disc emissivity profiles, $\epsilon(r)$, calculated by our ray-tracing method for different lamp-post heights. (Lower) Emissivity indices, q, which is defined by $\epsilon(r) \propto r^{-q}$.

the contrary, the observed lag-energy spectrum requires solar abundance of iron; it clearly rejects the extreme iron overabundance. In addition, the observed diminution of the lag feature in the high-flux state needs a very large source height of $\sim 40\,R_g$, which contradicts the observed broad line profile. Consequently, we conclude that the relativistic light bending model is difficult to explain both the rms dips and reverberation lags in the Fe-K band simultaneously.

Chapter 5

Cloud-reflection scenario

Contents

We have shown in the previous chapter that the disc reflection scenario cannot explain all the observational facts consistently. Next, we try to explain the Fe-K spectral variability with the cloud-reflection scenario, assuming the neutral clouds (§5.2) and the ionised clouds (§5.3). As explained in §2.4, this scenario has been successful to reproduce the observed Fe-K line profiles and deep rms dips, therefore we aim to reproduce the observed lag features. We adopt a Monte-Carlo simulation method to calculate lags produced by the clouds; we compute interaction between incident photons and ambient clouds, investigate photon paths after interaction, and calculate time-delay of each photon.

5.1 Tools

5.1.1 MONACO

We adopt a Monte-Carlo simulation code, MONACO (MONte Carlo simulation for Astrophysics and COsmology; Watanabe et al. 2006; Odaka et al. 2011), which is a general-purpose framework for synthesizing X-ray radiation from astrophysical objects. This code employs the Geant4 toolkit library (Agostinelli et al. 2003; Allison et al. 2006) for photon transport in complicated geometries with physical processes for the interaction of photons based on original implementation (Odaka et al. 2011). We consider photoelectric effects followed by fluorescence emission, together with all scattering by electrons (i.e., Compton, Raman, and Rayleigh scatterings). These calculations can handle multiple scatterings and Doppler effects from velocity structure in the material.

We have to input geometry, physical parameters of the ambient matters (e.g., density, velocity, ion abundance, ion population) and the source spectrum into MONACO. A photon with an energy E_0 and a direction Ω_0 is generated at a time t_0 and a position x_0 in each trial. The photon with an initial condition $X_0 = (E_0, \Omega_0, t_0, x_0)$ is tracked by calculating its propagation and interaction with matter until escaping from the system or being absorbed. Once a photon escapes from the system, the parameters of the last interaction, $X_1 = (E_1, \Omega_1, t_1, x_1)$, are recorded. A schematic view is shown in figure 5.1. From these parameters, we can get information of energy spectra and time lags.

5.1.2 XSTAR

When the scattering material is ionised (§5.3), ionisation states are required to calculate interactions of photons in MONACO. Here we use XSTAR[1] (version 2.39; Kallman et al. 2004) to that end. XSTAR is widely used in X-ray astrophysics to calculate transfer of the incident radiation into the cloud, temperature, ionisation, atomic level populations at each point in the cloud, and transfer of the emitted radiation out of the cloud.

Input parameters in XSTAR are the source spectrum, gas composition (atomic abundances relative to solar), the gas density or pressure, and geometry. When the gas is optically thin, the state of the gas depends on the ionisation degree, so that results of one model

[1]Manual: https://heasarc.gsfc.nasa.gov/lheasoft/xstar/docs/html/xstarmanual.html

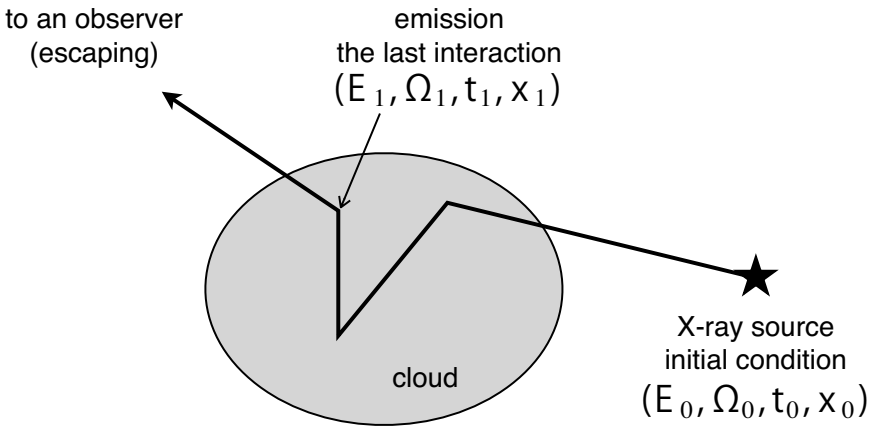

Figure 5.1: Schematic diagram of the Monte Carlo simulation in MONACO (Odaka et al. 2011).

calculation can be applied to a wide variety of situations. Calculation of the ionic level populations proceeds in two steps. First, ion fractions are calculated using total ionisation and recombination rates into and out of every ion. Second, the full kinetic equation is solved linking the various levels of the ions, including all processes in the database that links the bound levels of any ions. This includes collisional and radiative bound-bound transitions with continuum photo-excitation, collisional ionisation, photoionisation, and recombination for all the levels of each ion. The temperature of the gas is determined by solving equations of thermal equilibrium at each radius.

5.2 Reflection by neutral shell-like clouds

5.2.1 Setting

As a first step, a neutral shell-like cloud is assumed. Figure 5.2 shows the assumed geometry of the scattering medium, like a part of a spherical shell. The shell extent is from $R = 100\,R_g$ to $110\,R_g$ across zenith angles 45°–90° (i.e., $\Omega/4\pi = 0.7$). Photons emitted downwards are assumed to be blocked by the accretion disc; this might give a minor additional contribution to the lagged emission, which we neglected. We assume $M_{\rm BH} = 10^7\,M_\odot$, which means that the light-travel time to the shell is 5000 s.

We consider two cases for the shell dynamics. We first explore a static shell, and secondly assume that the shell has a typical outflow velocity from its launch point, i.e. $0.14c = 42,000$ km s^{-1} (Tombesi et al. 2011) and a typical turbulence of 1000 km s^{-1} (Hagino et al. 2015). We set the hydrogen radial column density ($N_{\rm H}$) of the shell as 2×10^{23} cm^{-2}. Incident photons have a power-law spectrum whose photon index is 2. The number of input photons is 7×10^8 in each case, and those photons are input as a delta function in time. We ignore photons below 2 keV because we focus around the Fe-K band.

Primary X-ray photons passing through the shell in the line-of-sight are along the red dashed line in figure 5.2, whose unit vector is $\vec{q}$. Some parts of photons in this path are

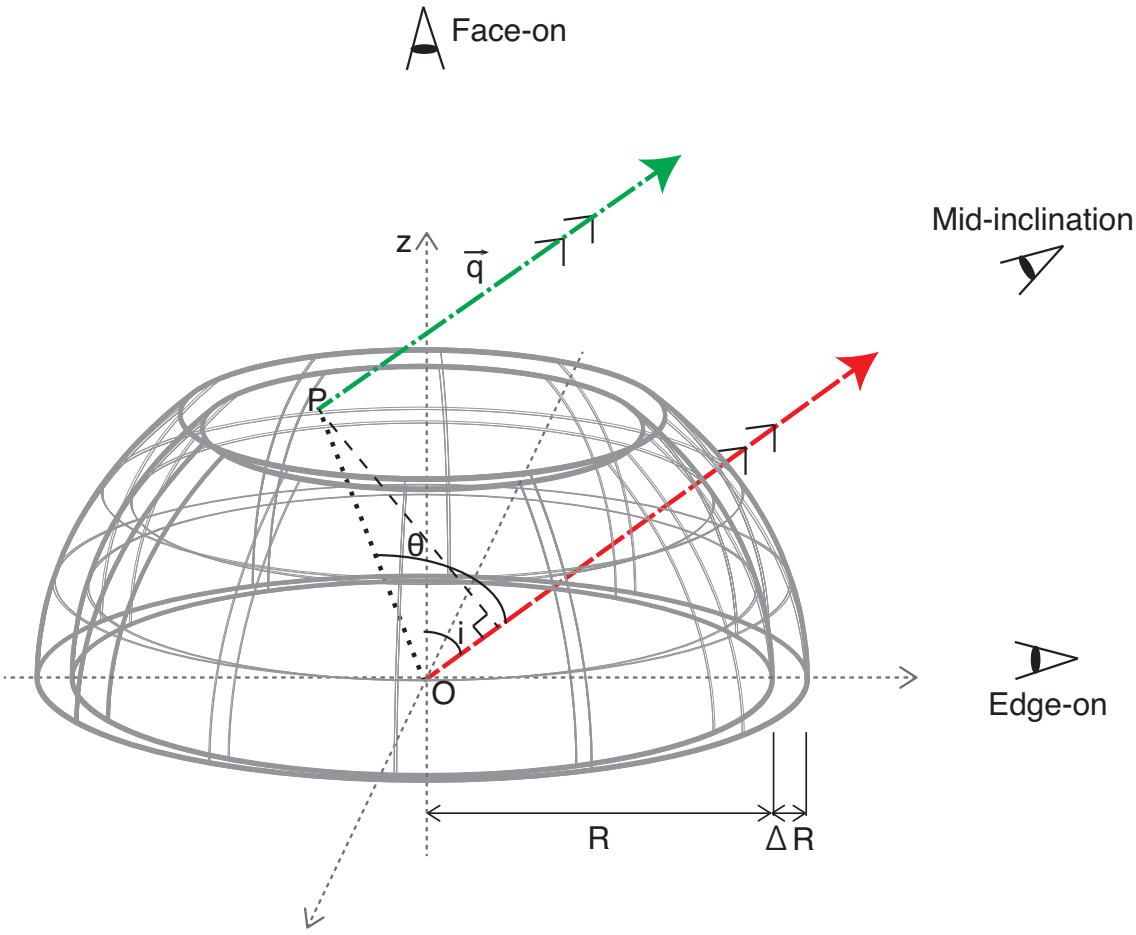

Figure 5.2: Assumed geometry of the ambient scattering medium and photon paths in our simulations. The scattering medium (grey solid line) is a ring-shaped part of the upper-half of a spherical shell, whose thickness (ΔR) is $0.1R$. The red dashed/green dot-dashed lines show paths of the primary/reprocessed photons toward the line-of-sight.

absorbed or scattered in the shell and do not reach us. The green dot-dashed line shows the path of a reprocessed photon. The point P is the location where the photon interacts last in the shell at a time $t_{\rm P}$ after being emitted from the central source, no matter how many times it has been scattered previously. This photon has a time-delay of $t_{\rm P} - (\vec{P}\cdot\vec{q})/c$. Since MONACO keeps track of $t_{\rm P}$, $\vec{P}$ and $\vec{q}$, we can calculate the time-delay of each scattered photon relative to the direct photons as well as a scattering angle $\theta \equiv \arccos(\vec{p}\cdot\vec{q})$, where $\vec{p}$ is a unit vector of $\vec{P}$.

We consider results along three different lines of sight, where the photon direction (in units of cosine of the zenith-angle, i) is between 14/15 and 15/15 (nearly face-on), between 7/15 and 8/15 (mid-inclination), and between 0/15 and 1/15 (nearly edge-on). This allows us to study how the lag features depend on the inclination angles.

5.2.2 Products

5.2.2.1 Spectra and transfer functions

The resultant spectra from the Monte-Carlo simulations have two components; the primary component without time delay and the reprocessed component with time delays. Figure 5.3 shows these spectral components for the three inclination angles, for the static shell and the outflowing shell. The primary components (red lines) in the edge-on and mid-inclination case are strongly absorbed by the near side of the shell in the line of sight. The absorption in the soft energy band is stronger in the outflowing shell, because the source spectrum is redshifted to lower energies in the wind rest frame due to the Doppler shift. The reprocessed components (green lines) have fluorescent Fe-K lines at 6.40 keV and 7.05 keV, an Fe-K edge at 7.1 keV, and a Compton hump above $\sim$20 keV. The Fe-K features in the outflowing shell are broadened, whereas they are sharp in the static shell.

Figure 5.4 shows the reprocessed spectra for the static and outflowing cases for different scattering angles (θ). This is mainly determined by the azimuthal angle of the point of last scattering, so this also determines the light-travel time lag. In the outflowing shell, the energies of the Fe-K line move toward the red-/blueshifted side due to Doppler shift when the photons are scattered on the far/near side of the shell, respectively. As a result of superposition of these different Fe-K energies, the integrated reprocessed spectra has broad line features (figure 5.3, right panels).

In the edge-on case, photons in the soft energy bands are absorbed in all θ values. In the mid-inclination case, soft photons are not absorbed when θ gets larger as the far side of the shell can be seen directly even when the central source is obscured. In the face-on case, there are few photons whose θ is larger than $3\pi/5$. When an incident photon is emitted in the x direction, $\vec{p} = (-1, 0, 0)$, and $\vec{q} = (\sqrt{29}/15, 0, 14/15)$, the maximum θ value is 111°.04, only slightly larger than $3\pi/5\,{\rm rad} = 108°$.

Figure 5.5 shows counts of reprocessed photons in each time- and energy-bin, which corresponds to figure 4.4. In both the edge-on and the mid-inclination cases, the energy-averaged responses have two peaks, the first from 0–4000 s ($\lesssim 1R/c$) from scattering on the near side of the shell with small scattering angles θ, and the second peak at $\sim$ 9000 s ($\simeq 2R/c$) from

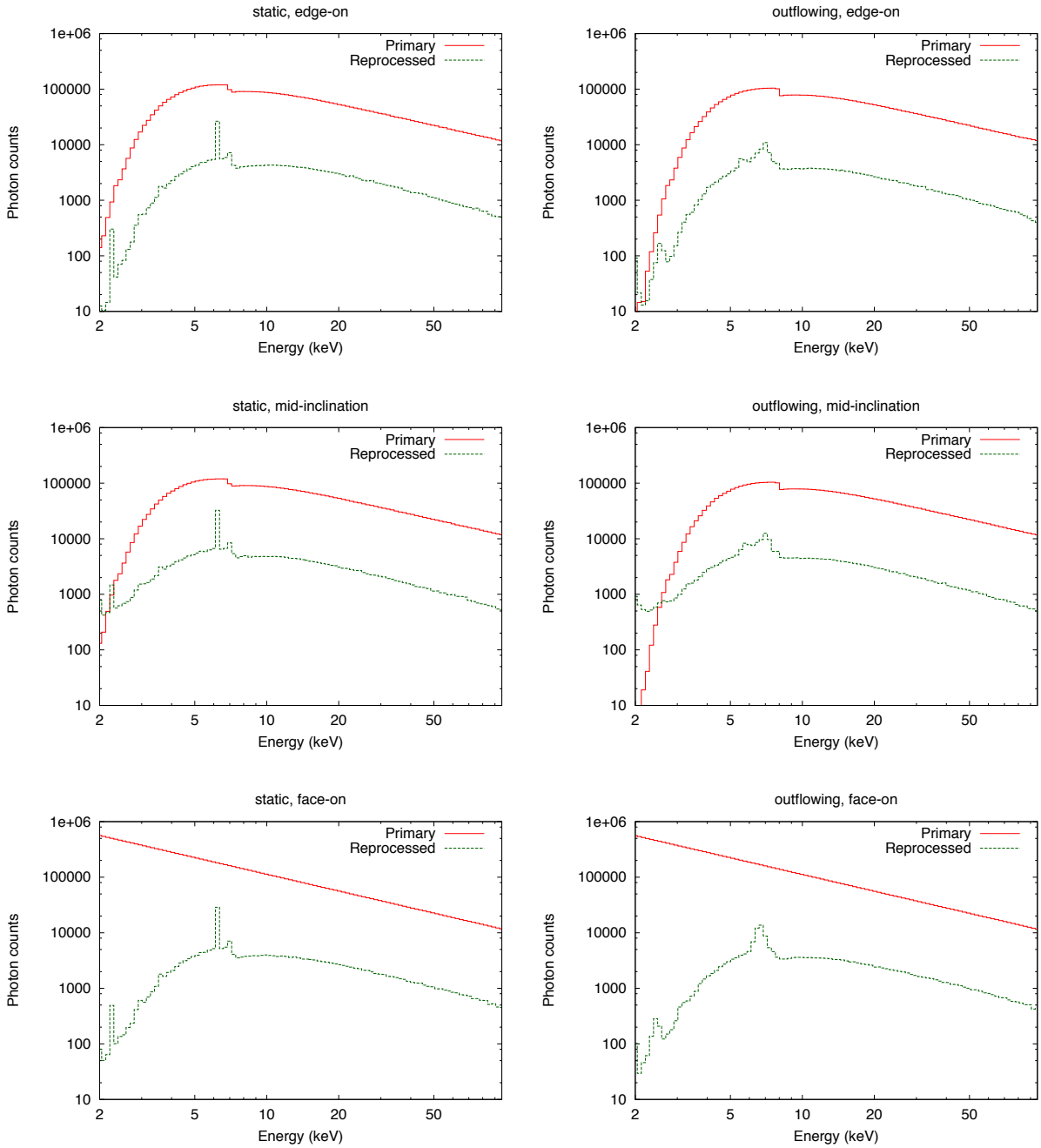

Figure 5.3: Energy spectra of the primary/reprocessed components with different inclinations for each of the static shell (left) and the outflowing shell (right). Each energy-bin-width is made logarithmically equal ($\Delta \log E\,(\mathrm{keV}) = 0.017$). Note that the reprocessed photons are dominant below ~ 3 keV in the outflowing mid-inclination case, which significantly affects the energy/frequency dependent lag features.

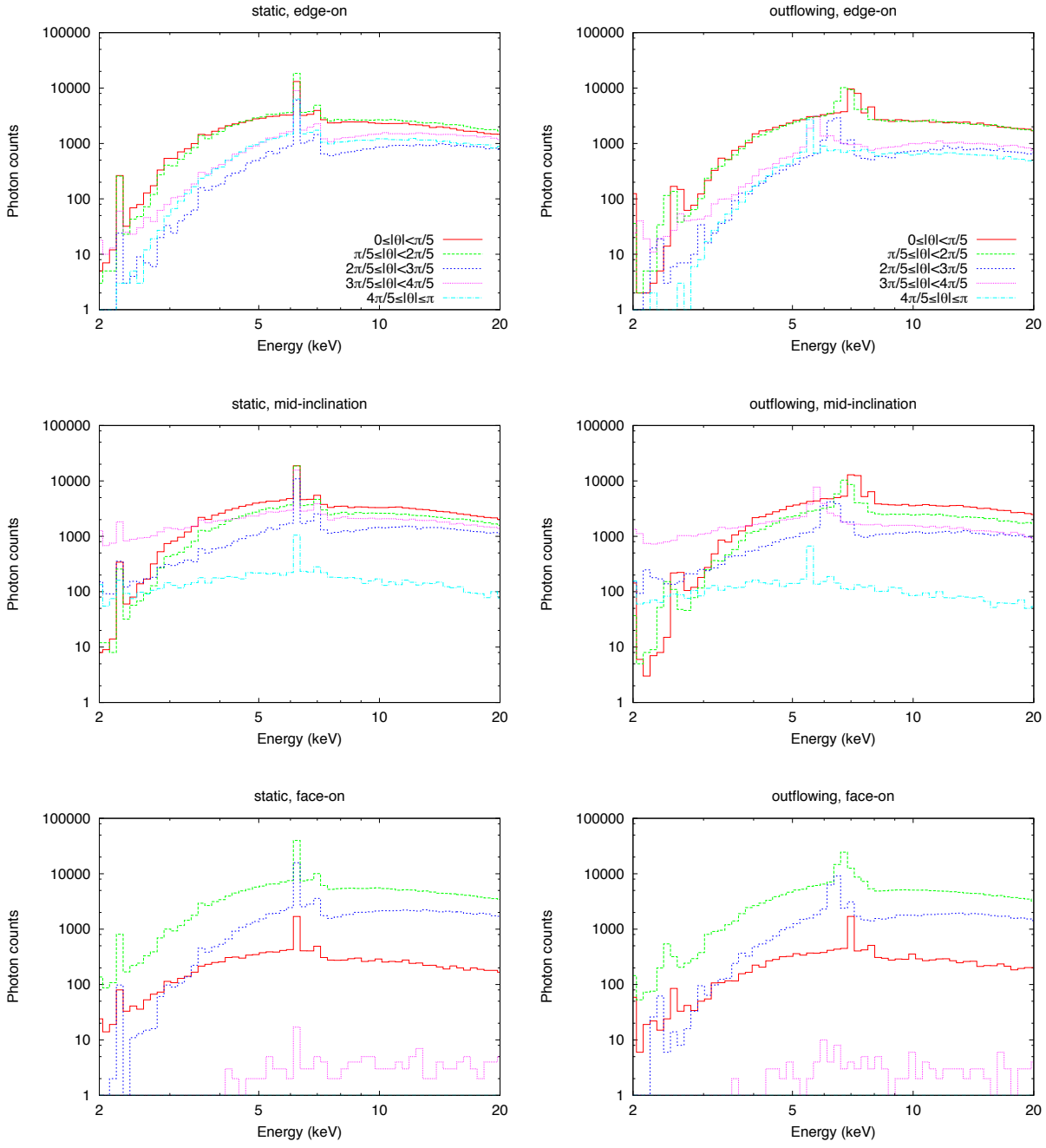

Figure 5.4: Energy spectra of the reprocessed components with different scattering angles (θ), for each of the static shell (left) and the outflowing shell (right). The scattering angles are shown in the top panels.

scattering on the far side of the shell with large θ. These two merge into a single peak for the face-on case. The blue vertical lines show the average delay time weighted by the number of photons including the primary ones without time delay. The number of reprocessed photons is much less than that of the primary photons, and thus the average delay time is much shorter than the light-travel time of the reprocessed photons (*dilution effect*). In the edge-on and mid-inclination cases, the average delay time is ∼200 s, corresponding to $4\,R_g/c$. This is shorter than the light-travel time from the source to the reflection shell by more than one order of magnitude. In the face-on case, the average delay time is even shorter, ∼50 s, which corresponds to R_g/c, because there are more primary photons and thus the dilution effect is more significant.

5.2.2.2 Lag-frequency plot

Equation (4.9) is again used to calculate lags. In this calculation, we set $t_{\rm bin} = 100$ s and $k_{\rm max} = 400$, so we consider lags between 0–40,000 s. Figure 5.6 shows the lag-frequency plots, comparing a soft band (3–4 keV) with a hard band (5–7 keV). In all the cases except for the outflowing mid-inclination case, *hard* lags are seen with an amplitude of $\lesssim 150$ s, which is much shorter than the light-travel time to the shell (5000 s) and comparable to the weighted average delay time (figure 5.5). In the outflowing mid-inclination case, *soft* lags with an amplitude of ~ 100 s are seen because the reference 3–4 keV band has a higher fraction of reprocessed flux than the others, so the "continuum" band is actually more dominated by lagged photons than the other cases. The lags are attenuated in all the cases at the frequency range of $> 2\times10^{-4}$ Hz, because the fast variations are smeared by the light-travel time across the shell.

In order to analytically evaluate frequency dependence of the lags, we rewrite equation (4.6) as

$$\begin{aligned} s(t) &= P_s g(t) + R_s \int dt' \psi_s(t') g(t-t') \\ h(t) &= P_h g(t) + R_h \int dt' \psi_h(t') g(t-t'), \end{aligned} \tag{5.1}$$

where R_s and R_h show the reprocess components in the soft- and hard-band, and ψ_s and ψ_h are normalised response functions ($\int dt\,\psi_s(t) = \int dt\,\psi_h(t) = 1$). Under the assumption that $\psi_s(t) = \psi_h(t) = \delta(t-\Delta t)$, i.e., the response is a delta-function, the lag is written as

$$\begin{aligned} \tau(f) &= \frac{1}{2\pi f} \arg\left[\left(P_s + R_s \exp[-2\pi i \Delta\tau f]\right)\left(P_h + R_h \exp[2\pi i \Delta\tau f]\right)\right] \\ &= \frac{1}{2\pi f} \arctan\left(\frac{(P_s R_h - R_s P_h)\sin(2\pi\Delta\tau f)}{P_s P_h + R_s R_h + (P_s R_h + R_s P_h)\cos(2\pi\Delta\tau f)}\right). \end{aligned} \tag{5.2}$$

In the $f \to 0$ limit,

$$\tau(f\to 0) = \frac{P_s R_h - R_s P_h}{(P_s + R_s)(P_h + R_h)}\Delta\tau = {\rm DF}\,\Delta\tau, \tag{5.3}$$

where the *dilution factor* DF can be calculated directly from the primary and reprocessed emission in each band. For example, when we use the parameters of the static edge-on case,

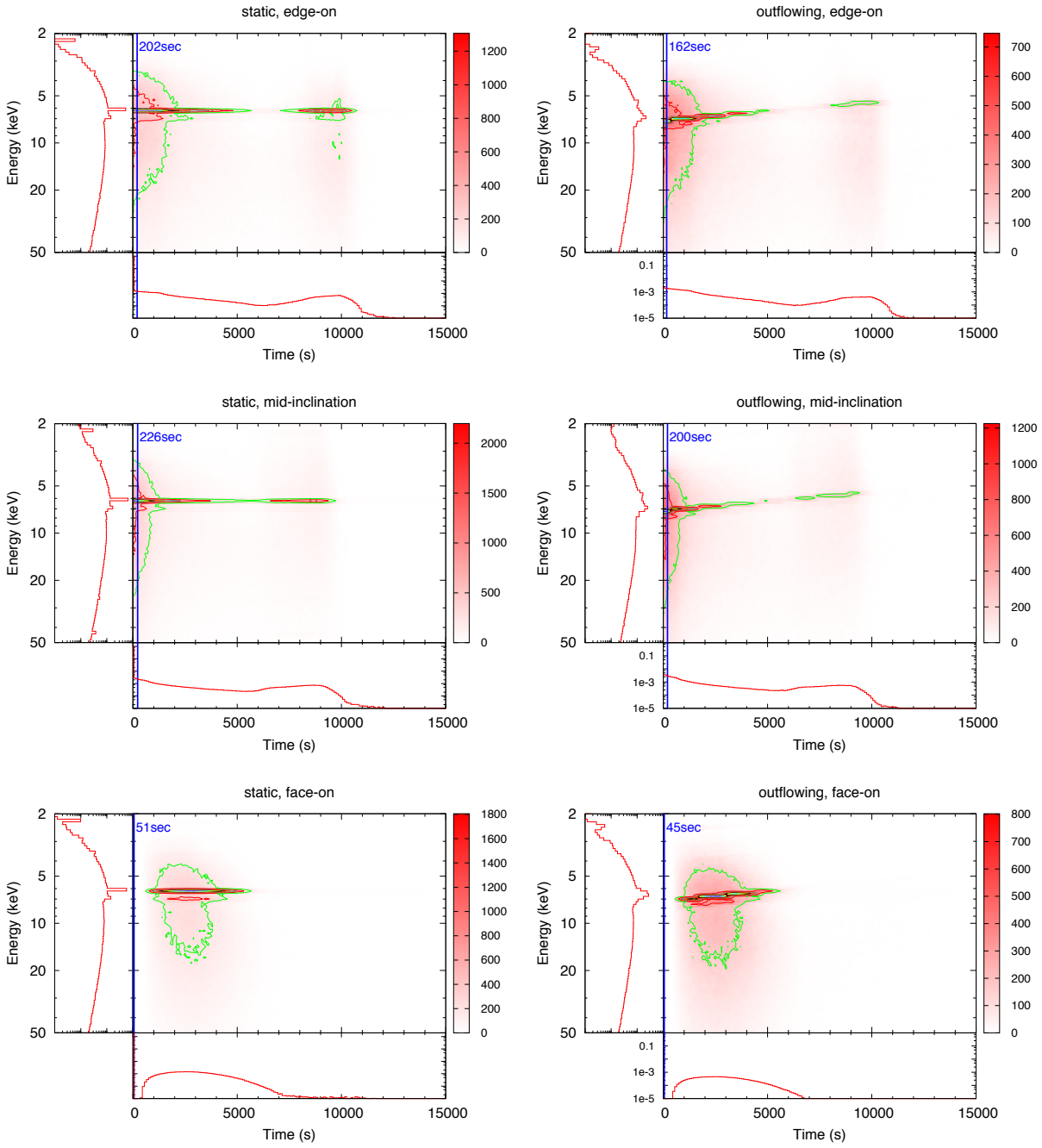

Figure 5.5: Main panels: Counts of reprocessed photons in each time- and energy-bin with contour plots for a distant shell at $R = 10^2\, R_g$ around the $M_{\rm BH} = 10^7\, M_\odot$ black hole ($R/c = 5000$ s), when the X-ray source emits at once with a delta-function of time. The blue vertical lines show the average delay time weighted by the number of photons, including the primary ones. Contour plots show one-tenths of the peak count. Left-hand panels: the time-averaged responses, which are identical to the reprocessed spectra. Bottom panels: the energy-averaged responses, showing response of the entire photons as a function of time. The vertical axis is normalised by the photon counts of the primary component, that is, the component without any lags.

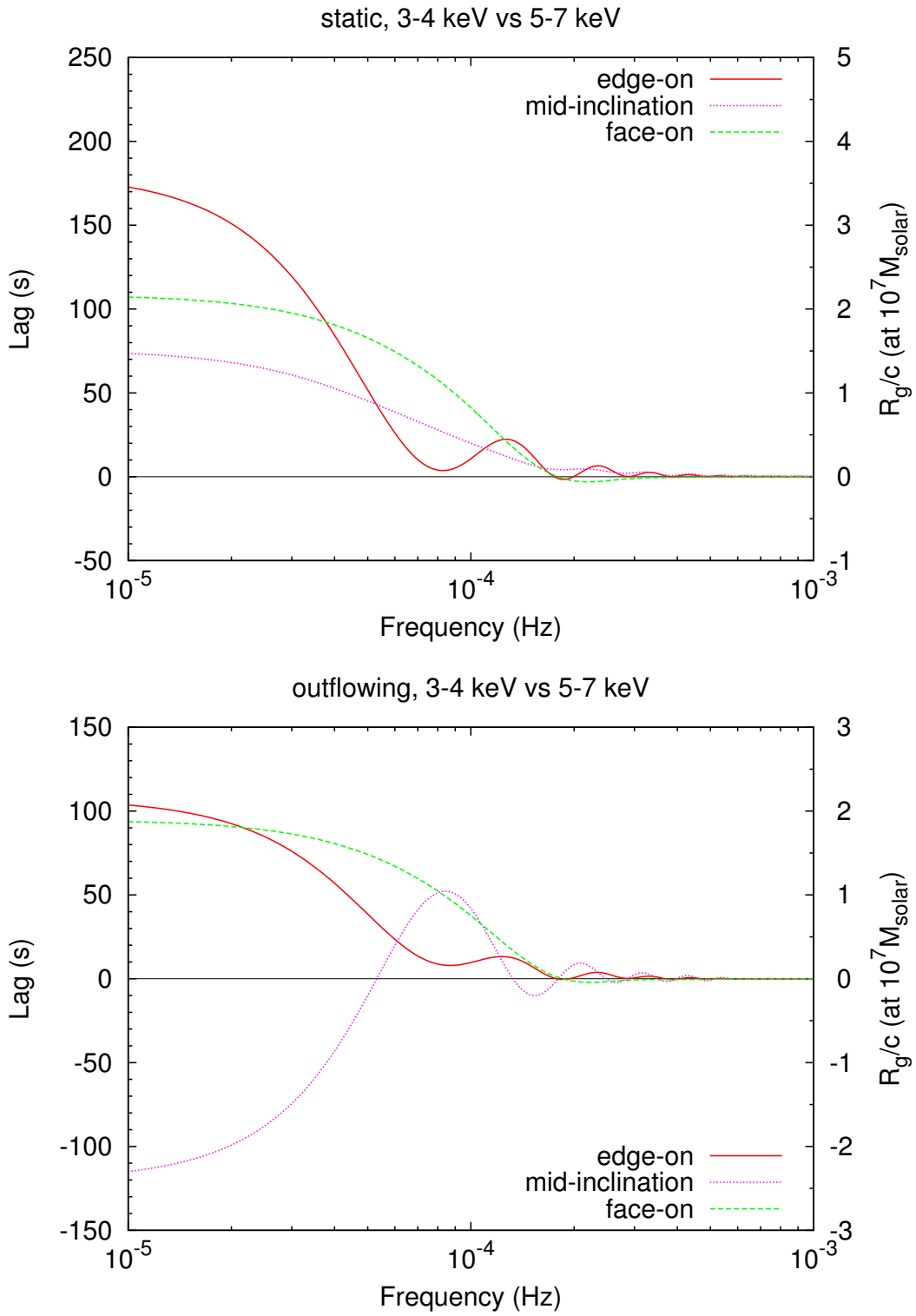

Figure 5.6: Lag-frequency plots when comparing 3-4 keV with 5-7 keV, derived from the Monte-Carlo simulation. Positive lags mean the hard lags, and vice versa.

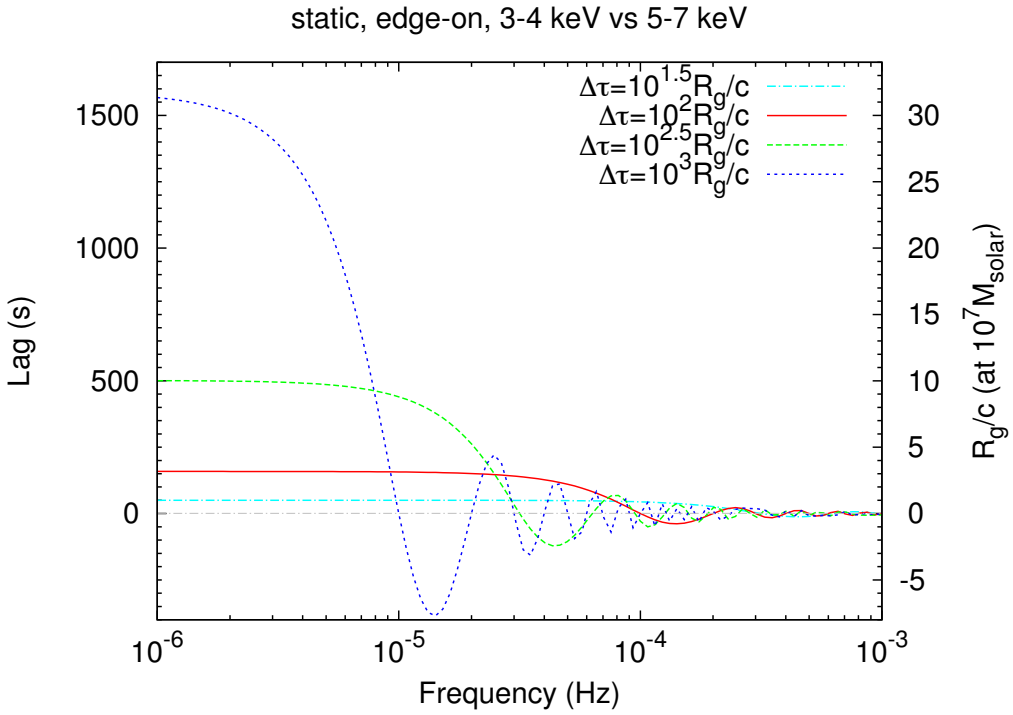

Figure 5.7: Lag-frequency plots with deferent light-travel times. The response is assumed to be a delta-function. Parameters of the static edge-on case are used. The time delay $\Delta\tau$ gets shorter from top to bottom at 10^{-6} Hz.

then the soft band (3–4 keV) counts in the primary and reprocessed flux give $P_s = 34.1$ and $R_s = 1$, while the hard band (5–7 keV) has $P_h = 111.6$ and $R_h = 7.2$ (see figure 5.3), so DF $= 3.17 \times 10^{-2}$. This predicts that DF reduces the observed lags by more than one order of magnitude. The mean intrinsic lag is of order $\Delta\tau \sim R/c = 5000$ s, so this predicts an observed lag at low frequencies of 158 s, which is very close to the ~ 170 s seen in the right panel of figure 5.6 for the edge-on case (red-solid line) as $f \to 0$. The difference comes from the mean intrinsic lag time being different from R/c by a factor (see the energy-compressed response in figure 5.5).

Equations (5.2) and (5.3) explicitly show that the measured lag amplitudes are not the immediate diagnostic of the size scale of the system; indeed they depend on the relative contribution of primary and reprocessed emission in each band. Instead, the size scale can be constrained by frequencies where the lag is attenuated. Figure 5.7 illustrates the light-travel time dependence of the lag frequencies. The lags oscillate around zero in the high frequency, and almost disappear on c/R. For example, when the light-travel time is $10^2\, R_g/c = 5000$ s, the lag is fully attenuated at 2×10^{-4} Hz $= c/R$ Hz. The frequencies where lag is attenuated decrease as the size scale gets larger, as expected.

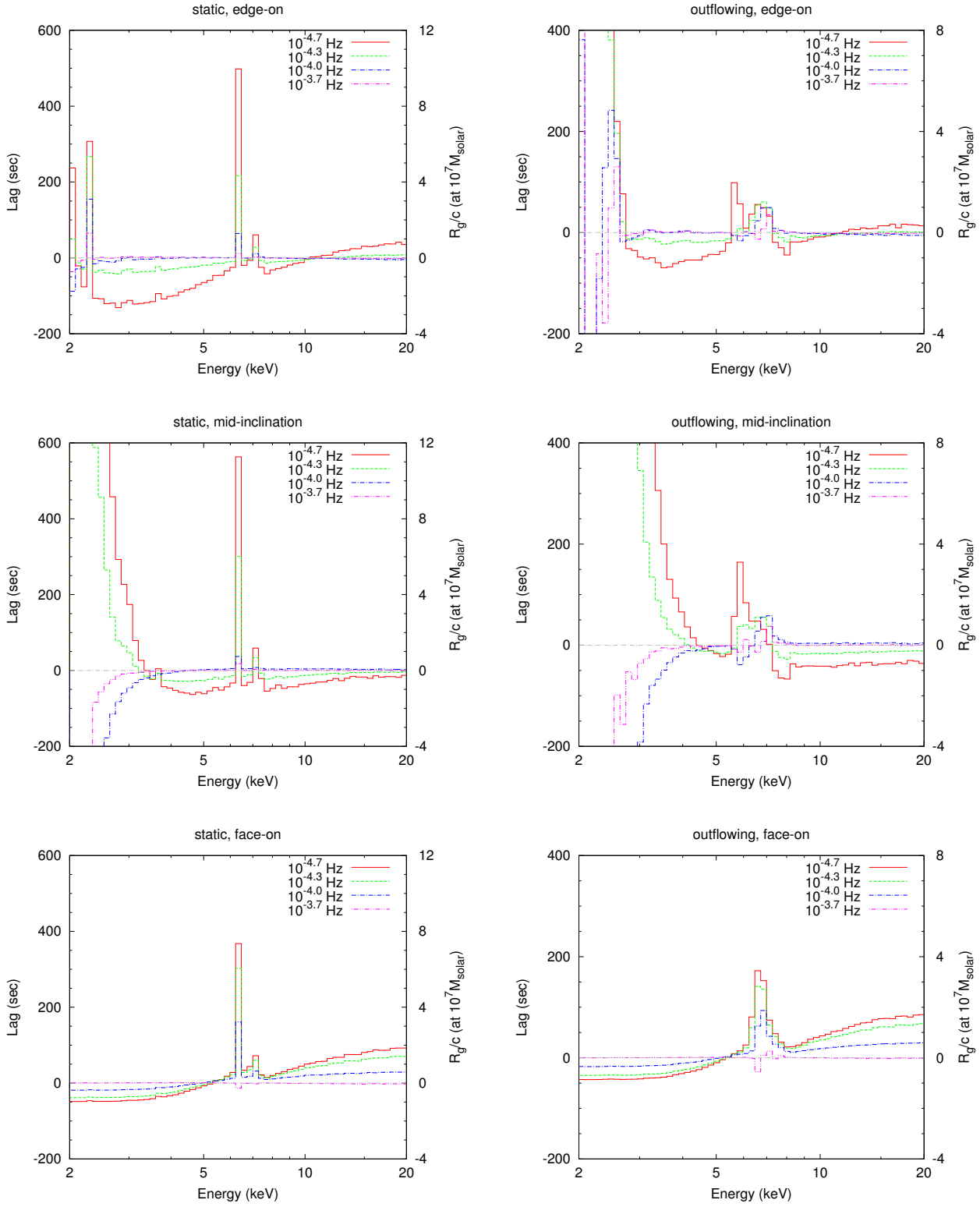

Figure 5.8: Lag-energy plots at various frequencies derived from the Monte-Carlo simulation.

5.2.2.3 Lag-energy plot

Figure 5.8 shows the lag-energy plots derived over four different frequencies to illustrate how this changes as a function of variability timescale. We use 2-20 keV as the reference band. The Fe-K lag amplitude, as well as the amplitudes of all the other lag features, become smaller as the frequency increases. This is because fast variations are smeared out by the light-travel time across the shell. Therefore, lagged signals are hardly seen on frequencies above 2×10^{-4} Hz. For lower frequencies, narrow Fe-K lines are seen from the static shell, while the lags are seen across a much broader 5–7 keV range in the outflowing shell. This is expected from the Doppler shifts determining the line broadening in the line-of-sight. Since the shift correlates with θ, which correlates with the lag time, the centroid energy of the broad Fe-K line in the lag-energy plot shifts depending on the variability timescale. Long variability times are required to see the longest lags, which come from material on the far side of the shell, where the line is redshifted. On the other hand, material on the near side of the shell, where the line is blueshifted, can respond to the shorter variability timescales. Thus the lag-energy plots for the outflowing shell have the line energy shifting from red to blue as the variability timescale decreases, correlated with decreasing line amplitude as the shell less contributes at higher frequencies.

Here, we again consider the $f \to 0$ limit. The energy-dependent dilution factor $\mathrm{DF}(E)$ can be calculated as

$$\mathrm{DF}(E) = \frac{P_{\mathrm{tot}} R(E) - R_{\mathrm{tot}} P(E)}{(P_{\mathrm{tot}} + R_{\mathrm{tot}})(P(E) + R(E))}, \tag{5.4}$$

where $P(E)$ and $R(E)$ are the primary and reprocessed components in the energy bin of interest, and P_{tot} and R_{tot} are those in the total energy band, like equation (5.2). Under the assumption that $R_{\mathrm{tot}}/P_{\mathrm{tot}} \ll 1$ and $R(E)/P(E) \ll 1$, equation (5.4) is approximated to be

$$\mathrm{DF}_{\mathrm{approx}}(E) = \frac{R(E)}{P(E)} - \frac{R_{\mathrm{tot}}}{P_{\mathrm{tot}}}. \tag{5.5}$$

In other words, $\mathrm{DF}_{\mathrm{approx}}$ is calculated as difference between relative flux of the reprocessed component to the primary component in the energy bin of interest and that in the total energy band. These equations work very well to describe the lag-energy spectrum. Figure 5.9 shows comparison of the lag-energy plot in the low-frequency range with $\mathrm{DF}(E)$. We can see that $\tau_{f\to 0}(E) \simeq \mathrm{DF}(E)\Delta\tau \simeq \mathrm{DF}_{\mathrm{approx}}(E)\Delta\tau$ with subtle differences.

Consequently, we have found that the characteristic lag features (frequencies, amplitudes, and broad profiles) are likely to be explained by the outflowing and partial-shell-like clouds located within $\sim 100\ R_g$. Reverberation lags are seen up to $\lesssim c/R$ Hz, so that scattering materials with $R \sim 100\ R_g$ are required. The lag amplitude as short as several R_g are explained by the dilution effect, which can dilute the time delay of the scattered component by two orders of magnitude. In addition, when the scattering cloud have an outflow velocity, photons scattered on the near side gets blueshifted, whereas those on the far side gets redshifted. Therefore, the time lag is observed in a wide energy range.

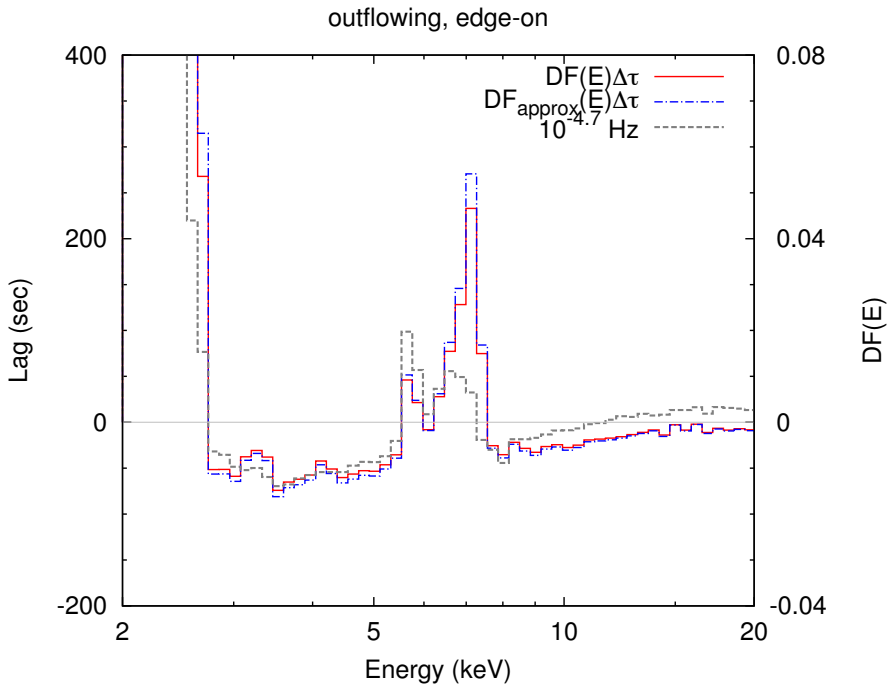

Figure 5.9: Plots of DF(E)$\Delta\tau$ (red-solid, shown by equation 5.4), DF$_{\rm approx}$(E)$\Delta\tau$ (blue-dot-dashed, shown by equation 5.5), and the lag-energy plot in the outflowing edge-on case at $10^{-4.7}$ Hz (grey-dashed), which is same as the one in the right upper panel of figure 5.8). The right axis shows the DF(E) values.

5.3 Reflection by ionised wind-like clouds

We have shown in the previous subsection that the outflowing and partial-shell-like clouds located within $\sim$ 100 R_g are required to reproduce lag features. The disc wind is the most plausible material, since it is accelerated by the radiation force produced by UV/X-ray illumination and commonly observed in accretion objects such as AGNs and BH binaries (see §2.2.4). The launching point of the disc wind is about several tens of R_g (e.g., Nomura et al. 2016), which is consistent with the required geometries to explain the observed lag features. The disc wind is ionised, being close to the illuminating source, as indicated by blueshifted absorption lines of the highly-ionised iron ions, such as the UFO lines (figure 2.5). So far, we have considered non-ionised clouds, which is not realistic. Thus, in this section, we consider a more realistic disc-wind geometry, that is, ionised and biconical outflowing clouds.

5.3.1 Setting

The disc-wind geometry is not fully understood. Although theoretical studies proposed several different geometries (like figure 2.6), they are too complicated to handle. Therefore we assume a simplified geometry to calculated reverberation lags due to the wind. We adopt a "biconical wind" geometry, which was used to study radiative transfer in the accretion disc wind (e.g., Shlosman & Vitello 1993; Knigge et al. 1995; Sim et al. 2008, 2010). Hagino et al. (2015, 2016) performed Monte-Carlo calculation in this geometry to explain UFO

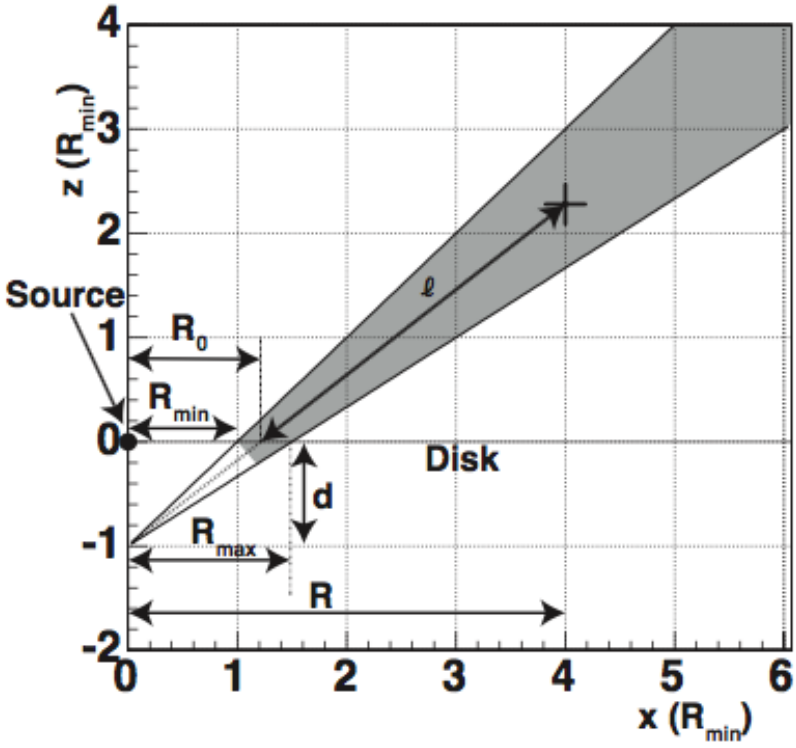

Figure 5.10: Geometry for the wind model (Hagino et al. 2015). The shaded region is filled with outflowing materials. The wind is rotationally symmetrical around z-axis.

absorption lines in the energy spectra using MONACO. The assumed wind has a small solid angle ($\Omega/4\pi = 0.15$), launched at $R_{\rm min} = 2(v_{\rm wind}/c)^{-2} = 50\,R_g$ when $v_{\rm wind} = 0.2c$, where the wind velocity exceeds the escape velocity. This geometry includes radial dependence of density and ionisation degree.

Details of the model and calculation scheme are fully described in Hagino et al. (2015, 2016). The focal point of the biconical wind is located at a distance d offset from the BH. This geometry is mainly characterised by three parameters; the solid angle Ω, the minimum radius $R_{\rm min}$, and the inner angle $\theta_{\rm min}$. The radial velocity follows an extension of the CAK velocity law (Castor et al. 1975), i.e.,

$$v_r(l) = v_0 + (v_\infty - v_0)\left(1 - \frac{R_{\rm min}}{R_{\rm min} + l}\right)^\beta, \tag{5.6}$$

where $v_r(l)$ is a radial velocity of the wind along a streamline of length l from its launch point. This is parametrised by the initial velocity v_0, the terminal velocity v_∞, and the acceleration index β. The rotational velocity and the density are determined by conservation of the angular momentum and the mass, respectively. The bicone is split into 100 (radial)×64 (azimuthal)×2 (polar) cells, and the ion populations are calculated in each radial shell by using XSTAR (figure 5.11). The ionisation structure is calculated sequentially from the inner to the outer shells. Two types of the photons are considered; those directly come from the source and illuminating the shell, and those transmitted through the inner shells and being incident on the inner boundary. After each run we can get the output spectrum, which in

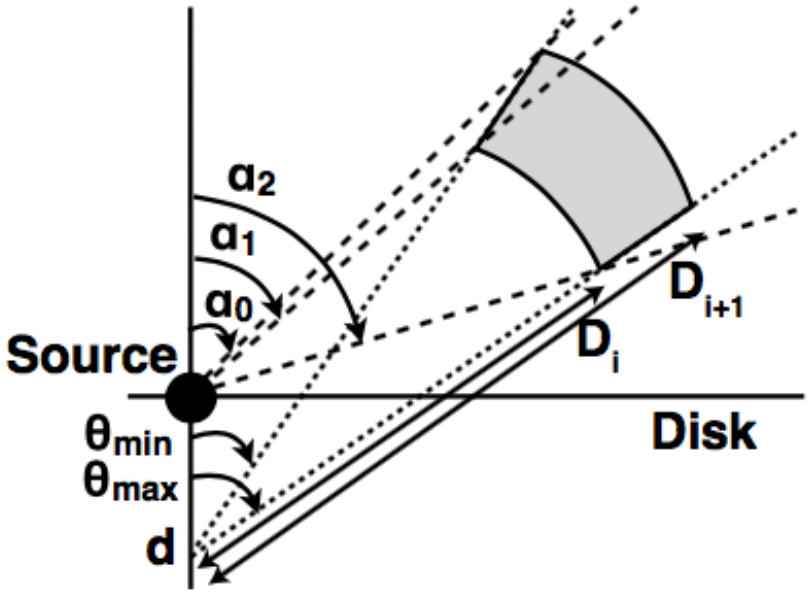

Figure 5.11: Geometry used for ionisation calculation (Hagino et al. 2015). In each shell between D_i and D_{i+1}, there are two types of incident photons; those directly coming from the source and those transmitted and emitted outward through the inner shell. Their fractions are parameterised by α_0, α_1, and α_2, which are expressed with D_i, D_{i+1}, $\theta_{\rm min}$, $\theta_{\rm max}$, and d.

turn becomes an incident spectrum for the next shell. We assume that the central source emits a power-law spectrum with photon index Γ and ionising luminosity $L_{\rm X}$. The resulting H- and He-like ion densities of each element are put into MONACO. The typical electron temperature and ionisation degree are calculated to be $\sim 10^5$ K and $\log \xi \sim 4-5$, so the wind consists of only highly-ionised material. We consider transitions of only H- and He-like ions of Fe and Ni, which is possible by the current MONACO code.

The wind mass-loss rate $\dot{M}_{\rm wind}$ is written as

$$\dot{M}_{\rm wind} = 1.23 m_p n(r) v(r) 4\pi D^2 (\Omega/4\pi), \tag{5.7}$$

where m_p is the proton mass, $n(r)$ is a number density, D is distance from the focal point, and Ω is a solid angle of the wind. This geometry is simply scaled by the BH mass; under the assumption that $L_{\rm X} \propto \dot{M}_{\rm wind} \propto M_{\rm BH}$, the ionisation degree and the column density are not dependent on the BH mass.

We use the same parameters as Hagino et al. (2016), i.e., $R_{\rm min} = d = 50\,R_g$, $\beta = 1$, $v_0 = 10,000$ km s^{-1} (same as a turbulent velocity), $v_\infty = 0.2c$, $\dot{M}_{\rm Edd}/M_{\rm BH} = 0.2$, $\Gamma = 2.6$, $L_{\rm X}/L_{\rm Edd} = 10^{-3}$, and the wind fills a bicone between $\theta_{\rm min} = 45^\circ$ to $\theta_{\rm max} = 56.^\circ 3$ ($\Omega/4\pi = 0.15$). We assume $M_{\rm BH} = 2 \times 10^6\,M_\odot$.

The wind velocity at the vicinity of the launch point is relatively slow, so the region within $100\,R_g$ has low ξ and high $N_{\rm H}$ (figure 5.12). In this region, the H-like iron ions are dominant (see figure 2.3), so the emission line due to resonance scattering is effectively produced. Figure 5.13 shows locations of the photon scattering in this simulation. The blank spot near the launching point is where the cloud is optically-thick. The density of the scattered

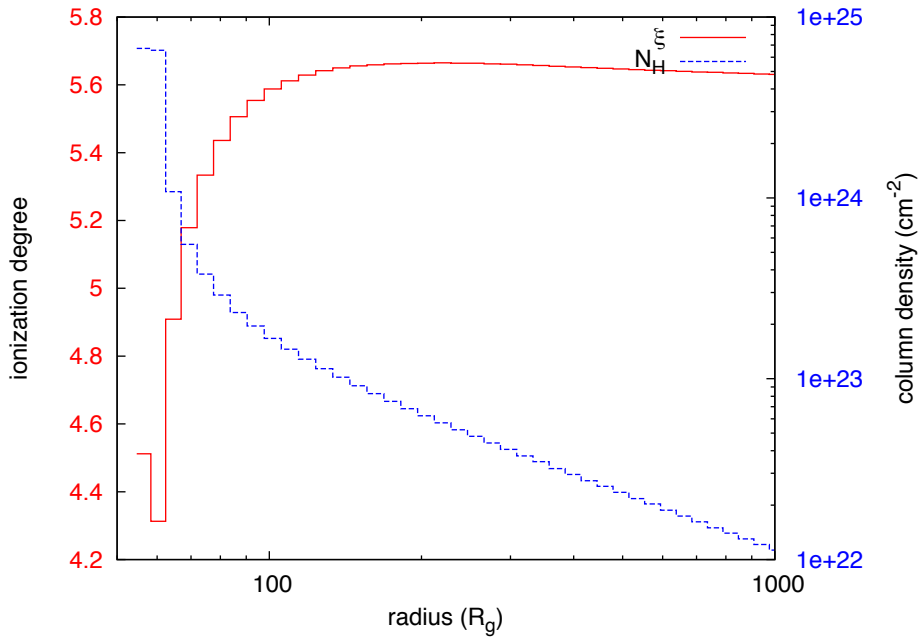

Figure 5.12: The ionization degree (red solid) and column density (blue dashed) as a function of distance from the focal point of wind. Each bin corresponds to a radial shell in XSTAR calculation.

photons becomes more sparse as the radius gets larger, indicating that the scattering mainly occurs in the inner region.

The number density n around the launch point (i.e., in the thickest region) is calculated to be $\sim 10^{12}$ cm^{-3} for the assumed $M_{\rm BH}$. This density is consistent with the hydrodynamical simulations (e.g., Hashizume et al. 2015; Nomura et al. 2016). Timescale of the photoionisation equilibrium is formulated by Krolik & Kriss (1995) and Nicastro et al. (1999) as

$$t_{\rm eq}^{i,i+1} \simeq \left\{\alpha_{\rm rec}(X^i,T_e)_{\rm eq} n_e\right\}^{-1} \left[\left\{\frac{\alpha_{\rm rec}(X^{i-1},T_e)}{\alpha_{\rm rec}(X^i,T_e)}\right\}_{\rm eq} + \left(\frac{n_{X^{i+1}}}{n_{X^i}}\right)_{\rm eq}\right]^{-1}, \tag{5.8}$$

where "eq" means the equilibrium quantities, $\alpha_{\rm rec}$ is the radiative recombination coefficient (in cm^3 s^{-1}), X^i is i-th ion, T_e is an electron temperature ($\sim 10^5$ K), and n_{X^i} is the number density of i-th ion. With the $\alpha_{\rm rec}$ values in Shull & van Steenberg (1982) and our XSTAR results, $t_{\rm eq}^{25,26}$ is calculated to be $\sim 10^{-4}$ s, which indicates that timescales of the photoionisation equilibrium are negligible for lag calculations.

5.3.2 Products

Figure 5.14 shows the energy spectra, where we calculate for 25 patterns of inclination angles, $\cos i = 0/25 - 1/25, 1/25 - 2/25, \ldots, 24/25 - 25/25$. The primary components have blueshifted absorption lines, whose depth and line profiles are dependent on different inclination angles. Most ions are highly ionised and Thomson scattering is dominant in all the energy band, resulting in strong reprocessed continua. The H-like iron ions resonantly scatter the incident photons and make the Fe-K emission line, broadened by the Doppler

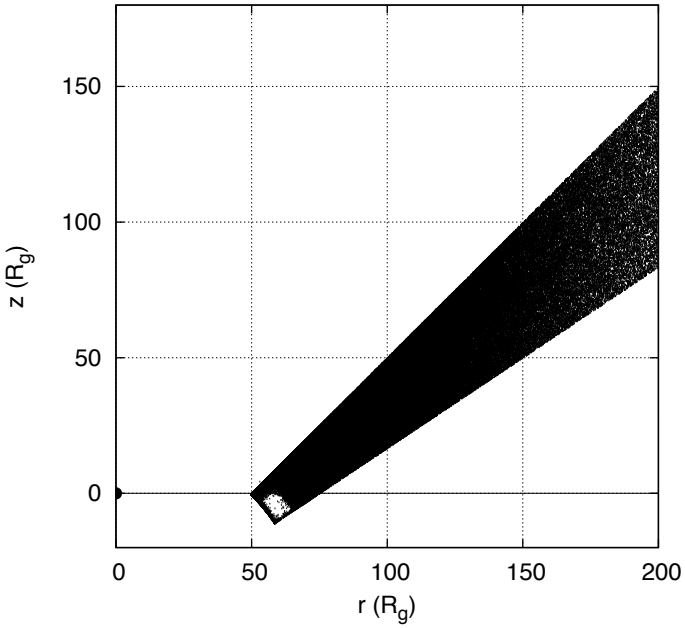

Figure 5.13: Locations of the photon scattering. The number of photons shown here is reduced for the sake of visibility.

shift. Both the primary and reprocessed component have blueshifted absorption lines, but that in the primary component is deeper than the one in the reprocessed one. The absorption lines are not seen for the low-inclination case, because no clouds exist in the line-of-sight. These features are consistent with Hagino et al. (2015, 2016).

In the lag-frequency plot (figure 5.15), the hard lag is seen for lower frequencies than $\sim 2 \times 10^{-3}$ Hz ($= c/50\,R_g$), as expected from figure 5.13. We have identified two characteristic components in the lag-energy plots (figure 5.16); the broad components in the 5–8 keV, which exist in all the cases, and the narrow ones, which are only seen in the high-inclination cases when the absorption lines are deep. The broad feature is produced due to the strong reprocessed component, whereas the narrow one is due to the absorption line in the primary spectra. In other words, the former reflects the wind clouds out of the line-of-sight that scatter X-ray photons, whereas the latter reflects those in the line-of-sight that absorb photons.

5.3.3 Comparison with observations

Here let us compare the simulation results with observations. We select three targets; Ark 564, 1H 0707–495, IRAS 13224–3809. These objects are known to show large X-ray variability and typical reverberation lags, and observed with a long exposure time with the total exposure time longer than 400 ks by *XMM-Newton*. We use the EPIC-pn data, which has the largest effective area in XMM around the Fe-K band. Periods with high background flares are ignored. We compute lags in each observation ID, and calculate their averages.

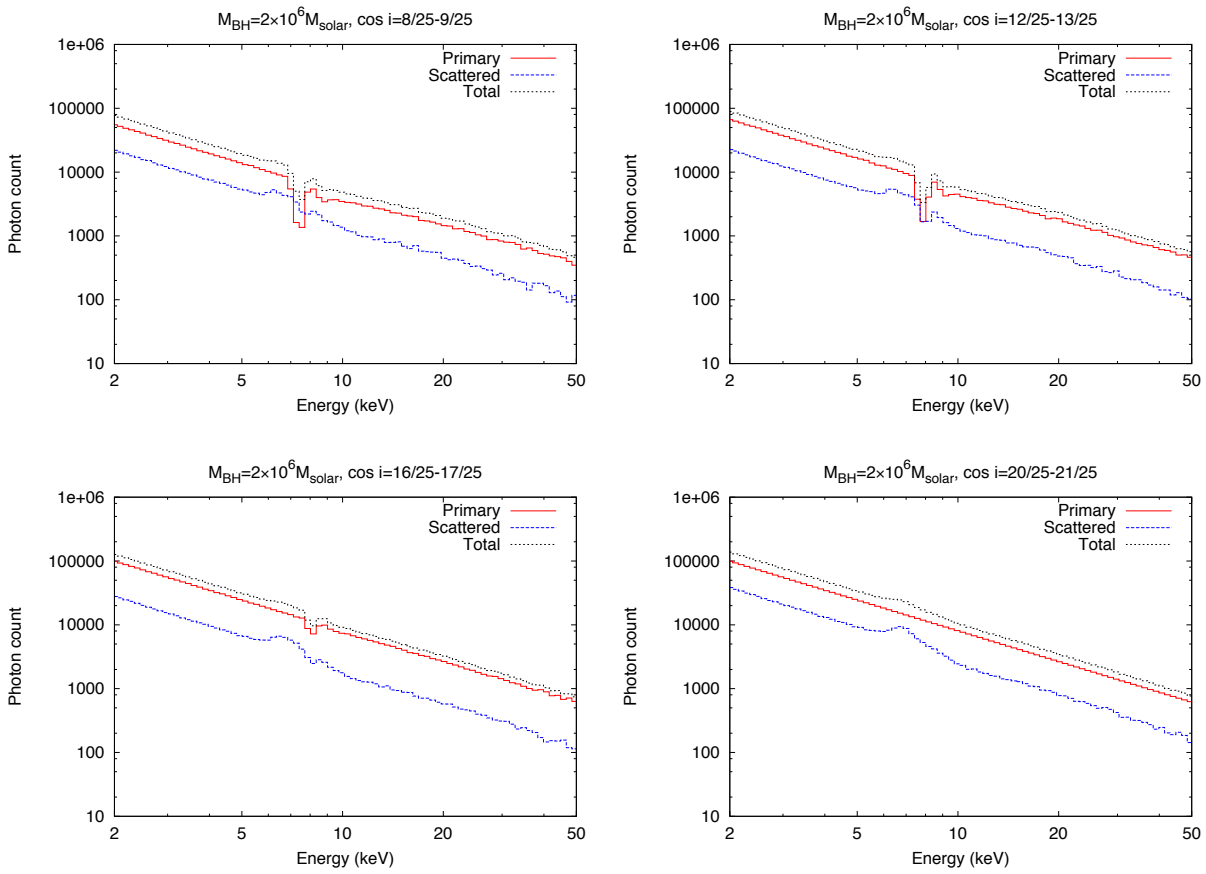

Figure 5.14: Energy spectra of primary (red solid), scattered (blue dashed), and total (black dotted) components in the wind model. Four representative inclination angles are shown, while calculation is made for 25 different angles.

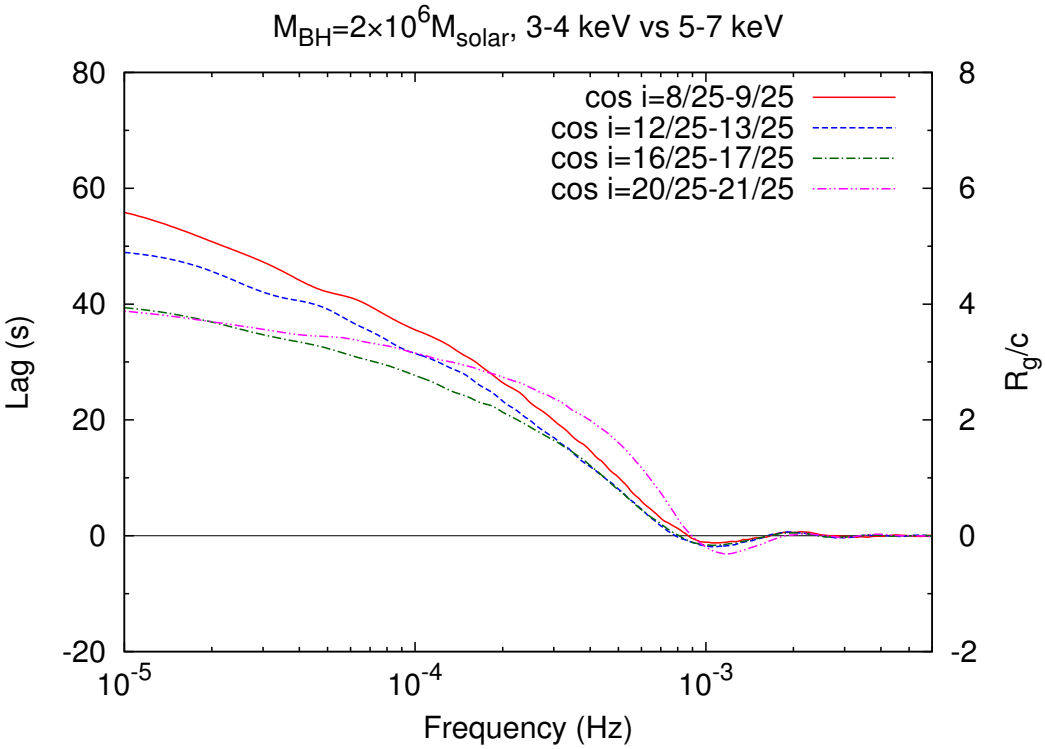

Figure 5.15: Lag-frequency plots in the wind model.

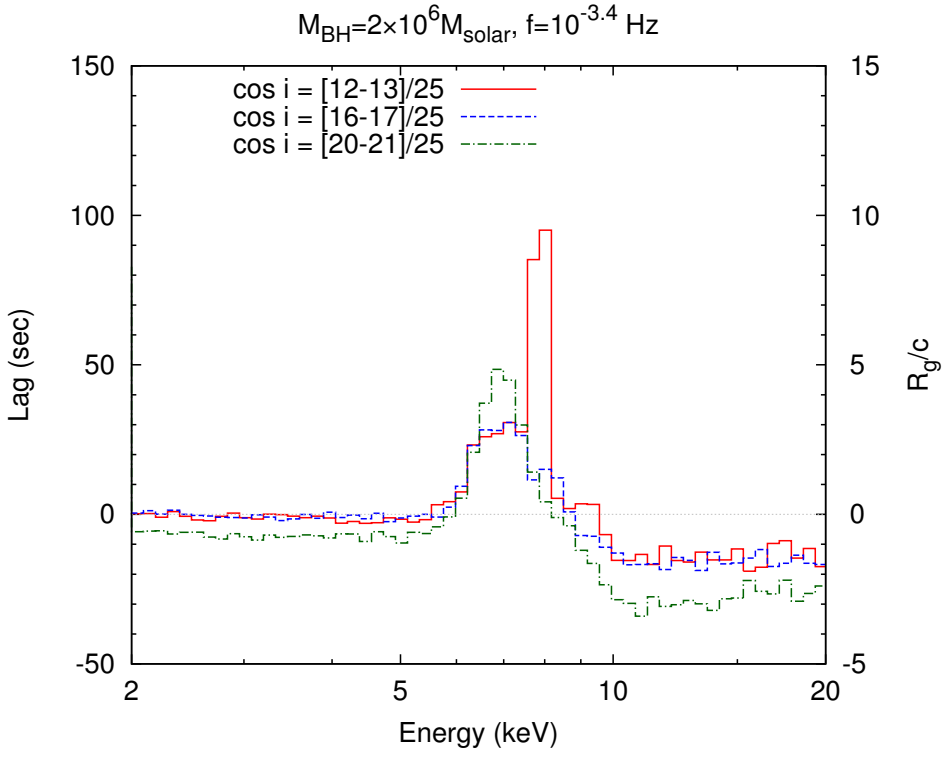

Figure 5.16: Lag-energy plots in the wind model for different inclination angles. The assumed $M_{\rm BH}$ and frequency are $2 \times 10^6\,M_\odot$ and $10^{-3.4}$ Hz, respectively.

Constraining the upper bound of the frequencies of the reverberation lags is important to know location of the scattering materials; the lags disappear at the frequency of $\sim c/R$ Hz when the scattering material is located at R (see §5.2.2.2). In order to constrain the frequencies where the lags disappear, we calculated the lag-energy plots with different frequency ranges with a high/low ratio of $10^{-0.4}$ Hz, changing the lower frequencies with a step of $10^{0.1}$ Hz, and examined presence of Fe-K lags. For example in Ark 564, we calculated lag-energy plots in the frequency ranges of $10^{-[4.0-3.6]}$ Hz, $10^{-[3.9-3.5]}$ Hz, ..., $10^{-[3.0-2.6]}$ Hz, and found that $10^{-[3.4-3.0]}$ Hz is the highest frequency range where the Fe-K lags are seen. Figure 5.17 shows the lag-energy plots in the highest frequency ranges. We have noticed that these plots and their frequency ranges are very similar to each other; they have the broad Fe-K lag features with amplitudes of $\lesssim 100$ s at the upper frequencies of $\sim 10^{-3.0}$ Hz, which corresponds to 1000 s. Therefore, we speculate that the three targets have similar wind geometries, especially similar $R_{\rm min}$ and Ω. Next, we try to compare them normalising the frequency range, considering difference of the BH masses. The frequency ranges of 1H 0707–495 and IRAS 13224–3809 are $10^{-0.2}$ and $10^{-0.1}$ times that of Ark 564 (see legends of figure 5.17). If these three targets share the same geometry, the BH masses of 1H 0707–495 and IRAS 13224–3809 are considered to be $1.3 \times 10^6\,M_\odot$ and $1.6 \times 10^6\,M_\odot$, when that of Ark 564 is $2 \times 10^6\,M_\odot$.[2] Figure 5.18 shows the normalised lag-energy plots; the vertical axis is scaled by the gravitational radius and all plots have the same normalised frequency range; from $c/250\,R_g$ to $c/100\,R_g$ ($10^{-[3.4-3.0]}$ Hz for $M_{\rm BH} = 2 \times 10^6\,M_\odot$). The profiles are very similar to each other and successfully reproduced by the model plot (red-solid line). This figure indicates that the observed lag profiles can be fully explained by the disc wind model.

5.4 Summary of this chapter

We calculate X-ray reverberation lags produced by scattering clouds around AGN via Monte-Carlo simulation. First, the scattering material is assumed to be such a neutral, part-spherical thin shell at $100\,R_g$ with the black-hole mass of $10^7\,M_\odot$ that is either static or outflowing at $0.14\,c$. We compiled results for each simulation over three different inclination angles. As a result, we found short-time ($\lesssim 150$ s) hard lags between a continuum (3–4 keV) and Fe-K band (5–7 keV) in the frequency range of $\lesssim 10^{-4}$ Hz, which is much shorter than the light-travel time (5000 s) and consistent with observations. The short lag amplitude compared to the light-travel time is explained by the dilution effect, where majority of the photons in the Fe-K energy band are the primary photons without time-delay, whereas the time-delayed reprocessed photons have a minor contribution. Hence we suggest that the observed X-ray reverberation lag features can be produced by the outflowing matter at $\lesssim 100\,R_g$.

Next, we calculated lags due to a more realistic biconical wind, which is adopted in Hagino et al. (2015, 2016), and compared the simulation results with observations of Ark 564, 1H

[2] The $M_{\rm BH}$ values of 1H 0707–495 and IRAS 13224–3809 in literature are $2 \times 10^6\,M_\odot$ and $6 \times 10^6\,M_\odot$ with a large uncertainty (Ponti et al. 2012). The difference is within a factor of 4, which we consider is acceptable.

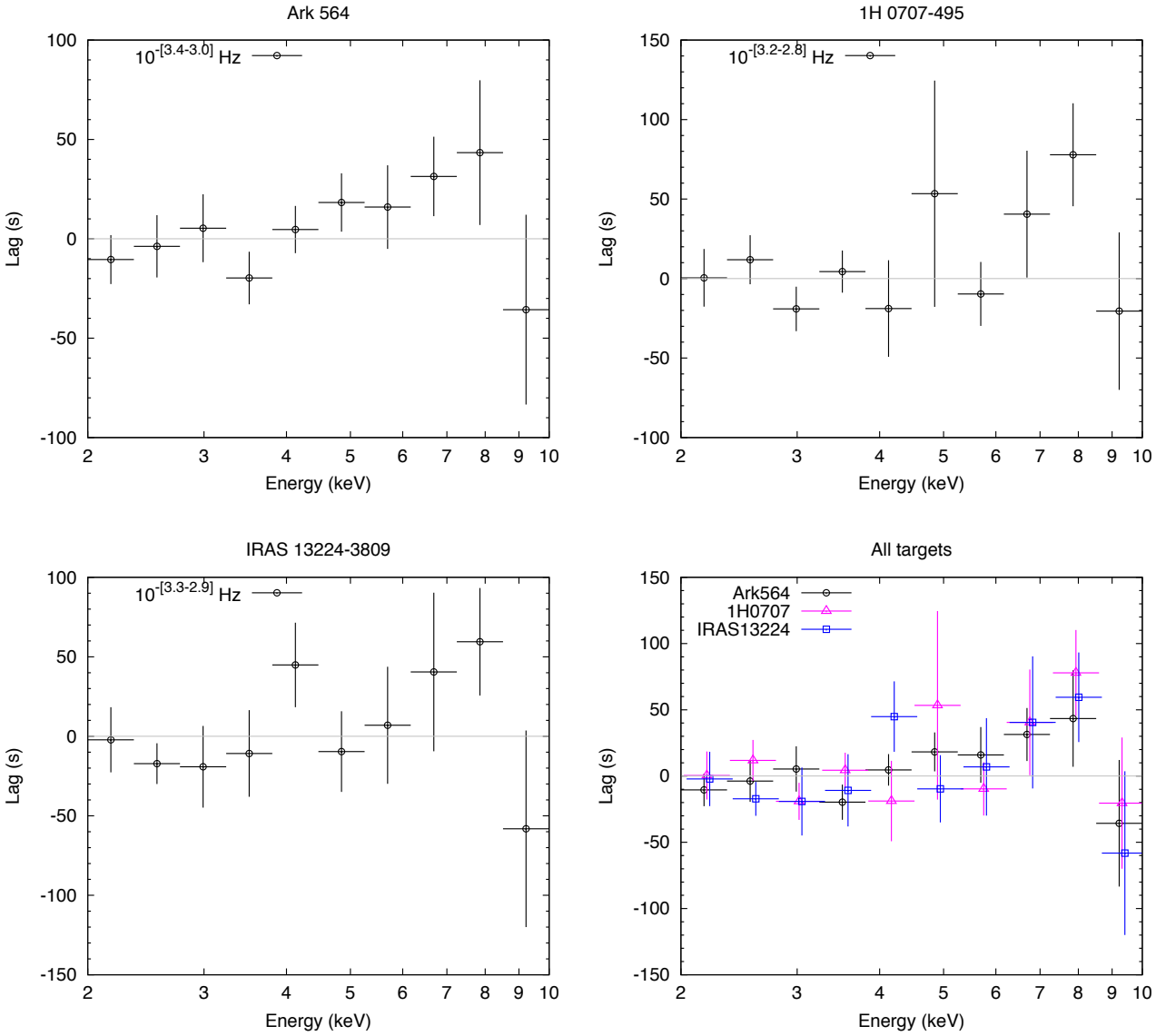

Figure 5.17: Lag-energy plots for the three targets in the highest frequency range where the Fe-K lags are seen. The right bottom panel shows the overplot of the three panels

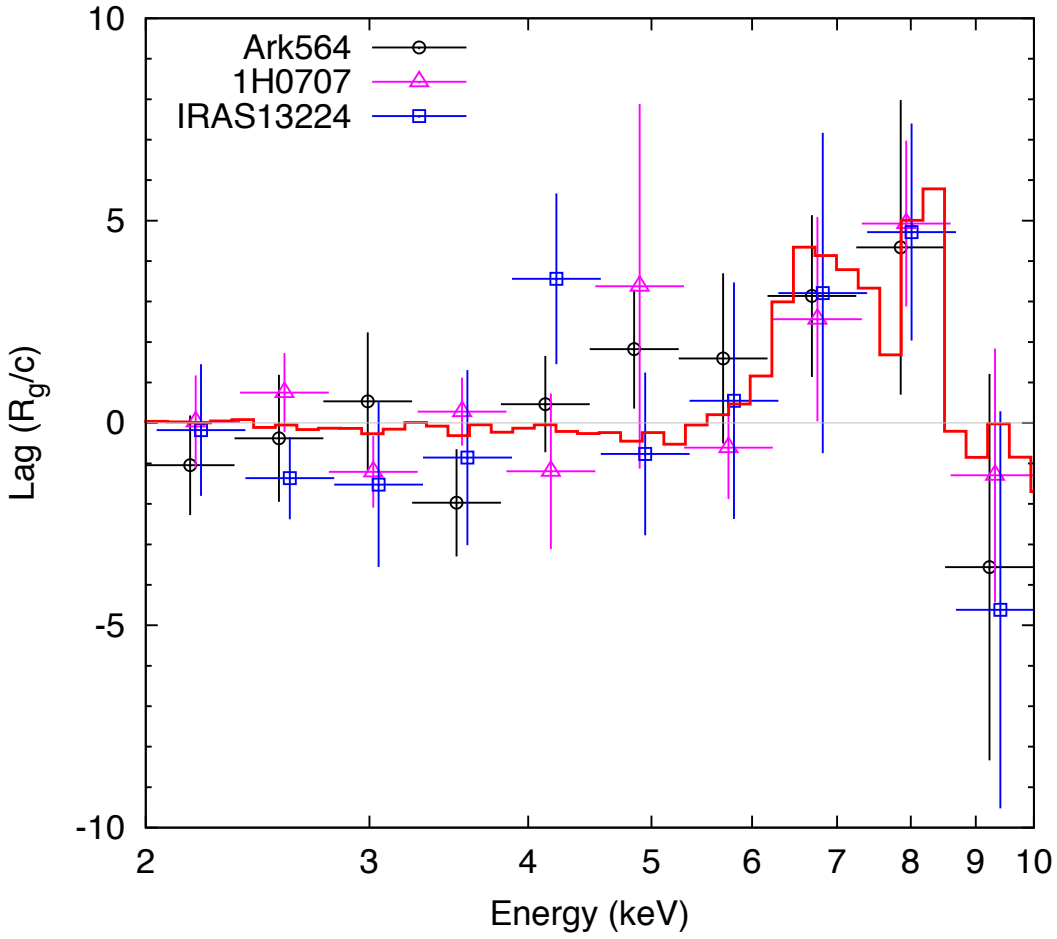

Figure 5.18: Lag-energy plots normalised by the gravitational radius with the biconical wind model ($f = c/250\,R_g$, $\cos i = [15/25 - 16/25]$). The BH masses are assumed to be $2 \times 10^6\,M_\odot$, $1.3 \times 10^6\,M_\odot$, and $1.6 \times 10^6\,M_\odot$ for Ark 564, 1H 0707–495, and IRAS 13224–3809, respectively, so that these plots have the same frequency range, between $c/250\,R_g$ and $c/100\,R_g$.

0707–495, and IRAS 13224–3809. The outflowing and ionised clouds launched at several R_g scatter incident X-ray photons and produce reverberation lags. Consequently, the observed lag features can be fully explained by the biconical wind.

Chapter 6

Discussion

6.1 Physical picture to explain the spectral variability

6.1.1 Disc winds and clumpy clouds

In Chapter 2, we mentioned that the line profile and rms dips in the Fe-K band of AGNs are explained by the partial covering model (see §2.4.2). Miyakawa et al. (2012) proposed that the partial absorbers have the internal structure with a non-ionised core and an ionised outer layer. This variable double partial covering model was found to be valid for other > 20 targets to explain their energy spectra and the rms spectra (Mizumoto et al. 2014; Iso et al. 2016; Yamasaki et al. 2016; Mizumoto & Ebisawa 2017); such double-layer absorbers are similar to the cometary cloud proposed by Maiolino et al. (2010). Mizumoto & Ebisawa (2017) investigated variability timescale of the partial absorbers and constrained their location as $\sim 10^3\, R_g$.

In the previous chapter, we have argued that the observed Fe-K reverberation lags can be explained by the disc winds. From theory sides, Takeuchi et al. (2013) and Kobayashi et al. (2018) suggested that the disc winds exhibit clumpy structures with a size of $\sim 10\, R_g$ above a height of $\sim 500\, R_g$. The gravitational force is diluted by r^{-2} from the central point, whereas the radiation force due to the accretion disc decreases more slowly as the radiation source is extended. In this case, the radiation force exceeds the gravitational force above a certain boundary, which results in the seemingly reverse gravitational field. Therefore, the heavier layer in the upper (inner) stream pushes the lighter one in the lower (outer) stream, which induces the Rayleigh-Taylor instability. Once the Rayleigh-Taylor instability is initiated, a radiation-hydrodynamic instability grows the clumpiness and the cold clumpy absorbers are naturally created in outer regions. This means that the two types of clouds, the inner disc winds explaining the Fe-K lags and the outer cold clumpy absorbers explaining the spectral profile and the rms dips, share the same origin. Indeed, this "disc wind + clumpy clouds" picture has been widely accepted (e.g., Gardner & Done 2015; Matzeu et al. 2016; Jin et al. 2017; Motta et al. 2017). In these manners, we conclude that all the three observational features in the Fe-K band of AGNs can be explained simultaneously in the cloud-reflection scenario.

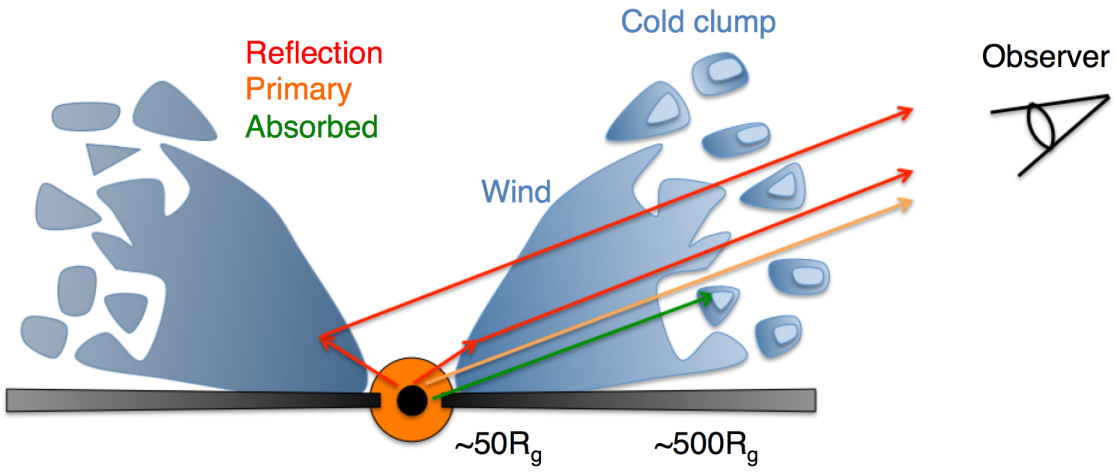

Figure 6.1: Physical picture to explain X-ray spectral variability in AGNs. The orange circle shows the X-ray emitting corona, whose size is an order of $10\,R_g$. Disc winds are launched at $\sim 30R_g$. The winds in the line-of-sight create blueshifted absorption lines as UFOs, and those out of the line-of-sight within $\sim 100\,R_g$ produce reverberation lags (red arrows). The winds exhibit clumpy structures at $\gtrsim 500\,R_g$, and make cold clumps. They partially cover the corona and make a deep Fe-K edge (orange and green arrows), which mimics the seemingly broad line feature. Change of the partial covering fraction produces the deep rms dip in the Fe-K band. Disc reflection is not shown here because it has minor contribution to the time lags (see the main text).

Our picture to explain the spectral variability of AGNs is as follows: An extended X-ray emission region whose size is $\sim 10\,R_g$ exist around the central BH. Outflowing clouds such as disc winds are launched at several tens of R_g. The continuous winds in the line of sight produce blueshifted absorption lines in the X-ray energy spectra, and those out of the line of sight ($\lesssim 100\,R_g$) produce reverberation lags. At $\gtrsim 500\,R_g$, cold clumpy absorbers of a scale of $\sim 10\,R_g$ are generated due to the density fluctuation of the wind triggered by instabilities. They partially cover the X-ray emission region and produce Fe-K edge in the energy spectra, which mimics the broad emission line. The clump has the inner structure with the cold core and the ionised outer layer, which may have the cometary structure. Variability of partial covering fraction produces the significant rms dips in the Fe-K band. This model can simultaneously and self-consistently explain all the observational facts concerning the Fe-K line features.

6.1.2 Contribution of the disc reflection

We argued that scattering materials within $100\,R_g$ affect the time-lags in Chapter 5. While the disc reflection at the very vicinity of the central BH ($< 10\,R_g$) is unlikely (Chapter 4), the disc reflection within $\sim 100\,R_g$ is expected to contribute to the lags. Therefore, in order to evaluate contribution of the disc reflection with $r = 10 - 100\,R_g$, we calculate the equivalent width of the iron line via MONACO. The disc is assumed to be neutral, optically-thick ($N_{\rm H} = 10^{26}$ cm^{-2} along the vertical axis), geometrically-thin ($h/r = 0.001$, where h is

thickness of the disc), and in Keplerian motion. In Chapter 5, we assumed that photons are emitted radially from a central point source, though in practice, the source should have a finite extent with $\sim 5-10\,R_g$. Here, to estimate effect of the maximum illumination of the accretion disc, we assume that a point source is located at $5\,R_g$ above the disc. In this case, the reflection scaling factor (i.e., solid angle of the disc within $10-100\,R_g$) is 40%. Figure 6.2 shows the simulated spectrum. We fitted the simulation result with a simple fitting model (powerlaw+positive Gaussian), and found that the iron line EW is 90 eV with $\sigma = 1$ keV (figure 6.3a). This EW is smaller than that of wind reflection (210 eV with $\sigma = 650$ eV; figure 6.3b), which means that contribution of the disc reflection to the time-lags is lower than the wind reflection, and that the wind reflection plays a major role to produce lag features.

6.2 Winds out of the line-of-sight

If the picture proposed in the previous section is correct, we can access the wind "out of the line-of-sight" using the Fe-K reverberation lags, while we have only been able to see the wind "in the line-of-sight" using absorption lines. If the sources are observed not directly through the wind, absorption lines are not seen while reverberation lags should be observed. Ark 564 is supposed to be one of such examples. Figure 6.4 shows X-ray energy spectra of the three targets the lags of which are investigated in §5.3.3. Although all the targets have similar Fe-K reverberation lags, their energy spectra are obviously different; IRAS 13224–3809 and 1H 0707–495 have deep Fe-K absorption edges/lines, whereas Ark 564 has only a weak Fe-K feature. To understand this obvious spectral difference, we conjecture that Ark 564 does not have the wind or cold clumps in the line-of-sight, while the wind exists out of the line-of-sight (figure 6.5). EW of the Fe-K broad emission line in Ark 564 is 200 eV with $\sigma = 650$ eV (figure 6.4), which is very similar to the one expected by the wind reflection (§6.1.2). In this manner, Ark 564 is considered to be a face-on target and its spectral and lag features are explained by the wind out of the line-of-sight.

Moreover, the reverberation lag due to the disc wind is expected to enable us to constrain the wind geometry. The lag amplitudes and the frequencies where the lag diminishes are directly related to the location of the wind (figure 5.7), and the lag amplitudes become longer with larger solid angles of the winds. Figure 6.6 shows the simulated lag-frequency plots in the ionised partial-shell-like clouds with three different solid angles. The more scattering materials exist in the larger solid angle, the larger the lag amplitudes get. Therefore, we may be able to constrain the solid angle of the winds with reverberation lags. Figure 6.7 shows Eddington ratio ($L_{\rm bol}/L_{\rm Edd}$) dependence of the lag parameters with *XMM-Newton* observations. These targets are listed in Kara et al. (2016), and the vertical axes are normalised by the BH mass. The lag frequencies have no dependence on $L_{\rm bol}/L_{\rm Edd}$, which suggests that the scattering materials are located at the same gravitational radius. On the other hand, Eddington ratios and the lag amplitudes seem to correlate with each other. This correlation implies that the solid angle is larger in the high Eddington ratio objects. It is known that the wind launching mechanism is dependent on the Eddington ratios. In the super-Eddington

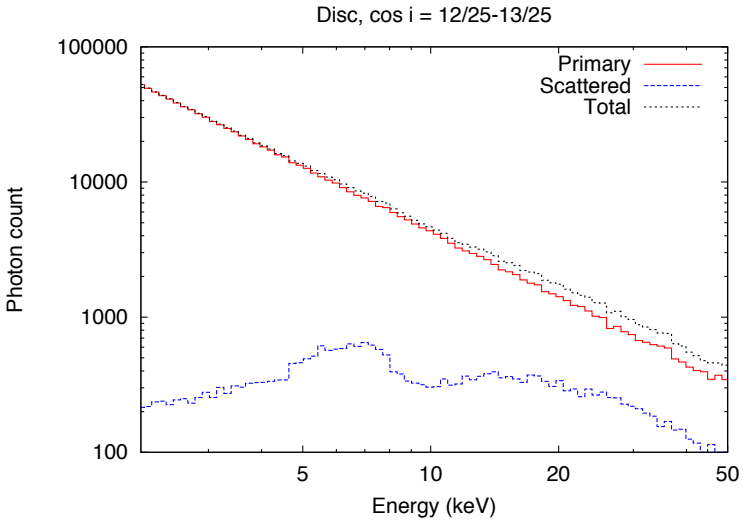

Figure 6.2: Simualted X-ray energy spectra for disc reflection when $\cos i = 12/25 - 13/25$. The radius of the disc is $10 - 100\,R_g$.

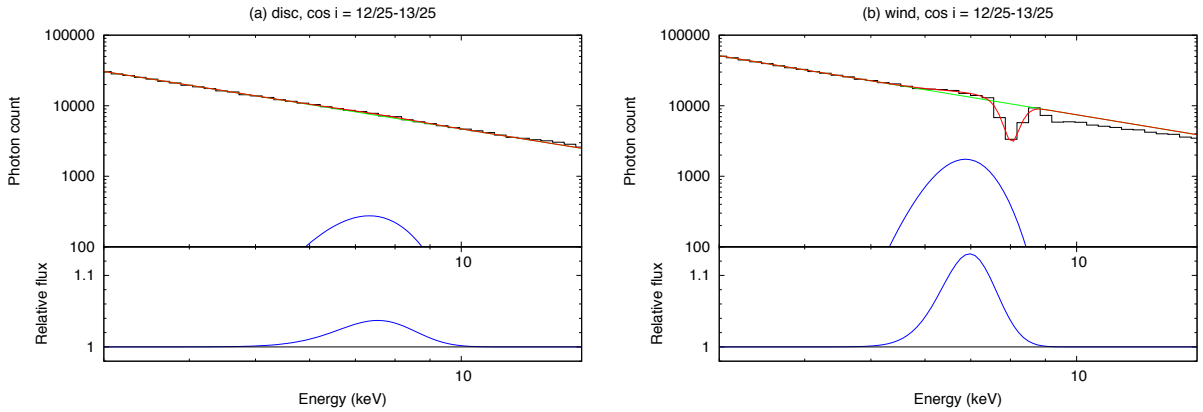

Figure 6.3: Fitting results of the disc reflection (a) and wind reflection (b, same as figure 5.14) when $\cos i = 12/25 - 13/25$. The fitting model is power-law+positive Gaussian(+negative Gaussian; only in the wind reflection). The black, red, green, blue lines show the simulation result, fitting model, power-law(+negative Gaussian), and positive Gaussian. The bottom panels shows the positive Gaussian normalised by the power-law continuum.

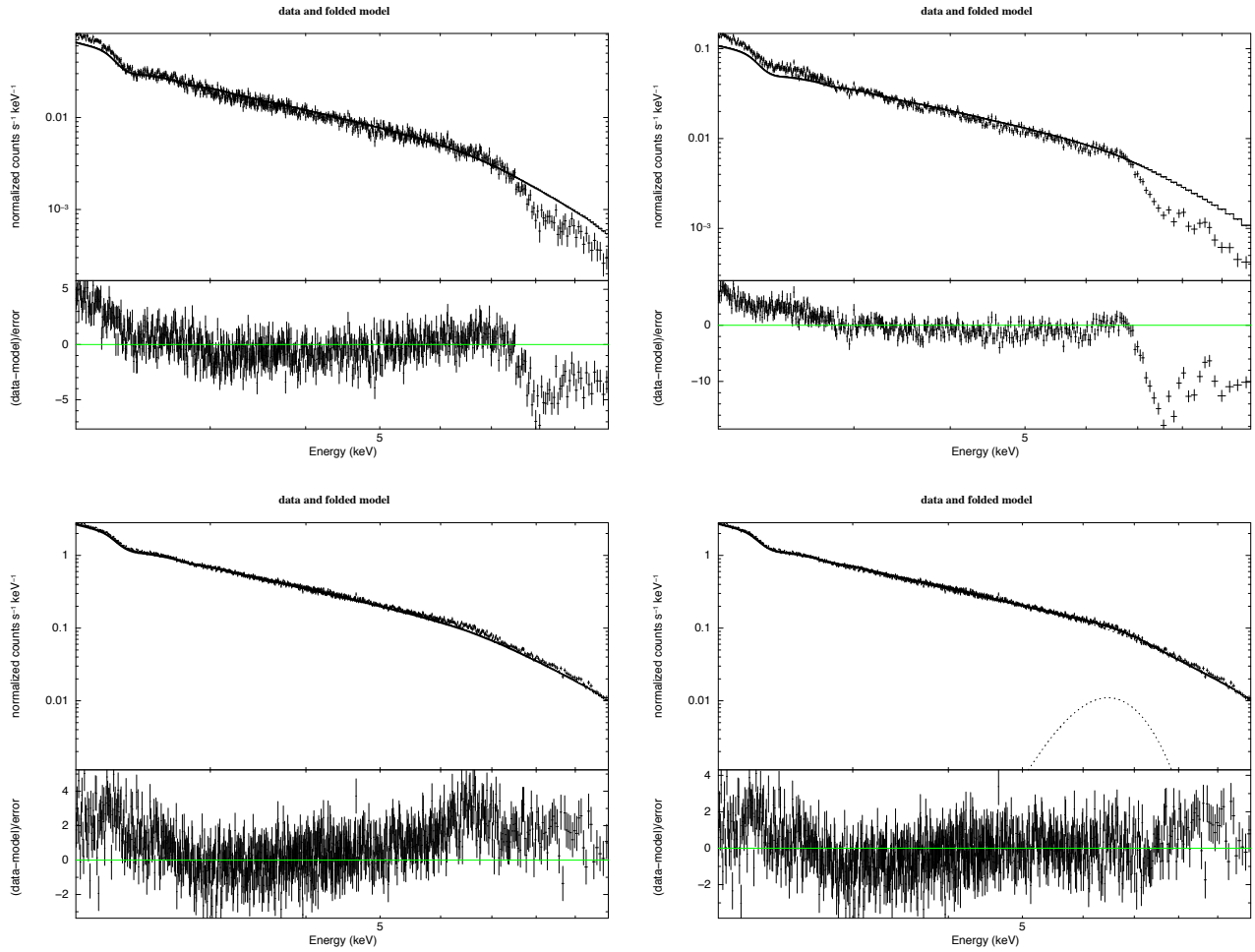

Figure 6.4: X-ray energy spectra of IRAS 13224–3809 (top left), 1H 0707–495 (top right), and Ark 564 (bottom left). The model lines show the power-law with $\Gamma = 2$ for IRAS 13224–3809 and 1H 0707–495, and 2.5 for Ark 564. The lower panels show residuals. Ark 564 shows a weak and broad iron emission line, whose EW is 200 eV and width is 650 eV, the fitting result of which is shown in the bottom right panel.

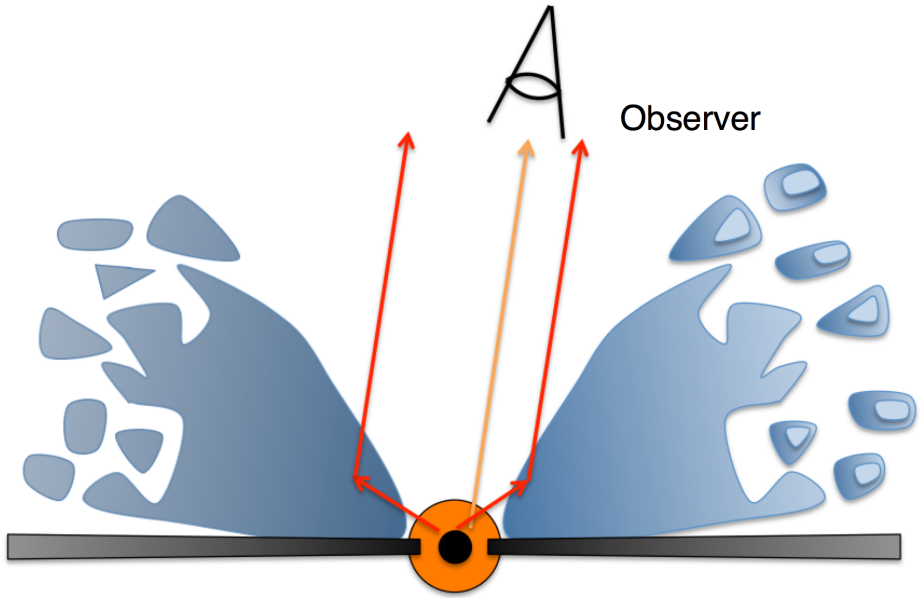

Figure 6.5: Physical picture of Ark 564, which is very similar to figure 6.1, besides the inclination angle

case, the radiation force with Thomson scattering exceeds the gravitation force (see equation 2.8). This type of winds is called as a "continuum-driven" wind, which is known to have large solid angles (e.g., Nardini et al. 2015). On the other hand, in the sub-Eddington case, the radiation force due to spectral lines more effectively accelerates materials, which is called as a "line-driven" wind (see figure 2.6). This wind may have a smaller solid angle than the continuum-driven wind.

In order to constrain the wind geometry more precisely, we need help of numerical simulations. We have calculated reverberation lags produced by the biconical wind geometry in §5.3, which is more or less realistic and easy to handle. We assumed that the physical parameters in a shell at the same radius are homogeneous in the biconical wind geometry, but the numerical simulation predicts that the actual disc wind has more complex geometries (also see figure 2.6). In order to take them into account, we plan to perform Monte-Carlo simulations using results of the hydro-dynamical numerical simulations. Density and velocity structures are given by the hydro-dynamical simulation, and the ionisation states can be calculated using XSTAR; in this way we may get realistic input information to Monte-Carlo simulation. Through such precise simulations, we will be able to investigate physical parameters of the disc wind in more detail, and compare with observations by future high-quality instruments such as Athena.

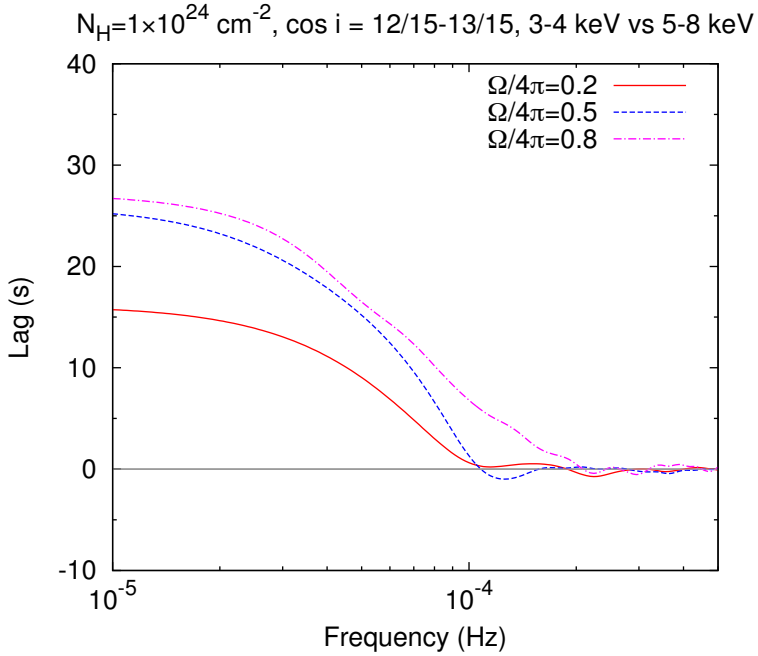

Figure 6.6: Lag-frequency plots for different solid angles in the partial-shell-like cloud with $\log \xi = 4.2$ and $N_{\rm H} = 1 \times 10^{24}$ cm^{-2}. The angle ranges where scattering materials exist are $36°.87 - 90°$, $60° - 90°$, and $78°.46 - 90°$ for $\Omega/4\pi = 0.2$, 0.5, 0.8, respectively.

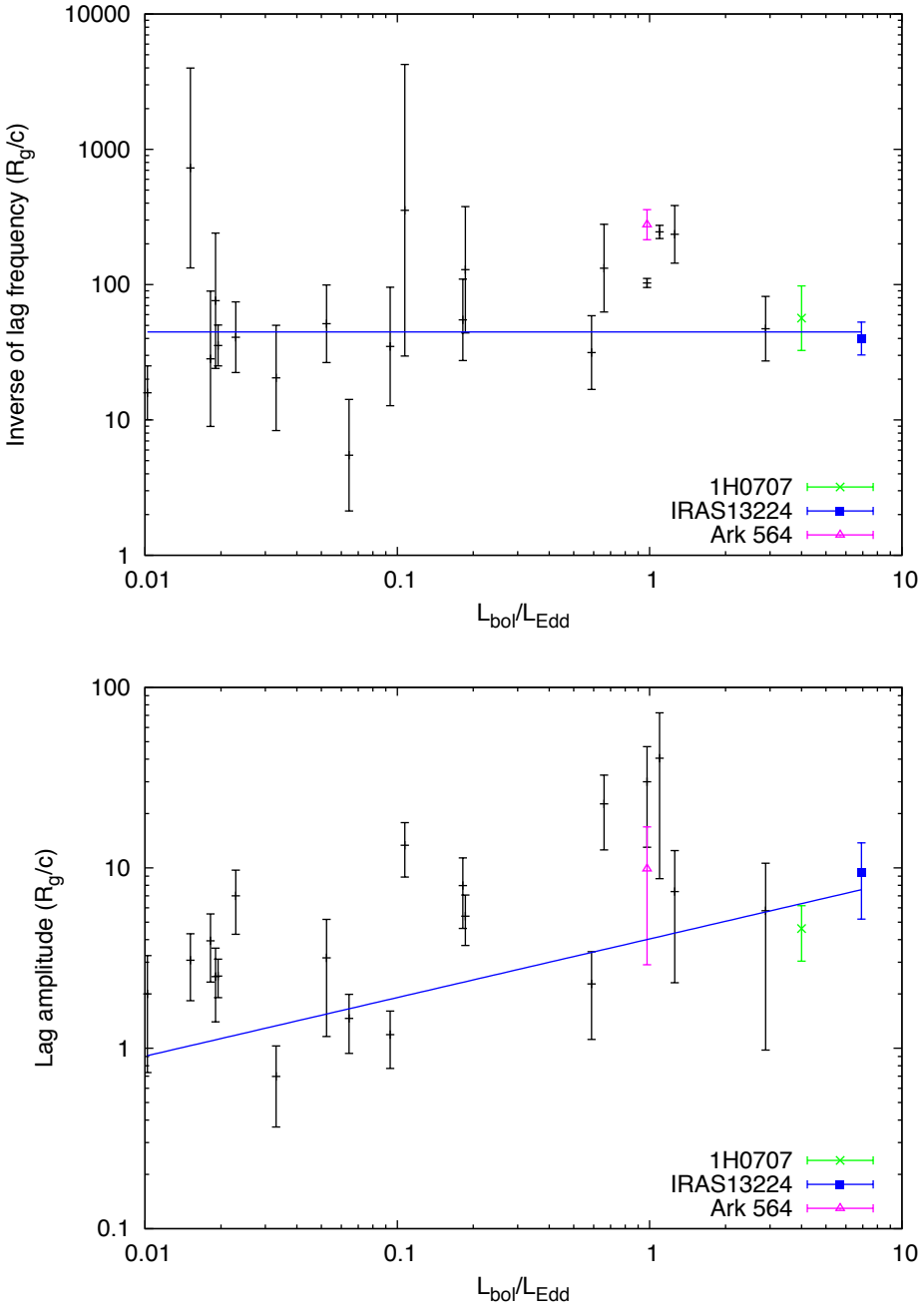

Figure 6.7: Eddington ratio ($L_{\rm bol}/L_{\rm Edd}$) dependence of the lag frequencies (upper) and the lag amplitudes (lower). We use the data listed in Kara et al. (2016). The vertical axes are normalised by the BH mass. The blue line show the best-fit linear function (log-log scale).

Chapter 7

Conclusion

X-ray spectra and spectral variability in the Fe-K band of AGNs are known to have three distinctive observational features; seemingly broad line feature in the 5–8 keV, deep root-mean-square (rms) dips up to ~ 50 %, and reverberation lags with the amplitudes of several R_g at the Fourier frequencies of $\sim c/100\,R_g$ Hz. We have examined the two major scenarios proposed to explain these features, the disc-reflection scenario and the cloud-reflection scenario by simulating the spectral variations and comparing them with actual observations. We focus on the 2–10 keV band with the variation timescale of $\lesssim 1$ day.

In the disc-reflection scenario, where a lamp post with constant luminosity is moving vertically along the rotation axis, it has been believed that the rms dips are explained by combination of variable Power-Law Component (PLC) and invariable Reflection-Dominated Component (RDC). However, through a ray-tracing calculation, we found that the RDC shows significant variability when the source height is changed, and thus the iron overabundance up to 10 times solar is required to explain the observed depth of the rms dip. On the other hand, the lag profile in the same target is consistent with the solar abundance of iron, and such a high iron overabundance is rejected. Consequently, we conclude that it is difficult to explain the observed features with the disc-reflection scenario.

In the cloud-reflection scenario, the spectral feature and rms dips have been already explained, so we tried to explain the lags with the cloud-reflection model for the first time. First, we assumed a neutral, part-spherical thin shell at $100\,R_g$ with an outflowing velocity. As a result, we found short-time ($\lesssim 3\,R_g/c$) hard lags in the frequency range of $\lesssim c/100\,R_g$ Hz. The short lag amplitude compared to the light-travel time is explained by the "dilution effect", such that majority of the photons in the Fe-K energy band are the primary photons without time-delay, whereas the time-delayed reprocessed photons have minor contribution. The observed broad line features in the lag-energy plot are explained by Doppler shifts of the outflowing materials. Hence, it is shown that the observed X-ray lag features can be produced by the outflowing matter at $\lesssim 100\,R_g$. Next, we calculated lags on a more realistic disc-wind geometry, and compared the results with the observations. We found that the outflowing and ionised clouds launched at several tens of R_g scatter incident X-ray photons and produce reverberation lags. Consequently, the observed lag features can be fully explained by the disc wind, or the cloud-reflection scenario.

Our picture to explain X-ray spectral variability of AGNs is as follows: An extended X-ray emission region whose size is $\sim 10\,R_g$ exist around the central BH. Outflowing clouds such as disc winds are launched at several tens of R_g, and produce reverberation lags. At $\gtrsim 500\,R_g$, clumpy cold absorbers are generated due to density fluctuation of the wind triggered by instabilities. The cold absorbers partially cover the X-ray emission region and produce Fe-K edge in the energy spectra, which mimics the broad emission line. Variability of the partial covering fraction produces the rms dips. This model simultaneously and self-consistently explains the observed features of X-ray variability in the Fe-K band.

Bibliography

Abramowicz, M. A., Czerny, B., Lasota, J. P., & Szuszkiewicz, E. 1988, *Astrophysical Journal*, 332, 646

Agostinelli, S., Allison, J., Amako, K., et al. 2003, Nuclear Instruments and Methods in Physics Research A, 506, 250

Akiyama, K., Kuramochi, K., Ikeda, S., et al. 2017, *Astrophysical Journal*, 838, 1

Allison, J., Amako, K., Apostolakis, J., et al. 2006, IEEE Transactions on Nuclear Science, 53, 270

Boller, T., Brandt, W. N., Fabian, A. C., & Fink, H. H. 1997, *Monthly Notices of the Royal Astronomical Society*, 289, 393

Boller, T., Tanaka, Y., Fabian, A., et al. 2003, *Monthly Notices of the Royal Astronomical Society*, 343, L89

Bonson, K. & Gallo, L. C. 2016, *Monthly Notices of the Royal Astronomical Society*, 458, 1927

Cackett, E. M., Zoghbi, A., Reynolds, C., et al. 2014, *Monthly Notices of the Royal Astronomical Society*, 438, 2980

Castor, J. I., Abbott, D. C., & Klein, R. I. 1975, *Astrophysical Journal*, 195, 157

Chiang, C.-Y., Walton, D. J., Fabian, A. C., Wilkins, D. R., & Gallo, L. C. 2015, *Monthly Notices of the Royal Astronomical Society*, 446, 759

Dewangan, G. C., Boller, T., Singh, K. P., & Leighly, K. M. 2002, *Astronomy & Astrophysics*, 390, 65

Dove, J. B., Wilms, J., & Begelman, M. C. 1997, *Astrophysical Journal*, 487, 747

Edelson, R., Turner, T. J., Pounds, K., et al. 2002, *Astrophysical Journal*, 568, 610

Emmanoulopoulos, D., Papadakis, I. E., Dovčiak, M., & McHardy, I. M. 2014, *Monthly Notices of the Royal Astronomical Society*, 439, 3931

Fabian, A. C., Ballantyne, D. R., Merloni, A., et al. 2002a, *Monthly Notices of the Royal Astronomical Society*, 331, L35

Fabian, A. C., Iwasawa, K., Reynolds, C. S., & Young, A. J. 2000, *Publication of Astronomical Society of Pacific*, 112, 1145

Fabian, A. C., Kara, E., Walton, D. J., et al. 2013, *Monthly Notices of the Royal Astronomical Society*, 429, 2917

Fabian, A. C., Rees, M. J., Stella, L., & White, N. E. 1989, *Monthly Notices of the Royal Astronomical Society*, 238, 729

Fabian, A. C., Vaughan, S., Nandra, K., et al. 2002b, *Monthly Notices of the Royal Astronomical Society*, 335, L1

Fath, E. A. 1909, *Popular Astronomy*, 17, 504

Gardner, E. & Done, C. 2015, *Monthly Notices of the Royal Astronomical Society*, 448, 2245

George, I. M. & Fabian, A. C. 1991, *Monthly Notices of the Royal Astronomical Society*, 249, 352

Gofford, J., Reeves, J. N., McLaughlin, D. E., et al. 2015, *Monthly Notices of the Royal Astronomical Society*, 451, 4169

Gofford, J., Reeves, J. N., Tombesi, F., et al. 2013, *Monthly Notices of the Royal Astronomical Society*, 430, 60

González-Martín, O. & Vaughan, S. 2012, *Astronomy & Astrophysics*, 544, A80

Hagino, K., Odaka, H., Done, C., et al. 2015, *Monthly Notices of the Royal Astronomical Society*, 446, 663

Hagino, K., Odaka, H., Done, C., et al. 2016, *Monthly Notices of the Royal Astronomical Society*, 461, 3954

Hashizume, K., Ohsuga, K., Kawashima, T., & Tanaka, M. 2015, *Publication of Astronomical Society of Japan*, 67, 58

Hitomi Collaboration. 2016, *Nature*, 535, 117

Hitomi Collaboration. 2017, accepted for *Publication of Astronomical Society of Japan*

Hoormann, J. K., Beheshtipour, B., & Krawczynski, H. 2016, *Physical Review D*, 93, 044020

Inoue, H. & Matsumoto, C. 2003, *Publication of Astronomical Society of Japan*, 55, 625

Iso, N., Ebisawa, K., Sameshima, H., et al. 2016, *Publication of Astronomical Society of Japan*, 68, S27

Jansen, F., Lumb, D., Altieri, B., et al. 2001, Astronomy & Astrophysics, 365, L1

Jin, C., Done, C., Ward, M., & Gardner, E. 2017, *Monthly Notices of the Royal Astronomical Society*, 471, 706

Kallman, T. R., Palmeri, P., Bautista, M. A., Mendoza, C., & Krolik, J. H. 2004, *Astrophysical Journal Supplement*, 155, 675

Kara, E., Alston, W. N., Fabian, A. C., et al. 2016, *Monthly Notices of the Royal Astronomical Society*, 462, 511

Kara, E., Fabian, A. C., Cackett, E. M., Miniutti, G., & Uttley, P. 2013a, *Monthly Notices of the Royal Astronomical Society*, 430, 1408

Kara, E., Fabian, A. C., Cackett, E. M., et al. 2013b, *Monthly Notices of the Royal Astronomical Society*, 428, 2795

Kara, E., Fabian, A. C., Cackett, E. M., et al. 2013c, *Monthly Notices of the Royal Astronomical Society*, 434, 1129

Karas, V., Vokrouhlicky, D., & Polnarev, A. G. 1992, *Monthly Notices of the Royal Astronomical Society*, 259, 569

Kelley, R. L., Akamatsu, H., Azzarello, P., et al. 2016, in *Proceedings of SPIE*, Vol. 9905, Space Telescopes and Instrumentation 2016: Ultraviolet to Gamma Ray, 99050V

Knigge, C., Woods, J. A., & Drew, J. E. 1995, *Monthly Notices of the Royal Astronomical Society*, 273, 225

Kobayashi, H., Ohsuga, K., Takahashi, H. R., et al. 2018, *Publication of Astronomical Society of Japan*, accepted (arXiv: 1802.00567)

Koratkar, A. & Blaes, O. 1999, *Publication of Astronomical Society of Pacific*, 111, 1

Krolik, J. H. & Kriss, G. A. 1995, *Astrophysical Journal*, 447, 512

Maiolino, R., Risaliti, G., Salvati, M., et al. 2010, *Astronomy & Astrophysics*, 517, A47

Matsumoto, C., Inoue, H., Fabian, A. C., & Iwasawa, K. 2003, *Publication of Astronomical Society of Japan*, 55, 615

Matt, G., Brandt, W. N., & Fabian, A. C. 1996, *Monthly Notices of the Royal Astronomical Society*, 280, 823

Matt, G., Fabian, A. C., & Ross, R. R. 1993, *Monthly Notices of the Royal Astronomical Society*, 262, 179

Matthews, T. A. & Sandage, A. R. 1963, *Astrophysical Journal*, 138, 30

Matzeu, G. A., Reeves, J. N., Nardini, E., et al. 2016, *Monthly Notices of the Royal Astronomical Society*, 458, 1311

Miller, J. M. 2007, *Annual Review of Astronomy and Astrophysics*, 45, 441

Miller, L., Turner, T. J., Reeves, J. N., & Braito, V. 2010a, *Monthly Notices of the Royal Astronomical Society*, 408, 1928

Miller, L., Turner, T. J., Reeves, J. N., et al. 2010b, *Monthly Notices of the Royal Astronomical Society*, 403, 196

Mineshige, S., Kawaguchi, T., Takeuchi, M., & Hayashida, K. 2000, *Publication of Astronomical Society of Japan*, 52, 499

Miniutti, G. & Fabian, A. C. 2004, *Monthly Notices of the Royal Astronomical Society*, 349, 1435

Miniutti, G., Fabian, A. C., Anabuki, N., et al. 2007, *Publication of Astronomical Society of Japan*, 59, 315

Miniutti, G., Fabian, A. C., Goyder, R., & Lasenby, A. N. 2003, *Monthly Notices of the Royal Astronomical Society*, 344, L22

Mitsuda, K., Bautz, M., Inoue, H., et al. 2007, *Publication of Astronomical Society of Japan*, 59, 1

Mitsuda, K., Inoue, H., Koyama, K., et al. 1984, *Publication of Astronomical Society of Japan*, 36, 741

Miyakawa, T., Ebisawa, K., & Inoue, H. 2012, *Publication of Astronomical Society of Japan*, 64, 140

Mizumoto, M. & Ebisawa, K. 2017, *Monthly Notices of the Royal Astronomical Society*, 466, 3259

Mizumoto, M., Ebisawa, K., & Sameshima, H. 2014, *Publication of Astronomical Society of Japan*, 66, 122

Mizumoto, M., Ebisawa, K., Tsujimoto, M., & Inoue, H. 2016, *Astronomische Nachrichten*, 337, 507

Moriyama, K. & Mineshige, S. 2015, *Publication of Astronomical Society of Japan*, 67, 106

Morrison, R. & McCammon, D. 1983, *Astrophysical Journal*, 270, 119

Motta, S. E., Kajava, J. J. E., Sánchez-Fernández, C., et al. 2017, *Monthly Notices of the Royal Astronomical Society*, 471, 1797

Mushotzky, R. F., Done, C., & Pounds, K. A. 1993, *Annual Review of Astronomy and Astrophysics*, 31, 717

Nandra, K., O'Neill, P. M., George, I. M., & Reeves, J. N. 2007, *Monthly Notices of the Royal Astronomical Society*, 382, 194

Nardini, E., Reeves, J. N., Gofford, J., et al. 2015, Science, 347, 860

Nicastro, F., Fiore, F., Perola, G. C., & Elvis, M. 1999, *Astrophysical Journal*, 512, 184

Niedźwiecki, A. & Miyakawa, T. 2010, *Astronomy & Astrophysics*, 509, A22

Noda, H., Makishima, K., Nakazawa, K., et al. 2013a, *Publication of Astronomical Society of Japan*, 65, 4

Noda, H., Makishima, K., Nakazawa, K., & Yamada, S. 2013b, *Astrophysical Journal*, 771, 100

Noda, H., Makishima, K., Uehara, Y., Yamada, S., & Nakazawa, K. 2011a, *Publication of Astronomical Society of Japan*, 63, 449

Noda, H., Makishima, K., Yamada, S., et al. 2014, *Astrophysical Journal*, 794, 2

Noda, H., Makishima, K., Yamada, S., et al. 2011b, *Publication of Astronomical Society of Japan*, 63, S925

Nomura, M., Ohsuga, K., Takahashi, H. R., Wada, K., & Yoshida, T. 2016, *Publication of Astronomical Society of Japan*, 68, 16

Nowak, M. A., Vaughan, B. A., Wilms, J., Dove, J. B., & Begelman, M. C. 1999, *Astrophysical Journal*, 510, 874

Odaka, H., Aharonian, F., Watanabe, S., et al. 2011, *Astrophysical Journal*, 740, 103

Onishi, K., Iguchi, S., Sheth, K., & Kohno, K. 2015, *Astrophysical Journal*, 806, 39

Parker, M. L., Pinto, C., Fabian, A. C., et al. 2017, *Nature*, 543, 83

Pious, J. K., Balakrishna, K. M., Lingappa, N., & Siddappa, K. 1992, *Journal of Physics B: Atomic, Molecular and Optical Physics*, 25, 1155

Ponti, G., Papadakis, I., Bianchi, S., et al. 2012, *Astronomy & Astrophysics*, 542, A83

Proga, D. & Kallman, T. R. 2004, *Astrophysical Journal*, 616, 688

Proga, D., Stone, J. M., & Kallman, T. R. 2000, *Astrophysical Journal*, 543, 686

Reynolds, C. S. & Nowak, M. A. 2003, *Physics Reports*, 377, 389

Reynolds, C. S., Young, A. J., Begelman, M. C., & Fabian, A. C. 1999, *Astrophysical Journal*, 514, 164

Ross, R. R. & Fabian, A. C. 1993, *Monthly Notices of the Royal Astronomical Society*, 261, 74

Schmidt, M. 1963, *Nature*, 197, 1040

Seyfert, C. K. 1943, *Astrophysical Journal*, 97, 28

Shakura, N. I. & Sunyaev, R. A. 1973, *Astronomy & Astrophysics*, 24, 337

Shlosman, I. & Vitello, P. 1993, *Astrophysical Journal*, 409, 372

Shull, J. M. & van Steenberg, M. 1982, *Astrophysical Journal Supplement*, 48, 95

Sim, S. A., Long, K. S., Miller, L., & Turner, T. J. 2008, *Monthly Notices of the Royal Astronomical Society*, 388, 611

Sim, S. A., Miller, L., Long, K. S., Turner, T. J., & Reeves, J. N. 2010, *Monthly Notices of the Royal Astronomical Society*, 404, 1369

Sobolewska, M. A. & Done, C. 2007, *Monthly Notices of the Royal Astronomical Society*, 374, 150

Stern, B. E., Poutanen, J., Svensson, R., Sikora, M., & Begelman, M. C. 1995, *Astrophysical Journal Letters*, 449, L13

Stevens, I. R. & Kallman, T. R. 1990, *Astrophysical Journal*, 365, 321

Strüder, L., Briel, U., Dennerl, K., et al. 2001, Astronomy & Astrophysics, 365, L18

Sunyaev, R. A. & Truemper, J. 1979, *Nature*, 279, 506

Takahashi, T., Kokubun, M., Mitsuda, K., et al. 2016, in *Proceedings of SPIE*, Vol. 9905, Space Telescopes and Instrumentation 2016: Ultraviolet to Gamma Ray, 99050U

Takeuchi, S., Ohsuga, K., & Mineshige, S. 2013, *Publication of Astronomical Society of Japan*, 65, 88

Tanaka, Y., Boller, T., Gallo, L., Keil, R., & Ueda, Y. 2004, *Publication of Astronomical Society of Japan*, 56, L9

Tanaka, Y., Nandra, K., Fabian, A. C., et al. 1995, *Nature*, 375, 659

Terashima, Y., Gallo, L. C., Inoue, H., et al. 2009, *Publication of Astronomical Society of Japan*, 61, S299

Thorne, K. S. & Price, R. H. 1975, *Astrophysical Journal Letters*, 195, L101

Tombesi, F., Cappi, M., Reeves, J. N., et al. 2011, *Astrophysical Journal*, 742, 44

Tombesi, F., Cappi, M., Reeves, J. N., et al. 2010, *Astronomy & Astrophysics*, 521, A57

Turner, T. J. & Miller, L. 2009, *Astronomy & Astrophysics Review*, 17, 47

Turner, T. J., Miller, L., Reeves, J. N., & Braito, V. 2017, *Monthly Notices of the Royal Astronomical Society*, 467, 3924

Uttley, P., Cackett, E. M., Fabian, A. C., Kara, E., & Wilkins, D. R. 2014, *Astronomy & Astrophysics Review*, 22, 72

Życki, P. T., Ebisawa, K., Niedźwiecki, A., & Miyakawa, T. 2010, *Publication of Astronomical Society of Japan*, 62, 1185

Vaughan, B. A. & Nowak, M. A. 1997, *Astrophysical Journal Letters*, 474, L43

Watanabe, S., Sako, M., Ishida, M., et al. 2006, *Astrophysical Journal*, 651, 421

Wilkins, D. R. & Fabian, A. C. 2013, *Monthly Notices of the Royal Astronomical Society*, 430, 247

Yamasaki, H., Mizumoto, M., Ebisawa, K., & Sameshima, H. 2016, *Publication of Astronomical Society of Japan*, 68, 80

Yoshida, H. 1993, *Celestial Mechanics and Dynamical Astronomy*, 56, 27

Zhou, X.-L. & Wang, J.-M. 2005, *Astrophysical Journal Letters*, 618, L83

Appendix A

Calculation method of the relativistic light bending model

We describe a relativistic light bending model and methods of the numerical calculation used in §4. In this appendix, we use "geometrised units" in which G and c are set to be unity.

A.1 Model and assumption

First, we consider the photons to directly reach the observer. The height, radial position and 4-velocity of the source are denoted by $h_{\rm s}$, $\rho_{\rm s}$ and $u^\mu_\ell = (u^0_\ell, 0, 0, u^3_\ell)$ (see figure 4.1). In its inertial frame, the radiation energy per unit time, and energy, $dW_\ell(e_\ell, t)/dt$, is defined as

$$\frac{dW_\ell(e_\ell, t)}{dt} de_\ell = N e_\ell^{-\Gamma+1} \delta(t) de_\ell, \tag{A.1}$$

where N is the photon number, e_ℓ is the photon energy, t is the Boyer-Lindquist time coordinate, and Γ $(= 2)$ is the spectral index. The primary continuum emission to reach directly to the observer from the emitter is expressed as

$$\begin{aligned} \frac{dW_{\rm p}(e_{\rm obs}, t)}{dt} de_{\rm obs} &= g_0^2 \frac{dW_\ell(e_\ell, t-\tau_{\rm p})}{dt} de_\ell \\ &= g_0^\Gamma N e_{\rm obs}^{-\Gamma+1} \delta(t-\tau_{\rm p}) de_{\rm obs}, \end{aligned} \tag{A.2}$$

where $e_{\rm obs}$ is the observed photon energy, and $\tau_{\rm p} (= \ell_{\rm p})$ is the time taken for a photon from the source to reach the observer's plane. Further, g_0 is the energy-shift factor between the observer and source, and is written as

$$g_0 = \frac{e_{\rm obs}}{e_\ell} = \frac{1}{u^0_\ell (1 - \Omega_\ell \Lambda)}, \tag{A.3}$$

where $\Omega_\ell = u^3_\ell / u^0_\ell$ is the angular velocity of the source, and Λ is the angular momentum of the photon with respect to the azimuth direction (ϕ) per energy. Therefore, the total photon flux to reach the observer, $F_{\rm p}(e_{\rm obs}, t) de_{\rm obs}$, is written as

$$F_{\rm p}(e_{\rm obs}, t) de_{\rm obs} = g_0^\Gamma N'_{\rm p} e_{\rm obs}^{-\Gamma} \delta(t - \tau_{\rm p}) de_{\rm obs}, \tag{A.4}$$

where $N'_{\rm p}$ is the photon number to reach the observer's plane per unit area.

Next, we consider the incident photon in the comoving frame of the accretion disc. The incident energy flux entering the gas element of the disc located at (r, ϕ), is expressed as

$$\begin{aligned} \frac{dW_{\rm d}(e_{\rm d}, t)}{dtdS_{\rm d}} de_{\rm d} &= g_1^2 \frac{dW_\ell(e_\ell, t-\tau_{\rm d})}{dtdS_{\rm d}} de_\ell \\ &= g_1^\Gamma N'_{\rm d} e_{\rm d}^{-\Gamma+1} \delta(t-\tau_{\rm d}) de_{\rm d}, \end{aligned} \tag{A.5}$$

where $N'_{\rm d}$ is the incident photon number per unit area, $dS_{\rm d}$ is the disc area element, $e_{\rm d}$ is the energy of the incident photon in the comoving frame, and $\tau_{\rm d}$ is the photon path length between the source and gas element (see figure 4.1). Further, the energy shift factor between the source and disc, g_1, is written by

$$g_1 = \frac{u^0_{\rm d}(1-\Omega_{\rm d}\Lambda)}{u^0_\ell(1-\Omega_\ell\Lambda)}, \tag{A.6}$$

where $u^\mu_{\rm d}$ and Ω_d is the 4-velocity and angular velocity of the disc element.

Photons in the fluorescent Kα line and the reflected continuum from the disc element are regarded as the reflection component. Probabilities that the fluorescent Kα line (6.4 keV at the rest frame) and the reflected continuum are emitted from the disc element, $P_{\rm K\alpha}$ and $P_{\rm scat}$, are expressed as

$$P_{\rm K\alpha}(e_{\rm d}) = W_{\rm K} \frac{\sigma_{\rm a}(e_{\rm d})}{\sigma_{\rm a}(e_{\rm d}) + \sigma_{\rm s}(e_{\rm d})}, \tag{A.7}$$

$$P_{\rm scat}(e_{\rm d}) = \frac{\sigma_{\rm s}(e_{\rm d})}{\sigma_{\rm a}(e_{\rm d}) + \sigma_{\rm s}(e_{\rm d})}, \tag{A.8}$$

where $e_{\rm d}$ is the energy of the incident photon in the comoving frame, $W_{\rm K}[= 0.35\ (0)$ for $e \geq E_{\rm e} = 7.112\,{\rm keV}\ (e < E_{\rm e})]$ is the iron Kα fluorescence yield (Pious et al. 1992), $\sigma_{\rm a}(e)$ is the iron photoelectric absorption cross-section (table 2 in Morrison & McCammon 1983), and $\sigma_{\rm s}(e)$ is the electron scattering cross-section given by the Klein-Nishina formula, such as

$$\sigma_{\rm a}(e) = \sigma_{\rm T} \frac{3}{4} \left[\frac{1+e}{e^3} \left\{ \frac{2e(1+e)}{1+2e} - \ln(1+2e) \right\} + \frac{\ln(1+2e)}{2e} - \frac{1+3e}{(1+2e)^2} \right], \tag{A.9}$$

where $\sigma_{\rm T}$ is the Thomson cross-section.

In the comoving frame of the gas element at (r, ϕ), reflected photon flux, $F_{\rm d}(e_{\rm d}, t)$ is expressed as

$$F_{\rm d}(e_{\rm d}, t) = F_{\rm K\alpha}(e_{\rm d}, t) + F_{\rm scat}(e_{\rm d}, t), \tag{A.10}$$

where $F_{\rm K\alpha}$ and $F_{\rm scat}$ are the photon flux of the fluorescent Kα line and reflected continuum radiation, and are defined as

$$\begin{aligned} F_{\rm K\alpha}(e_{\rm d}, t) &= g_1^\Gamma N'_d \delta(e_{\rm d} - 6.40\,{\rm keV}) \delta(t-\tau_{\rm d}) \int_{E_{\rm e}}^\infty P_{\rm K\alpha}(e) e^{-\Gamma} de \\ F_{\rm scat}(e_{\rm d}, t) &= g_1^\Gamma N'_{\rm d} \delta(t-\tau_{\rm d}) e_{\rm d}^{-\Gamma} P_{\rm scat}(e_{\rm d}). \end{aligned} \tag{A.11}$$

Therefore the radiative energy per unit time, energy, and solid angle is written as

$$\frac{dW_{\rm rev}(e_{\rm d}, t)}{dtd\Omega dS_{\rm d}} = \frac{e_{\rm d}}{4\pi} F_{\rm d}(e_{\rm d}, t). \tag{A.12}$$

The emissivity of the fluorescent Kα line, j, is proportional to $F_{\mathrm{K}\alpha}$:

$$j(r,\phi) = Jg_1(r,\phi)^{\Gamma} N'_d(r,\phi) \int_{E_{\mathrm{e}}}^{\infty} P_{\mathrm{K}\alpha}(e) e^{-\Gamma} de \quad (J = \text{const.}). \tag{A.13}$$

Finally, we consider the total radiation energy of the photons to reach the observer. The observed radiation emitted from a disc element located at (r,ϕ) is expressed as

$$\left[\frac{dW_{\mathrm{obs}}(e_{\mathrm{obs}},t)}{dtd\Omega dS_{\mathrm{obs}}}\right]_j = \left[g_2^2 \frac{e_{\mathrm{obs}}}{4\pi} F_{\mathrm{d}}(e_{\mathrm{obs}}/g_2, t-\tau_{\mathrm{r}})\right]_j \tag{A.14}$$

$$g_2 = \frac{e_{\mathrm{obs}}}{e_{\mathrm{d}}} = \frac{1}{u^0(1-\Omega_{\mathrm{d}}\Lambda_{\mathrm{r}})} \tag{A.15}$$

$$\Lambda_{\mathrm{r}} = -x_{\mathrm{obs}} \sin\theta_{\mathrm{obs}}, \tag{A.16}$$

where $(dS_{\mathrm{obs}})_j$ is the disc element, e_{obs} is the observed photon energy, τ_{r} is the time taken for a photon from the gas element to reach the observer's plane. The ray reaches the Cartesian coordinate on the observer's plane, $(x_{\mathrm{obs}}, y_{\mathrm{obs}})$, with the angular momentum of the photon with respect to the ϕ direction per energy, Λ_{r} (figure 4.1). The suffix "j" is the number of each cell of the observer's plane.

Thus the total energy flux to reach the observer's plane is expressed as

$$\begin{aligned} F_{\mathrm{tot}} &= \sum_j \left(\frac{dW_{\mathrm{obs}}(e_{\mathrm{obs}}, t-\tau_{\mathrm{r}})}{dtdS_{\mathrm{obs}}} de_{\mathrm{obs}}\right)_j \\ &= \sum_j \left[\frac{dS_{\mathrm{obs}}}{4\pi D^2} g_2^2 F_{\mathrm{d}}(e_{\mathrm{obs}}/g_2, t-\tau_{\mathrm{r}})\right]_j . \end{aligned} \tag{A.17}$$

A.2 Methods of numerical calculation

We numerically calculate trajectories of the rays emitted from the static source by solving the null geodesic equation; we apply the symplectic method (Moriyama & Mineshige 2015; Yoshida 1993), where the impact parameter of each ray is given by Karas et al. (1992). In this calculation, we obtain τ_{p}, N'_{p} and g_0, and then calculate F_{p} by using equation (A.4). Next, we calculate trajectories to reach the disc surface from the source, and obtain τ_{d}, N'_{d}, i, and g_1. Then we calculate $F_{\mathrm{K}\alpha}$ and F_{scat} by using equation (A.11).

We calculate ray trajectories which leave each area element of the observer's plane in the perpendicular direction to reach the disc by applying the symplectic method to obtain $\tau_{\mathrm{r}}(x_{\mathrm{obs}}, y_{\mathrm{obs}})$, and g_2. F_{tot} is calculated by substituting $F_{\mathrm{K}\alpha}, F_{\mathrm{scat}}$, $\tau_{\mathrm{r}}(x_{\mathrm{obs}}, y_{\mathrm{obs}})$, and g_2 in equation (A.17).

Appendix B

Disc-reflection scenario in the low inclination case

Resultant rms spectra and lag features of the relativistic disc reflection model for $i = 60$ deg are shown in §4. In this chapter, we explain those for the low inclination case, $i = 30$ deg.

Figure B.1 shows h dependence of the Fe-K line profiles and fluxes for different a. Doppler effect becomes weaker and thus a narrower Fe line is produced than the $i = 60$ deg cases; the blue cut-off energy and the red horn energy are ~ 6.8 keV and ~ 5.8 keV, respectively, whereas they are ~ 8 keV and ~ 5.2 keV for $i = 60$ deg. In particular, h dependence of the line flux is very different; the peak flux of the iron line varies by one order of magnitude between $h = 3$ and 8 for $i = 30$ deg, whereas it is only a factor of 2 for $i = 60$ deg. The large RDC variability makes the EW plots rather flat. The rms dip is not produced in this case; on the contrary, change of the line profile makes narrow *peaks* around 7 keV (figure B.2). Such peaks were predicted in model A of Niedźwiecki & Miyakawa (2010); they showed that increase of fractional variability in the Fe-K energy band is produced especially in the low-inclination cases ($i \leq 40$ deg). In this case, change of the Fe-K spectral shape depending on h is larger than the flux variability, and the variability amplitude rather increases. This rms peak brings us a strong statement that the relativistic light bending model has to be largely modified.

The 2D transfer functions, the lag-frequency plot, and the lag-energy spectrum have similar tendency to those for $i = 60$ deg, with small differences (figures B.3, B.4, B.5). The lag-frequency plots look very similar, and the Fe-K features in the lag-energy plots are sharper and less redshifted, which reflects the line profiles in the energy spectra.

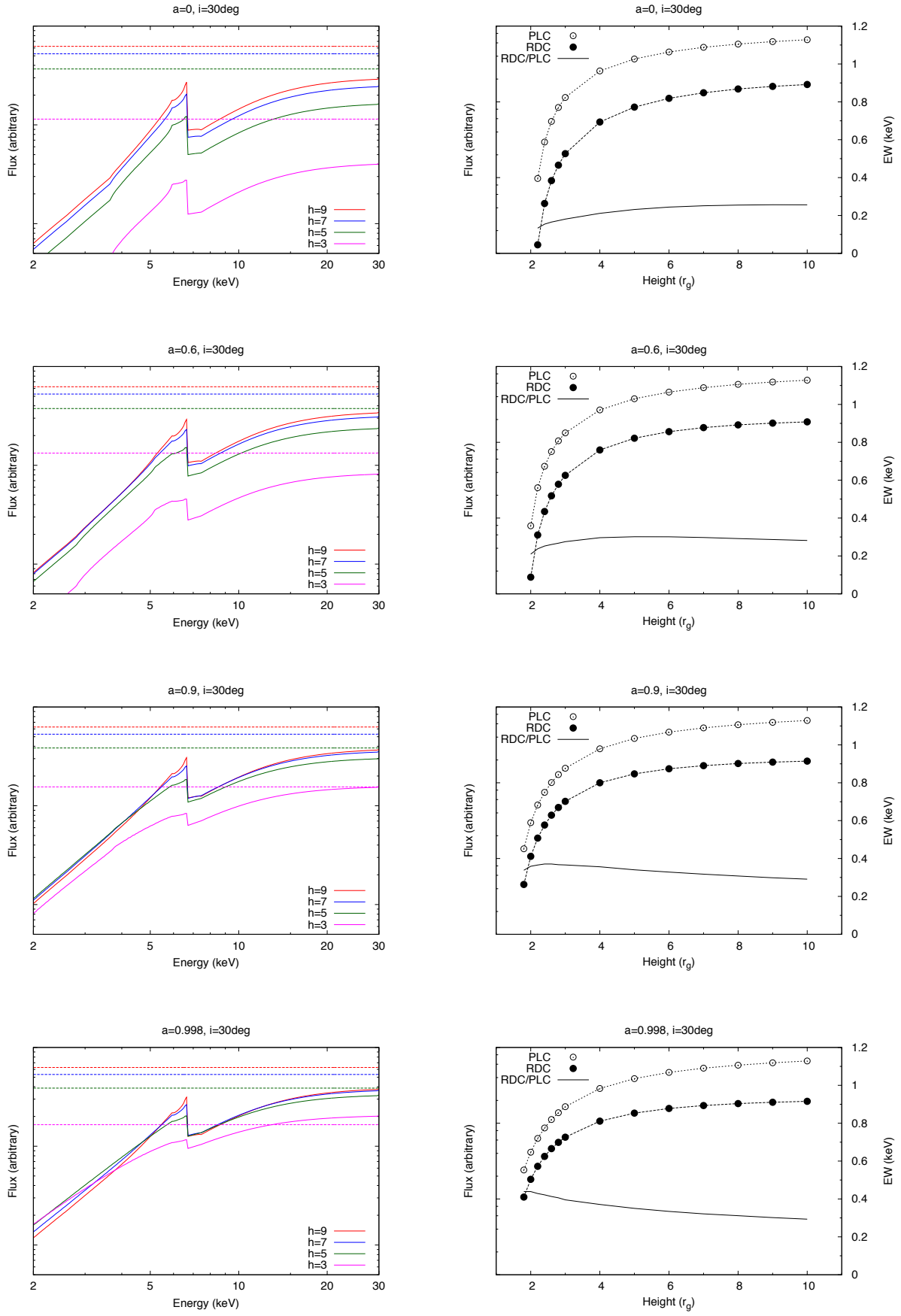

Figure B.1: Same as figure 4.2, but for $i = 30$ deg.

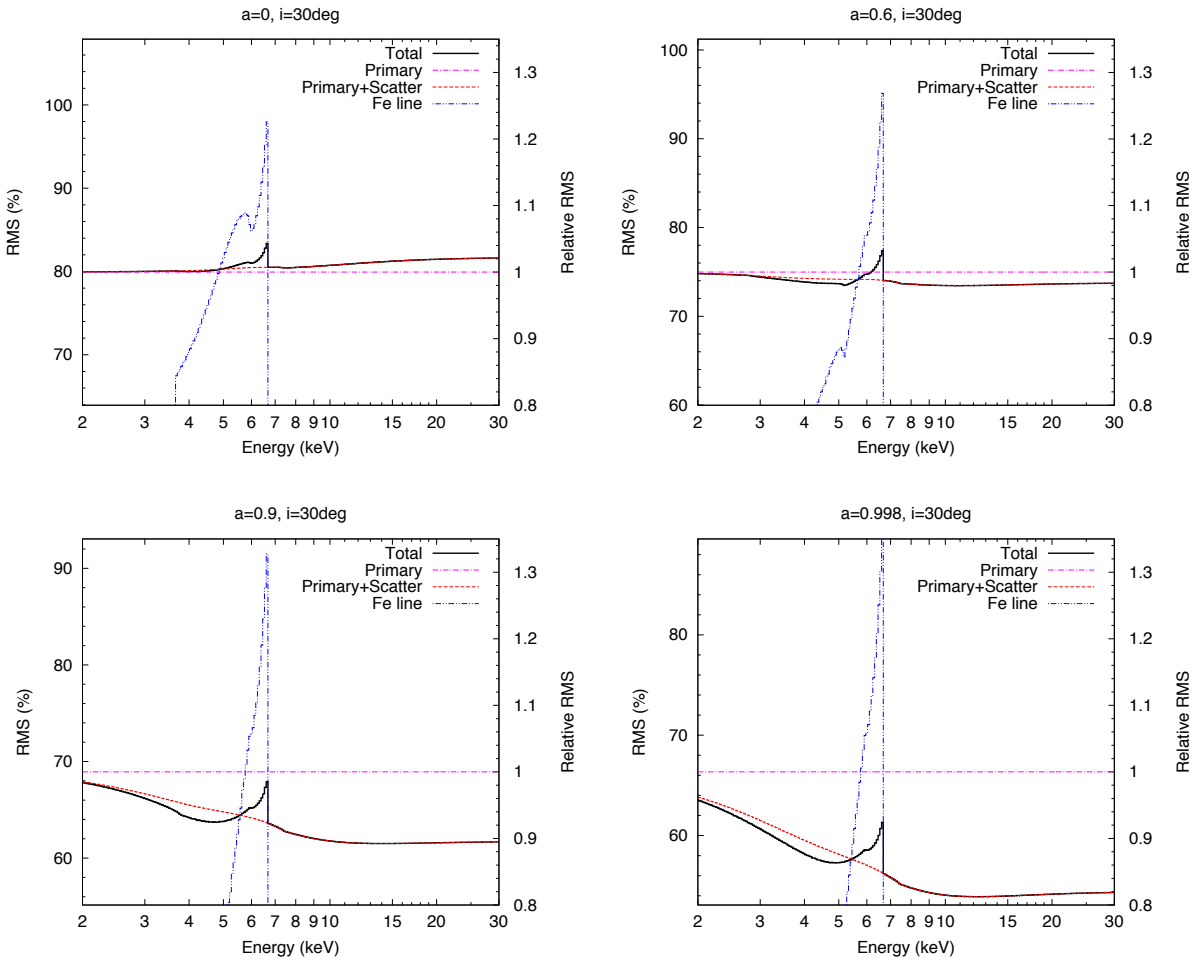

Figure B.2: Same as figure 4.3, but for $i = 30$ deg

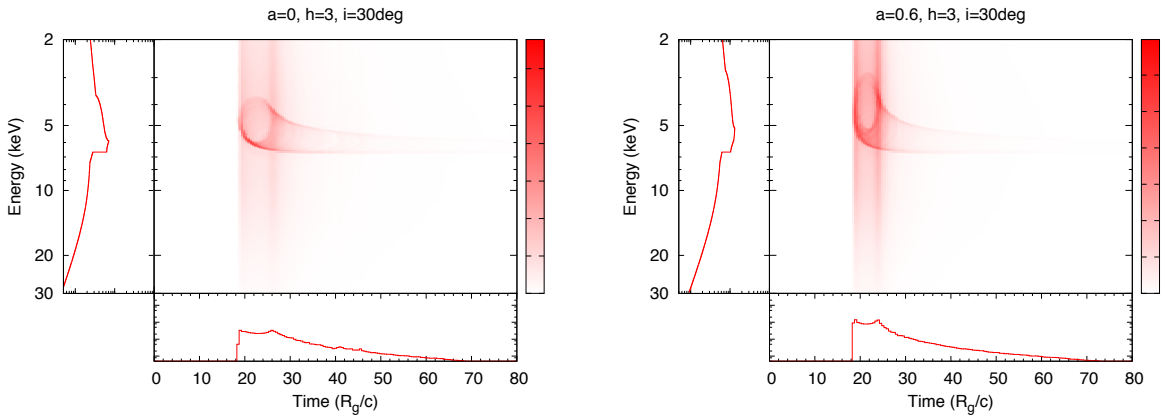

Figure B.3: Same as figure 4.4, but for $i = 30$ deg

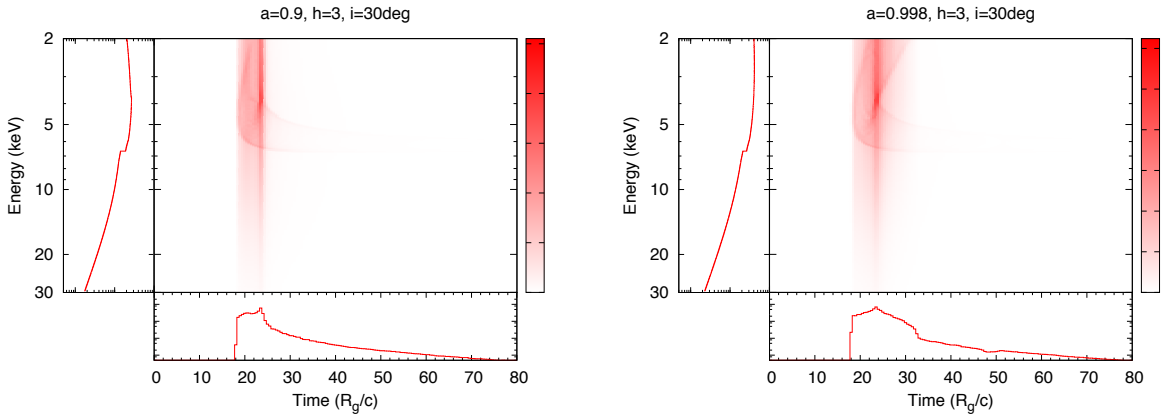

Figure B.3: *Continued.*

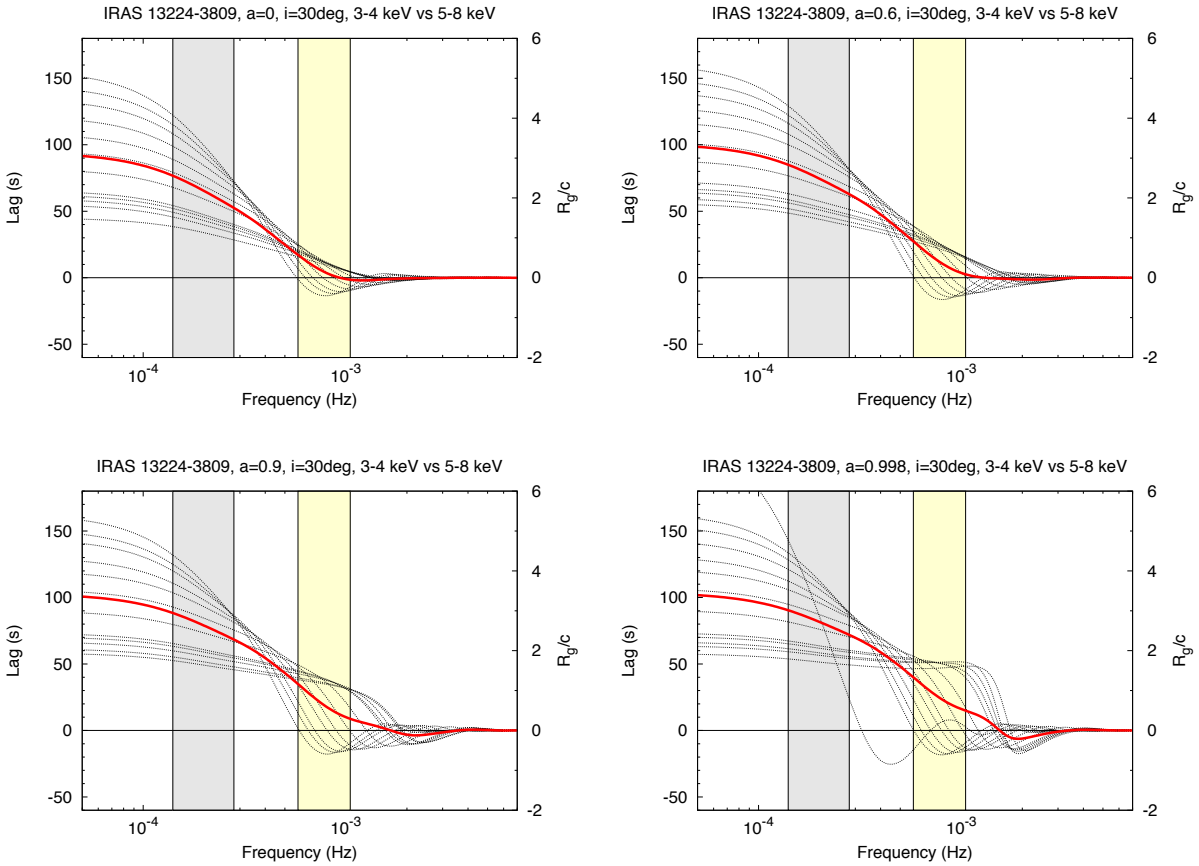

Figure B.4: Same as figure 4.5, but for $i = 30$ deg

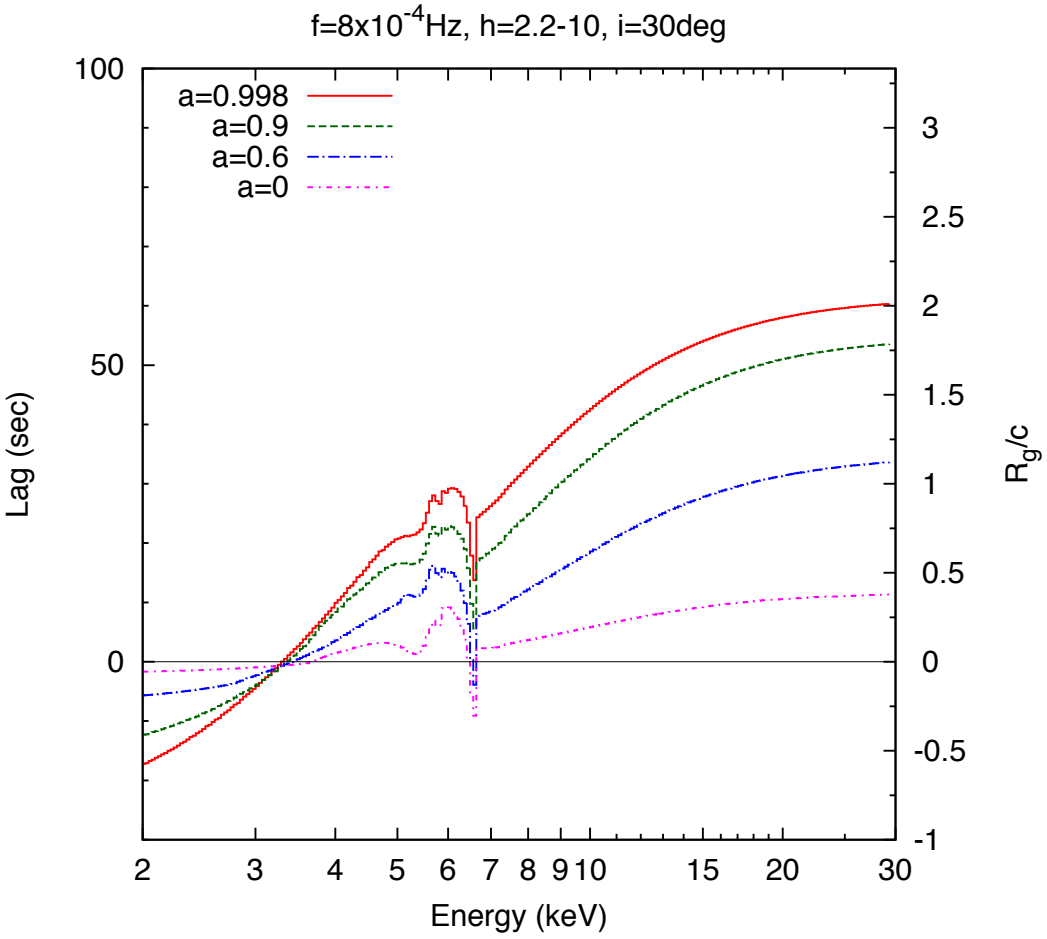

Figure B.5: Same as figure 4.6, but for $i = 30$ deg

Acknowledgments

This PhD thesis was completed by supports from many people. First of all, I am deeply grateful to Prof. Ken Ebisawa and Dr. Masahiro Tsujimoto, who have been guiding and encouraging me throughout the five years of my graduate course. Their deep insight, severe instructions, and passion to reveal mystery of the Universe invite me toward the academic curiosity. I could not complete this thesis without their kind help.

I have had a lot of advice, comments, help, and discussion from collaborators other than the above two persons. Section 4 is based on collaboration with Mr. Kotaro Moriyama, Prof. Shin Mineshige, and Dr. Norita Kawanaka. Especially this study could not be performed without the GR numerical code of Mr. Moriyama. Section 5 is based on collaboration with Prof. Chris Done, Dr. Kouichi Hagino, and Dr. Hirokazu Odaka. I also gratefully acknowledge Dr. Ken Ohsuga for his comments, and OB&OG members of Ebisawa laboratory; Q. Wada, H. Yamasaki, and E. Kusunoki. I would like to offer my special thanks to N. Uchiyama and M. Ichikawa.

Finally, I would like to express the deepest appreciation to my parents and twin brother for their support and understanding.